Pilot Studies for Quantitative 2D and 3D X-Ray Fluorescence Imaging

Dissertation
zur Erlangung des Doktorgrades
an der Fakultät für Mathematik, Informatik und Naturwissenschaften
Fachbereich Physik
der Universität Hamburg

vorgelegt von

Christian Gabriel Körnig

Hamburg
2022

Gutachter der Dissertation:	Prof. Dr. Florian Grüner Prof. Dr. Wolfgang J. Parak
Zusammensetzung der Prüfungskommission:	Prof. Dr. Günter H. W. Sigl Prof. Dr. Florian Grüner Prof. Dr. Wolfgang J. Parak Prof. Dr. Wolfgang Hillert Dr. Elisabetta Gargioni
Vorsitzender der Prüfungskommission:	Prof. Dr. Günter H. W. Sigl
Datum der Disputation:	21.11.2022
Vorsitzender Fach-Promotionsausschusses PHYSIK:	Prof. Dr. Wolfgang J. Parak
Leiter des Fachbereichs PHYSIK:	Prof. Dr. Günter H. W. Sigl
Dekan der Fakultät MIN:	Prof. Dr.-Ing. Norbert Ritter

Abstract

X-ray-fluorescence imaging (XFI) is an emerging functional imaging modality promising benefits for tumor detection, cell-tracking and pharmacokinetics. When matter is irradiated by an external x-ray beam, fluorescence photons in the x-ray regime characteristic for the elemental composition are emitted. By using non-endogenous high- or medium-Z elements as markers, this principle can be employed in a functional imaging modality. One challenge in this method is separating the fluorescence photons from background events, mostly created by Compton scattering. For achieving the highest sensitivities in XFI, a mono-energetic incident beam is thus needed, making synchrotrons the ideal x-ray source for XFI. However, the special characteristics of a synchrotron beamline have to be taken into account for the design of the experimental setup.

In the scope of this thesis, a series of pilot studies were performed to understand and optimize all aspects required to apply the principle of XFI to synchrotron-based in-vivo immune cell tracking at the P21.1 beamline at the Petra III synchrotron. Furthermore, a new reconstruction method is investigated which allows to reduce the radiation dose of three-dimensional spatial imaging of the fluorescence marker distribution. Combining the results, three-dimensional reconstruction of organ concentrations down to 650 ng/ml at in-vivo conform radiation levels are achievable, promising to allow tracking multiple types of cells simultaneously.

Zusammenfassung

Röntgenfluoreszenz-Bildgebung (RFB) ist eine vielversprechende Methode für funktionale Bildgebung mit potentiellen Anwendungen im Bereich Tumorerkennung, Zellverfolgung und Pharmakokintetik. Bei der Bestrahlung von Materie mit einem externen Röntgenstrahl werden Fluoreszenzphotonen im Röntgenbereich emittiert, die charakteristisch für die elementare Zusammensetzung sind. Dieser Mechanismus erlaubt funktionale Bildgebung, in dem nicht-endogene mittel- oder hoch-Z Elemente als Marker verwendet werden. Eine Herausforderung bei diesem Prinzip ist die Trennung zwischen Fluoreszenz- von Untergrundphotonen, die hauptsächlich durch Comptonstreuung entstehen. Um die höchste Sensitivität in RFB zu erreichen, ist daher ein mono-energetischer Röntgenstrahl nötig, weshalb ein Synchrotron die ideale Quelle ist. Allerdings müssen die speziellen Eigenschaften einer Synchrotronanlage bei der Planung des RFB-Experiments berücksichtigt werden.

In dieser Arbeit werden eine Reihe von Pilotstudien durchgeführt, mit dem Ziel alle benötigten Aspekte zu verstehen und optimieren, um durch RFB am P21.1 Messplatz des PETRA III Synchrotrons in-vivo Immunzellen zu verfolgen. Zusätzlich wird eine neue Methode zur dreidimensionalen Rekonstruktion der Fluoreszenzmarkerverteilung untersucht, durch die die Strahlendosis reduziert werden kann. Durch Kombination dieser Studien wird gezeigt, dass Organkonzentrationen bis 650 ng/ml mit einer in-vivo konformen Strahlendosis detektiert werden können, wordurch es ermöglicht wird, gleichzeitig mehrere Zellarten zu verfolgen.

Contents

1 Introduction **13**

2 Theory **21**

2.1 X-Ray Interactions 21

2.1.1 Compton Scattering 21

2.1.2 Photoabsorption 23

2.1.3 Fluorescence 24

2.1.4 Auger Cascades 27

2.1.5 Rayleigh Scattering 27

2.1.6 Lambert-Beer-Law 28

2.1.7 A Note on Conventions 29

2.1.8 Radiation Damage in Biological Tissue 29

2.2 X-Ray Sources 31

2.2.1 X-Ray Tube 31

2.2.2 Synchrotron Beamline 33

2.3 Absorption Imaging 34

2.3.1 Computed Tomography 34

2.3.2 Computed Tomosynthesis 38

2.4 Principles of Synchrotron-based XFI 39

2.5 X-Ray Detectors 43

2.5.1 Properties of CdTe Detectors 44

2.5.2 Properties of Silicon Detectors 46

2.5.3 Detector Selection for XFI 48

3 Methods **51**

3.1 Geant4 Simulations . . . 51

3.2 Experimental Setup . . . 54

3.2.1 Beamline Layout . . . 54

3.2.2 XFI Platform . . . 56

3.2.3 DAQ Software . . . 57

3.2.4 On-Axis Camera . . . 61

3.2.5 Standard Phantoms . . . 62

3.3 Quantitative X-Ray Fluorescence Imaging . . . 64

3.3.1 Fluorescence Marker Mass Determination . . . 64

3.3.2 Extraction of the Fluorescence Signal . . . 65

3.3.3 Signal Significance . . . 67

3.4 Effects of Attenuation on the Reconstructed Masses . . . 68

3.4.1 Attenuation Correction for a Single Detector . . . 68

3.4.2 Attenuation Correction for Multiple Detectors . . . 73

3.5 Beamline Incident Flux Measurement . . . 76

4 Quantitative Small Animal 2D XFI Measurements **83**

4.1 Thyroid Scans . . . 85

4.2 Biodistributions of Injected Iohexol and PdNPs . . . 90

4.3 In-situ Biodistributions of Labeled Macrophages . . . 93

4.4 In-vivo Biodistributions of Macrophages and Free Iohexol . . . 97

5 X-Ray Fluorescence Tomosynthesis **101**

5.0.1 XFTS Algorithm . . . 102

5.0.2 Quantitative XFTS Reconstruction . . . 105

5.0.3 XFTS Using Multiple Detectors . . . 106

5.1 XFTS Demonstration Experiment 107
5.1.1 Cylindrical Phantom Measurements 108
5.1.2 Mouse Phantom Measurements 119
5.1.3 Detection Limits and Comparison to Simulations 125

6 Conclusion and Outlook **129**

Bibliography **133**

Acknowledgement **153**

1 Introduction

Wilhelm C. Röntgen revolutionized medical diagnostics when he discovered x-rays [1] in 1895 and presented the first ever x-ray image showing his wife's hand. Röntgen found that a Crook's tube emitted radiation that could penetrate deep into tissue and would expose photographic plates. Already in 1900, x-rays were used in clinical applications, diagnosing fractured bones [2]. In the 20th century, the usage broadened and theoretical work on tomography - the 3D reconstruction of the structure from many individual images - dates back to as early as 1914 [3]. Limited by computing capacity, it took until 1973, before the first commercially viable computed tomography (CT) scan was performed by Godfrey Houndsfield [4]. Here, x-ray images are obtained from many projection angles. By back-projecting each image along its beam axis, it is possible to obtain the 3D distribution of attenuating material, allowing for better diagnosis than conventional x-ray images.

Nearly at the same time, in 1971, magnetic resonance imaging (MRI) was developed [5], providing an alternative to the imaging techniques based on ionizing radiation. Instead, MRI makes use of the quantum mechanical spin by using a combination of pulsed magnetic fields to measure relaxation times after exciting precession in the protons at their Larmor frequency [6, 7]. Additionally, MRI can not only be used as a structural imaging modality but also for functional imaging, often called fMRI. For such applications, magnetic markers are coupled to ligands and thus enhance the MRI response at positions where they accumulate [8].

Additionally, the development of positron emission tomography (PET) and single-photon emission computed tomography (SPECT) opened up new possibilities to monitor func-

tional properties within the body by using radioligands, i.e. radionuclides coupled to a ligand which defines the biological process to be monitored. In PET, positron emitters are used as radionuclides. As the positron will interact with the surrounding matter and be annihilated by an electron, two photons with 511 keV energy each are emitted in the nearly opposite direction (back-to-back). PET detectors are built as a segmented cylinder with many detector elements, often based on scintillators. Due to the back-to-back signature of the decay event, coincident events in opposing detector elements are generated, leading to a nearly background-free detection method [9]. For reconstruction, it is known that the photons have to be generated along the line between the two detector elements. This is a similar problem as for CT reconstruction, where the detected attenuation is the integral of the attenuation coefficient along the beam axis. Therefore, similar reconstruction methods can be applied. Alternatively, 3D reconstruction can be directly performed on an event basis, when measuring the time difference (time of flight, TOF) between the coincident events, which is called TOF-PET. This requires very fast detectors and has only become possible in recent years [9] but allows to directly determine the position along the line from which the photons were emitted. In contrast, SPECT is not based on positron emitters but directly uses gamma emitters, eliminating the need for a 360° detector. Detection is performed using pixelated flat-panel detectors and similar to CT, images from multiple projection angles have to be acquired. To obtain positional information, a grid collimator has to be used, such that only photons moving nearly perpendicular to the detector surface are detected. Reconstruction is similar to CT, but SPECT images typically have higher noise levels and worse spatial resolution [10]. An important clinical use case for PET and SPECT is oncology, where glucose analog radioligands are used to find metastatic tumors [10].

Furthermore, optical imaging methods such as fluorescence imaging and bioluminescence imaging (BLI) exist. In fluorescence imaging, markers emit light of a specific wavelength when they are excited by an external light source. In bioluminescence imaging, the

markers are instead based on enzymes that catalyze chemical processes which emit light of a specific wavelength removing the need for an external light source [11]. Fluorescence and bioluminescence can then be detected by regular CCD cameras.

Other than their valuable contribution to medicine, these imaging methods also had a big influence on medical research, offering new perspectives to understand biological processes and aiding drug development. They can be used to bridge the gap between in-vitro experiments on the cellular level and human trials in preclinical research by studying the processes in-vivo in animal models [12]. The most important animal model is the mouse, which offers high genetic homology with humans [11, 13] and methods for genetic variation are well understood. This allows researchers to block or promote specific parts of the organism allowing systematic studies of diseases [11, 14, 15]. In contrast to in-situ experiments, where the animal has to be sacrificed for analysis, in-vivo imaging in such applications provides the possibility to study processes evolving over time in one individual organism, improving the experimental accuracy and strongly reducing the number of animals required for such experiments [13]. Thus, a branch of medical research has evolved to improve the ability to target specific processes with markers for one of the aforementioned imaging modalities. Most prominently, nanoparticles (NPs) have demonstrated very useful and tunable characteristics, making them an ideal candidate for versatile markers. Depending on the size, shape, and coating, injected nanoparticles will accumulate in different organs or tumors, but the effects of each individual NP property, as well as the interplay between them, are not yet well understood [16]. Targeting specificity can be further increased by coating the NPs with polymers or different kinds of ligands [17–20].

Immunotherapies, such as cell therapy pare promising treatments for diseases like cancer and autoimmune disorders, but only a few such therapies are in clinical use today [21, 22]. In immunotherapies, not the disease itself is treated, but instead the immune system

response of the patient is stimulated or modified to aid in fighting the disease. An important tool for improving these treatments is to monitor the biodistribution of immune cells in-vivo. To do so, the labeling with markers of a suitable imaging modality has to be performed on the cellular level to directly observe the behavior of these cells, providing deep insight into specific immune responses. Today, such labeling is mostly performed with radiotracers for PET imaging [22–24] but in many cases no non-invasive imaging method is suitable and an alternative evaluation of efficacy such as lethality comparisons or histology has to be performed, resulting in the use of many animals and reducing the insight into biological mechanisms [13].

Depending on the goal of a study, the most suited imaging modality might vary. Fluorescence and BLI provide high sensitivity and the ability for multiplexed imaging, allowing to distinguishably label different targets at the same time [25–27]. But penetration depth of the optical or near-infrared light through tissue is limited, offering only a few millimeters of observable depth with quickly deteriorating spatial resolution, thus being mostly used for in-vitro measurements or imaging of subcutaneous features [27, 28].

PET provides high sensitivity as the coincident detection of back-to-back photons is nearly background-free. However, due to the positron range before anihilation, the spatial resolution of PET imaging is limited to a few millimeters, depending on the energy of the emitted positron [29]. Local radiation doses in PET are relatively high and can reach the order of several Grays in the targeted organs [11]. Additionally, radiation damage can lead to death of the labeled cells [8, 30], thus affecting the dynamics of the process to be imaged. Furthermore, only relatively short longitudinal studies are possible, as the injected marker decays over time. Nowadays, PET is combined with either a CT or MRI scan, to obtain anatomical information. Without such an additional modality, interpretation of the PET results is often difficult. However, this increases the complexity and cost of the scanner and in case of CT further increases the already relatively high

radiation dose. Multiplexed imaging in PET is not possible, as the two-photon signature of the beta decay is indistinguishable for different elements [11].

SPECT has mostly similar properties as PET, with some key differences: Sensitivity of SPECT is typically lower than in PET, as single photon events are recorded and the detector has to be highly collimated to only allow nearly-perpendicular photons to be detected to obtain positional information. Alternatively, SPECT can be performed using a pinhole collimator. In this geometry spatial resolution is better and can be superior to PET, since gamma-emitters are used and therefore the signal is directly emitted from the marker location. However, this detection method strongly reduces the effective detector size and thus results in much larger radiation doses. In principle, multiplexed imaging is possible by using different radiotracers with distinct decay energies, but differentiation of these energies is challenging with typically used detectors [31].

While MRI does not rely on radioactive tracers and can thus be used for long-term monitoring and also offers high spatial resolution and no radiation damage, its sensitivity in functional imaging is relatively low compared to methods like PET and BLI [8, 32, 33] and cell labeling via reporter genes have shown limited efficacy [8, 34]. Furthermore, quantitative analysis remains challanging [33]. Recently, methods have been developed to enable multi-color imaging, by using the direct detection of ^{19}F, instead of indirect markers based on iron or gadolinium [35]. By variation of the chemical properties of ^{19}F molecules, the resonance frequency can be shifted to allow for multiplexed imaging [36]. However, to detect these changes, specialized MRI machines are needed.

X-ray fluorescence imaging (XFI) is an emerging alternative imaging modality [37–41], which promises to fill the existing gap between the aforementioned modalities. Its working principle is similar to optical fluorescence, i.e. a marker is emitting photons with a characteristic wavelength when exited by an external source, however, both the external source and the emitted fluorescence are in the x-ray regime. By using x-rays instead

of optical photons, penetration depth in tissue is much longer, such that any location inside a mouse can be probed while spatial resolution remains high. Furthermore, x-ray fluorescence is an inherent property of any element, each having a unique fluorescence spectrum, meaning that a wide variety of elements can be used as fluorescence markers. This allows to find the best suitable marker for a target to label without many constraints and can be used for highly multiplexed imaging. Additionally, as these markers do not have to be radioactive, XFI can be used for longitudinal studies over several weeks [42]. In XFI, spectral background is present due to scattering processes in the tissue. However, by carefully designing the experimental setup, the spectrum of the background contributions can be shaped such that the fluorescence energy region is virtually background-free, although this requires performing XFI at synchrotron facilities. On the other hand, XFI is a scanning method, resulting in comparatively long imaging durations. Radiation dose can be adjusted depending on the required sensitivity but is typically similar to micro-CT scans or PET/SPECT imaging [11, 43, 44]. Additionally, x-ray fluorescence can be used as a detection method ranging from in-vitro single-cell and micro-sample analysis [45, 46] up to small animal [38–40] and even human imaging [37, 47], potentially allowing to use the same marker and labeling technique across the full research cycle. Thus, XFI promises to be a valuable tool for drug and cell tracking studies, which are today mostly performed - if possible - using PET and SPECT imaging.

While x-ray fluorescence analysis (XRF) of small samples in the order of µm thickness is a standard procedure at many synchrotron beamlines [48–50], translating this principle to a medical imaging modality is a non-trivial task and is not in the repertoire of such facilities. This thesis discusses, how XFI can be implemented and advanced towards in-vivo measurements at synchrotrons with a focus on cell- or drug tracking applications and thus maximum sensitivity. After introducing the involved physical processes in chapter 2.1 and an in-depth comparison of different approaches for XFI experiments in chapter 2.4, chapter 3 covers the methods used in the synchrotron experiments and analysis.

Chapter 4 presents a series of pilot studies to evolve synchrotron-based 2D XFI to in-vivo detection of labeled cells and in chapter 5 a novel approach to obtain 3D image reconstruction without an extensive increase in radiation dose is presented.

2 Theory

2.1 X-Ray Interactions

The concept of XFI is based on the idea to use an incident x-ray beam to probe the sample. It is thus important, to understand the different interactions that can happen between photons and matter, which define the characteristics of the signal and background contributions in XFI measurements.

2.1.1 Compton Scattering

Compton scattering refers to the elastic scattering of a photon at an electron of an atomic shell [51]. In its most simplistic form, the electron is assumed to be free at rest, making the scattering a two-particle process. Using energy and momentum conservation, a fixed relation between the scattering angle (i.e. the angle between the photon's velocity before and after the interaction) and the energy transfer can be obtained, given as

$$\frac{E'}{E} = \frac{1}{1 + \frac{E}{m_e c^2}\left(1 - \cos\theta\right)}\,, \tag{2.1}$$

where E is the initial energy and E' the final energy of the photon, m_e the electron rest mass, c the speed of light, and θ the Compton scattering angle.

In this case, the cross section is given by the Klein-Nishina formula [52]

$$\frac{d\sigma}{d\Omega}_{KN}(E, \theta, \phi) = \frac{1}{2}\left(r_e \frac{E'}{E}\right)^2 \left(\frac{E'}{E} + \frac{E}{E'} - 2\sin^2(\theta)\cos^2(\phi)\right) \tag{2.2}$$

with ϕ the polar angle relative to the polarization plane of the incident photon and

$$r_e = \frac{1}{4\pi\epsilon_0}\frac{e}{m_e c^2} \tag{2.3}$$

being the Bohr radius.

While synchrotron beamlines typically offer highly polarized beams, the emitted photons of most other x-ray sources such as x-ray tubes or radioactive samples are unpolarized. In this case, eq. 2.2 has to be averaged over all polar angles, resulting in a simplified cross section

$$\frac{d\sigma}{d\Omega}^{UP}_{KN}(E,\theta) = \frac{1}{2}\left(r_e\frac{E'}{E}\right)^2\left(\frac{E'}{E}+\frac{E}{E'}-\sin^2(\theta)\right). \tag{2.4}$$

The Klein-Nishina cross section is shown in figure 2.1. Note, that 90° scattering is strongly suppressed in the polarization plane.

For Compton scattering in matter, the electrons are not free but bound in an atomic shell and thus the dynamics of the electrons have to be taken into account. Therefore, the fixed relationship between energy transfer and scattering angle as well as the Klein-Nishina cross section are no longer valid, but corrections are required [53].

Typically, these corrections are combined in a scattering function $SF(E,Z,\theta)$ such that the Compton scattering cross section for an element Z is given as

$$\frac{d\sigma}{d\Omega}_{Compt}(E,Z,\theta,\phi) = \frac{d\sigma}{d\Omega}_{KN}(E,\theta,\phi)\cdot SF(E,Z,\theta). \tag{2.5}$$

These scattering functions can either be obtained via experiments or calculated ab-initio, e.g. by using the scattering matrix elements [53]. In first approximation, $SF(E,Z,\theta)$ scales linearly with the total number of electrons - which is equal to Z - as each individual electron of an atom can interact with the photon. Figure 2.2 shows the scattering function normalized to Z for three elements and various incident energies. Small angle scattering is strongly suppressed compared to the Klein-Nishina equation, as the bound electrons carry momentum perpendicular to the incident photon. For larger scattering angles, the

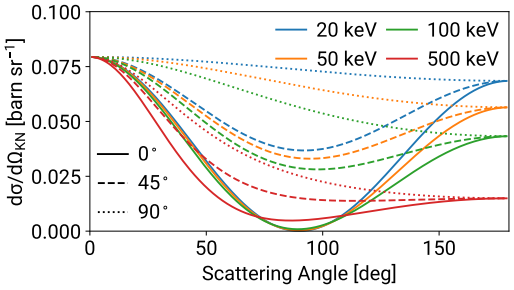

Figure 2.1 – Polarized Klein-Nishina cross section for different energies and polarization angles. The unpolarized cross section is identical to the case of $\phi = 45°$. Data taken from [54].

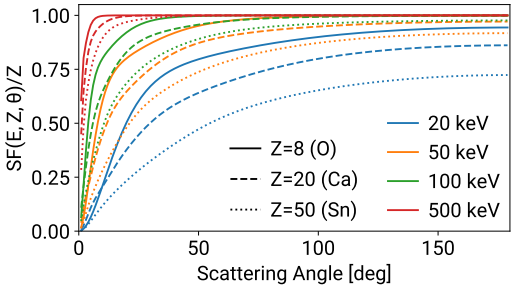

Figure 2.2 – Scattering functions normalized to Z for different energies and elements. Data taken from [54].

normalized scattering function approaches one, i.e. electron shell dynamics become less dominant. Photons with higher incident energy are less affected by these corrections as the binding energy becomes negligible compared to the photon's energy and the electron can be seen as quasi-free. However, in the energy range of interest for XFI between 20 and 100 keV, these corrections are still important.

2.1.2 Photoabsorption

Photoabsorption describes the process, in which the incident photon is absorbed by an electron and the photon's energy is transferred to the electron. Due to conservation of momentum, this process can only happen at bound electrons. Furthermore, the photon's energy must be larger than the binding energy of the electron, meaning that the photoabsorption ionizes the atom. Currently, no complete theoretical formulation for the photoabsorption cross section exists, but a general scaling law

$$\sigma_{phot} \sim Z^5 E^{-3.5} \tag{2.6}$$

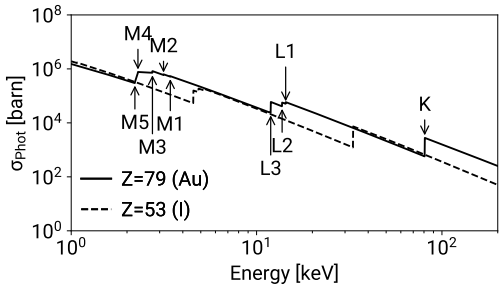

Figure 2.3 – Photo cross section for gold and iodine. Shell edges are labeled for gold. Data taken from [54].

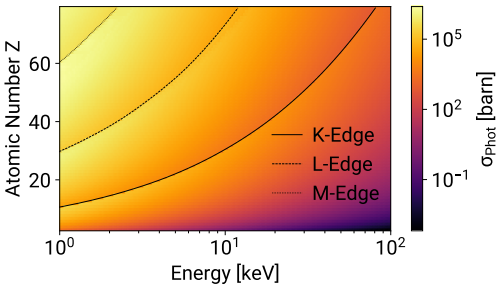

Figure 2.4 – Photo cross section dependency on the atomic number and incident energy. Data taken from [54].

has been observed [55]. Furthermore, steep edges in the cross section are present, whenever the photon's energy becomes larger than the binding energy of a (sub-)shell, as more electrons can interact in the process, as visible in figures 2.3 and 2.4.

2.1.3 Fluorescence

After a photoabsorption event in an atom, the vacant electron state can be filled by an electron of a higher shell, in its process releasing a fluorescence photon which carries the energy difference between the two binding states away, as shown in figure 2.5. The exact fluorescence energy is unique for each atom and shell combination as it depends on the binding energies of the involved electron's (sub-)shells. Therefore, the element from which the fluorescence is emitted can be deduced by measuring the energy of the fluorescence photon. Allowed transitions are defined by the quantum mechanical selection rules, requiring $\Delta n = \pm 1$, $\Delta l = \pm 1$, $\Delta j = 0, \pm 1$ where n is the principal quantum number corresponding to the shell, l the angular momentum quantum number and j the total angular momentum number including spin [56]. Figure 2.6 shows possible transitions involving the K,L and M shell. For describing the set of lines from one shell to another,

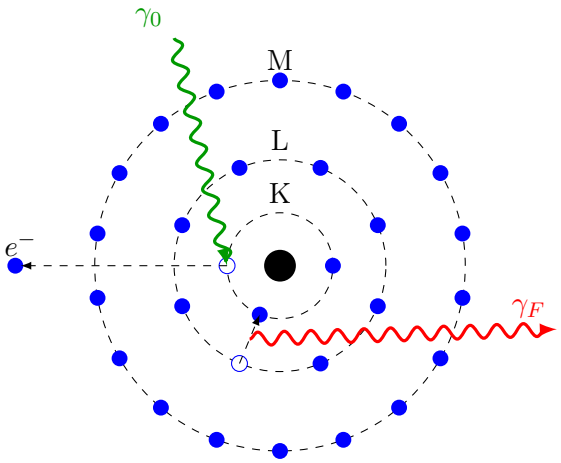

Figure 2.5 – Schematic view of a fluorescence event. The incident photon γ_0 (green) gets absorbed by a K-shell electron which thus leaves its shell. The vacant state is populated by an electron from a higher-energetic shell. This transition results in the radiation of a fluorescence photon γ_F (red). Image adapted from [59].

the Siegbahn notation [57] is used, which uses the letter of the vacant shell and a subscript Greek letter denominating the number of shells in between the transition. As an example, K_β describes the transition of an electron from the M to the K shell. However, when describing a specific line, the IUPAC convention is used in this thesis, where target and origin subshell are both named, e.g. the K-L_2-line or L_3-M_5-line [58]. Figure 2.6 shows possible K and L_α transitions between the subshells. Due to the selection rules, only a few lines define the K-shell fluorescence spectrum, while for L-shell fluorescence many transitions have to be taken into account[†].

As fluorescence is a secondary process following photoabsorption, its cross section scales similarly. Figures 2.7 and 2.8 shows the K- and L-fluorescence cross section for different incident energies. Comparing it to the absorption cross section in figure 2.3 highlights

[†]While figure 2.6 only depicts L_α lines, L_β and L_γ can also contribute significantly to the overall L-shell fluorescence spectrum

the same properties. The fluorescence cross section has its maximum when the incident photon's energy is right above the edge energy of the corresponding shell and quickly falls off for higher energies.

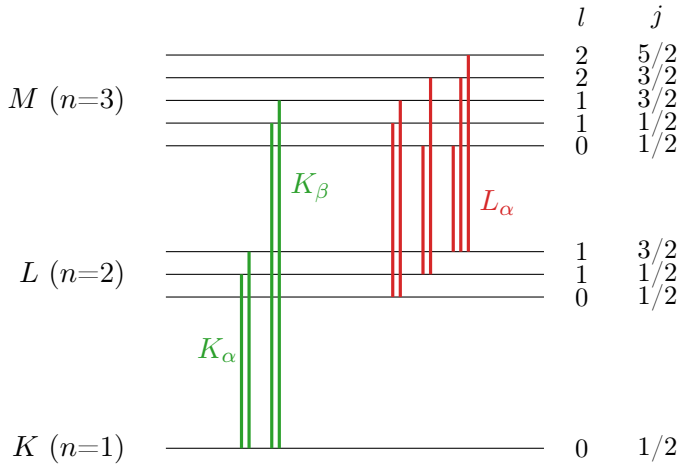

Figure 2.6 – Illustration of possible electron transitions and fluorescence lines.

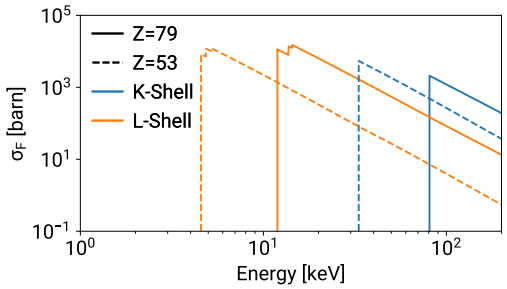

Figure 2.7 – K- and L-shell fluorescence cross section for gold (Z=79) and iodine (Z=53). Data taken from [54].

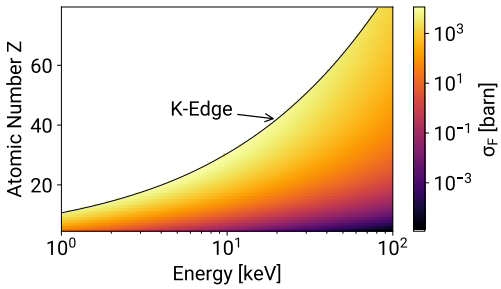

Figure 2.8 – K-shell fluorescence cross section dependency on the atomic number and incident energy. Data taken from [54].

2.1.4 Auger Cascades

Alternatively to the radiative transition as fluorescence, the excess energy after a transition of an electron to a lower shell can also be transferred to another electron of the shell. This so-called Auger effect results in the emission of an electron instead of a photon, thus often called non-radiative. For each subshell of an element, the fluorescence yield can be defined, describing which fraction of transitions from this shell will result in fluorescence and which in Auger events [56]. Fluorescence yields become small for higher shells, meaning that a K or L shell fluorescence event will be followed by a cascade of Auger electrons. As electrons at these energies have only a travel length of a few micrometers [60], they will be absorbed nearly immediately and will not be measured. However, they contribute to the total radiation dose in the object [61].

2.1.5 Rayleigh Scattering

Rayleigh scattering describes the process of elastic scattering of a photon with a bound electron. In this process, no energy is transferred but only a change of momentum occurs. Rayleigh scattering is mostly prominent at small angles and increasing for higher-Z elements [55] as shown in figure 2.9. Due to its elastic nature, Rayleigh scattering can easily be separated in spectral measurements and does not contribute to the background of the fluorescence signal.

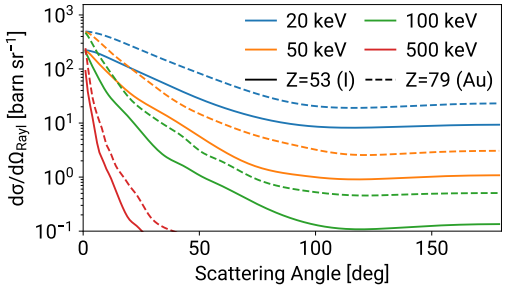

Figure 2.9 – Differential Rayleigh scattering cross section for different incident energies and elements. Data taken from [54].

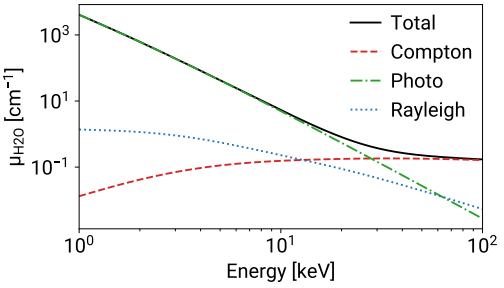

Figure 2.10 – Contributions to the attenuation coefficient of water across different energies. Data taken from [54].

2.1.6 Lambert-Beer-Law

An important quantity of interest is the total transmission of an x-ray beam through a block of matter. It can be obtained using the Lambert-Beer-Law

$$I(x) = I_0 \cdot \exp\left(-\left(\frac{\mu}{\rho}\right)_{tot} \cdot \rho \cdot x\right) \tag{2.7}$$

with x the depth inside the material, ρ its density and $\left(\frac{\mu}{\rho}\right)_{tot}$ the attenuation coefficient. The attenuation coefficient is strongly connected to the cross section via

$$\left(\frac{\mu}{\rho}\right)_{tot} = \left(\frac{\mu}{\rho}\right)_{phot} + \left(\frac{\mu}{\rho}\right)_{CS} + \left(\frac{\mu}{\rho}\right)_{Rayl} = \left(\sigma_{phot} + \sigma_{CS} + \sigma_{Rayl}\right) \frac{N_A}{M} \tag{2.8}$$

with N_A the Avogadro constant and M the molar mass. This law describes the probability, of not interacting via one of the processes during a given length, which is typically called transmission. However, especially in the case of Rayleigh scattering, one has to be careful if and to which extent its cross section shall be included in the attenuation coefficient, as due to its properties (small scattering angles and no energy loss) the scattered photon might be indistinguishable from a transmitted photon.

Figure 2.10 illustrates the scaling of the contributions of the different processes across

different x-ray energies. For $E \leq 30\,\mathrm{keV}$, photoabsorption dominates the attenuation, for higher energies Compton scattering becomes dominant.

2.1.7 A Note on Conventions

Due to the relation given in eq. 2.8, it is common in the field of photon science to use the term cross section for what is in fact the attenuation coefficient and define the cross section in units of cm^2/g. This simplifies many equations when describing particle-matter interactions instead of particle-particle interactions. In this thesis, this convention is only applied to fluorescence cross sections, where the term attenuation coefficient might be misleading since the attenuation arises from the photoabsorption and fluorescence is only a secondary event. Using this convention, the number of created fluorescence photons is then simply given as

$$N_F = N_0 \sigma_F \rho_F l \tag{2.9}$$

with N_0 the number of incident photons, σ_F the fluorescence cross section (in cm^2/g), ρ_F the density of the fluorescence marker and l the length inside the fluorescence material.

2.1.8 Radiation Damage in Biological Tissue

Due to the interactions of the incident photons as listed above, atoms and molecules of biological tissue will become ionized, and a single incident interaction can result in many ionized molecules which then break up into radicals. This is especially likely for water, making organisms with high water-content radiation-sensitive. The H and OH radicals can react with other molecules of the cell or DNA, leading to cell death or transformation. When too many cells are damaged, the radiation exposure can become fatal for the organism. Additionally, cell transformation can lead to long-term stochastic effects, most prominently cancer induction [62].

As a quantity for the radiation exposure, the absorbed dose, i.e. the total amount of energy deposited per mass of tissue is often used, measured in Gray ($1\,\mathrm{Gy} = 1\,\mathrm{J/kg}$).

For calculating the deposited energy, not the attenuation coefficient, but the so-called mass-energy absorption coefficient $\left(\frac{\mu}{\rho}\right)_{en}$ is used [63]. This quantity takes into account that not all energy of an interaction might be deposited in the matter. The difference between the attenuation coefficient and the mass-energy absorption coefficient is shown in figure 2.11. For low energies, both values are nearly identical, as photoabsorption is the dominant effect and the range of any secondary particle is small, meaning that with high likelihood the complete energy of a photon is transferred to the absorber during an interaction. For higher energies, where Compton scattering is more likely to occur, much less than the total energy is absorbed and the mass-energy absorption coefficient becomes smaller than the attenuation coefficient.

Using this quantity, the deposited dose in the material can be calculated via

$$D = \left(\frac{\mu}{\rho}\right)_{en} \cdot E_0 \cdot \Phi \tag{2.10}$$

with E_0 the incident photon's energy and Φ the number of photons per radiated area.

Figure 2.12 shows simulated absorbed dose values per 10^{10} photons/mm^2 at the isocenter of a cylindrical water phantom with different radii. For lower energies, where the beam has only a short range in the phantom, dose is much higher for small phantoms. At higher energies, beam attenuation becomes smaller and the deposited dose is only minimally dependent on the phantom diameter.

Fatal radiation doses are typically expressed as $LD_{50/30}$, which is the dose for which the exposure is lethal within 30 days in 50% of all cases. For humans, this limit is about 4 Gy, while the $LD_{50/30}$ for mice is around 6.2 Gy [62].

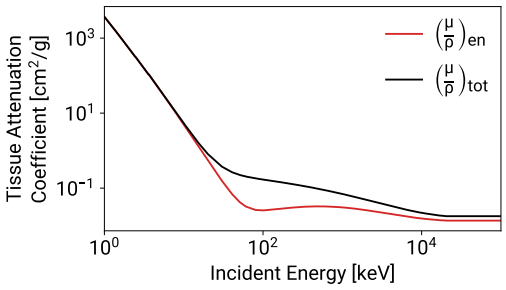

Figure 2.11 – Comparison between $\left(\frac{\mu}{\rho}\right)_{en}$ and $\left(\frac{\mu}{\rho}\right)_{en}$ for soft tissue. Data obtained from [63] and interpolated in the log-log domain.

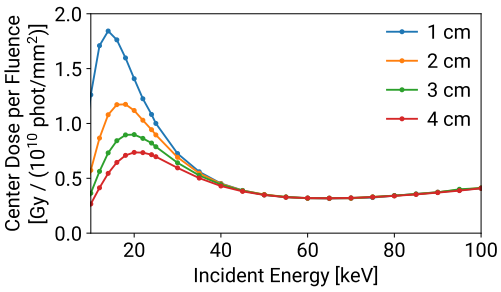

Figure 2.12 – Radiation dose per incident fluence at the isocenter of a simulated water phantom with different radii for mono-energetic incident radiation. Tabulated data taken from [43].

However, in the context of x-ray fluorescence imaging in preclinical applications, not the fatal dose is of interest. With the goal of using XFI for long-term in-vivo cell- or drug-tracking, these dynamics must not be severely influenced by the radiation exposure. It has been shown that rodents are capable of recovering from doses up to 300 mGy within a few hours [64]. Therefore, this limit - which is much lower than the $LD_{50/30}$ - is used for all pilot studies in this thesis. It can be seen in figure 2.12 that the deposited dose per fluence is minimal in the range between 50 and 70 keV, making this a well-suited energy region for imaging modalities.

2.2 X-Ray Sources

2.2.1 X-Ray Tube

Wilhelm Röntgen famously discovered x-rays in 1895 during experiments with a Crookes tube [1] for which he was awarded the first Nobel Prize in 1901. The basic design concept of an x-ray tube is today still the same as it was invented by Coolidge in 1913 [65],

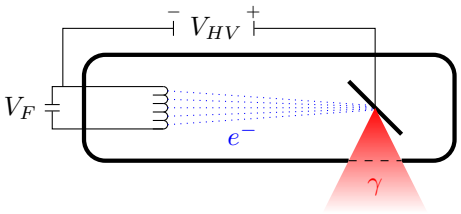

Figure 2.13 – Basic principle of a Coolidge x-ray tube.

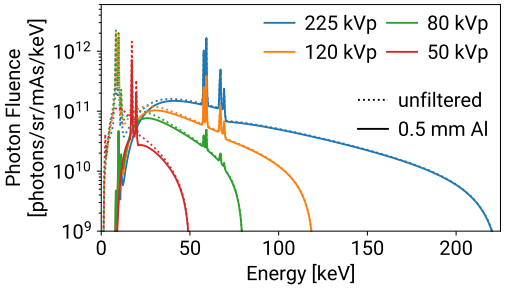

Figure 2.14 – Simulated x-ray tube spectra using SpekPy [67, 68] for different voltages. For 50 kVp, a molybdenum anode is used and tungsten anodes are used for higher energies.

depicted in figure 2.13. Electrons are emitted from a heated filament cathode. By applying a high voltage between the filament and the target anode, electrons are accelerated. When hitting the target, x-rays are generated via bremsstrahlung. Additionally, characteristic x-rays - which are fluorescence photons - are emitted depending on the target material. Typically, about 99% of the electrons' energy is transferred into heat and only 1% into x-ray photons, meaning the anode has to withstand high temperatures. Therefore, typical anode materials are molybdenum for acceleration voltages below 50 kV or tungsten for higher voltages. As bremsstrahlung is a continuous process, a cone-shaped broad spectrum is emitted. The photon flux of an x-ray tube is proportional to the electron current and the square of the acceleration voltage [66].

An important figure of merit for x-ray tubes is the focal spot size, i.e. the spread of the electrons when interacting with the anode. This spot size limits the resolution that can be obtained in absorption imaging. Modern clinical x-ray tubes achieve spot sizes of a few hundred micrometers [69] and preclinical micro-focus tubes around 5 µm [70]. However, with reduced spot size, the heat load onto the target becomes higher, imposing limits on the flux. To mitigate this issue, concepts like rotating anodes or liquid metal

jet anodes have been developed and clinical tubes are typically operated in pulsed mode to prevent damage to the anode [66].

2.2.2 Synchrotron Beamline

At synchrotron light sources, x-rays are generated by deflecting high-energetic electrons in a magnetic field. Originally, synchrotron beamlines were placed at the bending magnet sections of storage rings of particle physics experiments [71]. Today, dedicated synchrotrons are typically used and the x-ray photons are not generated in the bending magnet section, but in specialized insertion devices (ID). These IDs consist of periodically arranged alternating magnets, deflecting the electron beam back and forth, resulting in the emission of x-ray photons. Depending on the strength of the deflection, wigglers and undulators are distinguished. In a wiggler, the deflection angle is relatively large, resulting in a wide opening angle of the x-ray beam. In this case, photons generated in the different periods do not interfere with each other, creating a broad energy spectrum. Wigglers are typically used if a large beam size is needed. In contrast, the deflection in undulators is smaller and the generated photons of each period interfere with each other. This results in an emitted spectrum consisting of sharp peaks at the fundamental interference wavelength as well as at higher harmonics instead of a broad white beam [72, 73].

After the insertion device, the generated x-ray beam is conditioned using different x-ray optics. Most prominently, a specific harmonic is filtered using Bragg diffraction in a crystal, resulting in a monochromatic x-ray beam. Typically, energy resolutions of $\Delta E/E \approx 10^{-4}$ can be achieved [74]. Based on the application, other components such as focussing crystals or compound refractive lenses can be used to generate parallel or focussed beams. As both, wiggler and undulator are based on synchrotron radiation which generates polarized photons, the x-ray beam of IDs is polarized as well [72].

Experiments discussed in this thesis have been performed at the P21.1 beamline of the PETRA III synchrotron (DESY, Hamburg, Germany). The characteristics of the available beam are

- 53 or 101 keV beam energy
- parallel $1 \times 1\,\mathrm{mm}^2$ beam size
- horizontally polarized
- $\approx 10^{11}$ photons/s incident flux

More details about the beamline are given in chapter 3.2.1.

2.3 Absorption Imaging

Initially, x-ray absorption imaging was limited to planar 2D imaging, where only the integrated attenuation along the projection plane can be detected. While this already provided very useful information and is still often employed today, in many cases a three-dimensional imaging method is needed.

2.3.1 Computed Tomography

In 1973, Houndsfield demonstrated the principle of computed tomography (CT) [4]. During a CT scan, many (today typically $\approx$ 1000 [75]) projection absorption images are recorded at different rotation angles around the object of interest and reconstruction algorithms are used to calculate the distribution of attenuating material.

Reconstruction of CT data is performed on each slice, representing the plane of the rotation at a specific height. A common way of representing the obtained CT data of a slice is the so-called sinogram, a 2D image, where each column represents the absorption profile

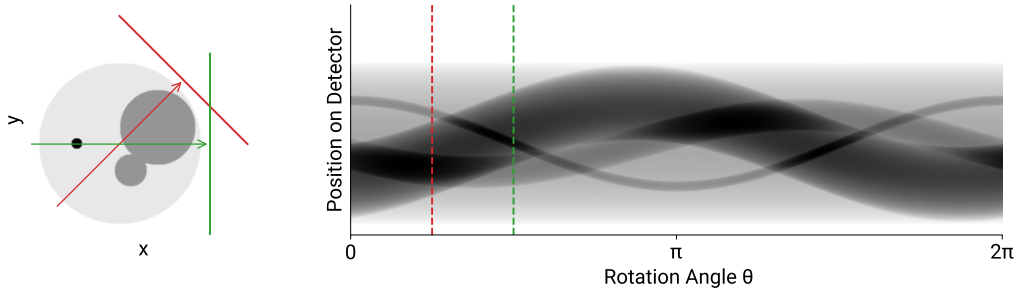

Figure 2.15 – Definition of the sinogram. The density distribution of the slice in the physical space (left), is mapped to the sinogram (right) in the rotated space defined by the rotation angle θ and the rotated detector plane. A full 360° rotation is shown, however, often data is only acquired over 180° as the attenuation along a line is equal independent of the direction, and thus 180° are sufficient to obtain a complete dataset. Red and green markers indicate the projections at 45° and 90°.

for one projection. Each feature in the distribution will have a sinusoidal contribution to the sinogram, where the distance from the rotation center defines the amplitude and the polar angle of the feature's location the phase. An example sinogram is shown in figure 2.15.

The most popular reconstruction method is the so-called filtered back-projection (FBP), which is based on the Fourier slice theorem and Radon transform [76, 77]. The basic idea is to back-project the recorded projection of each angle along its respective imaging axis. However, since the projection values are always positive, doing so will smear out the reconstructed image. It can be shown that this naive back-projection will result in a point spread function of $1/|r|$ [78]. Instead, a filter has to be applied to the projection before performing the back-projection. When applied in the frequency domain, the filter is a simple ramp function, resulting in a high-pass filter. The filtering step is therefore performed by applying a Fourier transform on the absorption profile $p(x)$

$$f(q) = \mathcal{F}(p(x))\,, \tag{2.11}$$

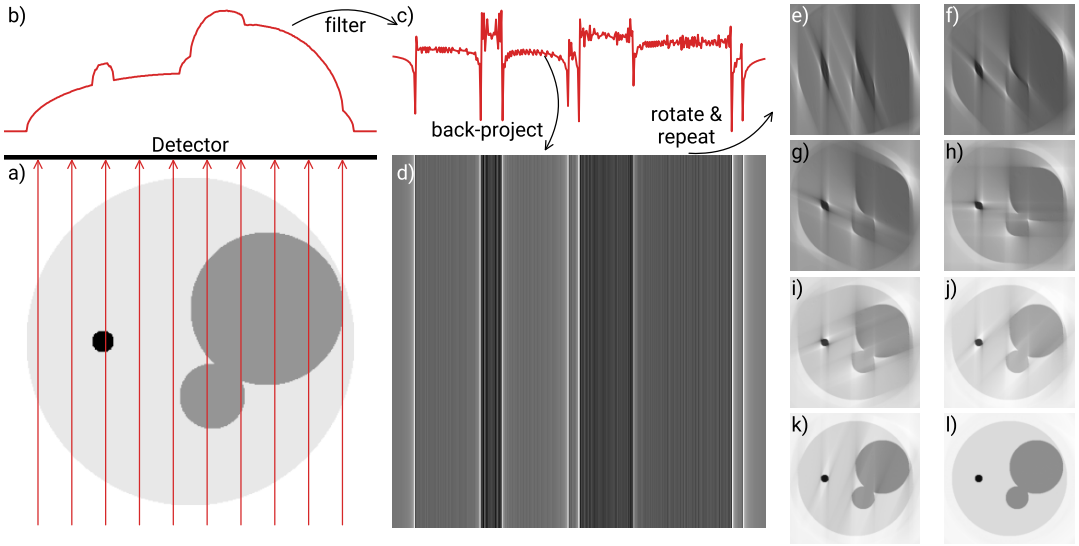

Figure 2.16 – Principle of the filtered back-projection. The object is imaged along one axis (a), resulting in the absorption projection (b). A ramp filter is applied in the frequency domain (c) before back-projecting it (d). These steps are repeated for rotations along 180° (e-l) to reconstruct the original geometry.

applying the filter

$$g(q) = f(q) \cdot w(q)\,, \qquad \text{typically } w(q) = |q| \tag{2.12}$$

and back-transforming the filtered frequency spectrum into the real space

$$\tilde{p}(x) = \mathcal{F}^{-1}(g(q))\,. \tag{2.13}$$

The process of FBP is schematically shown in figure 2.16.

Figure 2.17 shows the difference in the reconstruction result between a naive back-projection and a filtered back-projection.

When dealing with real data, absorption profiles are noisy due to statistical fluctuations. Since these fluctuations are occurring for each pixel, they contribute at high frequencies

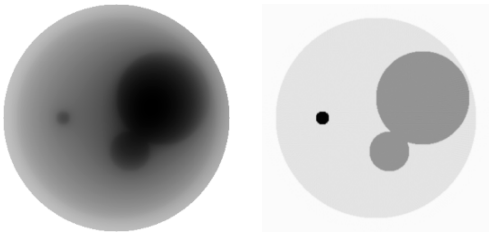

Figure 2.17 – Comparison between naive back-projection (left) and filtered back-projection (right).

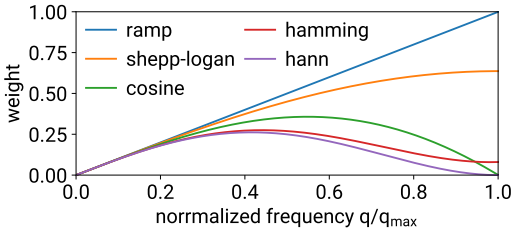

Figure 2.18 – Shape of typically used filters in FBP. While the ramp acts as a high-pass filter, the others also suppress the highest frequencies.

in the Fourier-transformed spectrum. By switching from a ramp filter to a different weighting function, a bandpass filter can be used to reduce the noise level. However, this does also eliminate the response to real high-frequency changes and reduces the image quality and must be chosen with care. A selection of typically used filters is shown in figure 2.18.

Today, often iterative reconstruction methods are applied instead of the FBP. In these methods, the imaging process is expressed as a set of linear equations, describing the effect of attenuation in each pixel in the object on the signal of each detector pixel and projection. Solving this set of equations is a sparse inversion problem and many algorithms can be used for such a task, such as maximum likelihood (ML) estimation, singular value decomposition (SVD), or algebraic reconstruction techniques (ART). The advantage of such an approach over the FBP is that secondary or geometrical effects such as beam hardening or non-isotropic incident spectra can be included in the imaging matrix and that these algorithms do work on incomplete datasets, meaning that they do not need coverage over the full 180° and can better handle artifacts such as metal parts [79].

2.3.2 Computed Tomosynthesis

Derived from CT, in recent years computed tomosynthesis (TS) has evolved as a clinical alternative fueled by advances in digital imaging detectors and is today mostly used for mammography [80]. In TS, similar to CT, projections are acquired from many different angles, however no full 180° coverage is needed and the reconstruction plane is parallel to the detector, not axial as in CT. While different variations of TS exist, its principle can easily be understood when using a fixed large detector and a translating x-ray source. The principle is shown in figure 2.19. Depending on the depth of a feature in the object and the placement of the x-ray source, the position of the feature's projection onto the detector changes. For reconstruction of a given depth, the image of each projection is shifted and stretched such that the features at this depth overlap in all images. Since this is only valid at exactly the selected depth, features in the front or back are not overlapping but appear out of focus. This method is called shift-and-add. In practice, the detector is often not fixed but moved with the source, allowing it to be smaller and cheaper. Furthermore, iterative reconstruction methods can be used to improve the image quality [81].

In comparison to CT, TS has more artifacts along the beam axis as a result of the out-of-focus contributions. However, it offers the advantage to require a lower radiation dose as the signal does not have to be extracted from each projection, but from a sum of all projections which reduces the statistical fluctuations in the attenuation processes. Tomosynthesis is thus a viable alternative to CT, when minimal radiation dose is critical or when projection images can only be acquired from a small angular interval and is often employed for mammography or chest imaging [82].

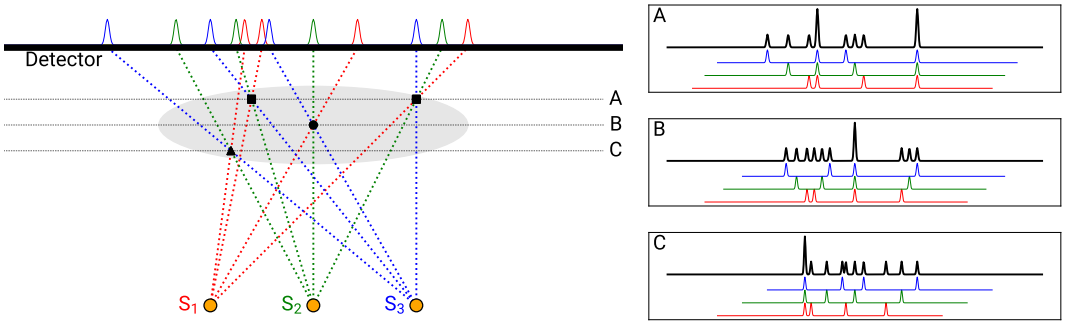

Figure 2.19 – Principle of the tomosynthesis using shift-and-add. Projections are acquired from different x-ray source positions S_i onto a fixed detector. On the right, the shifted profiles depending on the depth that shall be recovered are shown in red, green, and blue, while the black line depicts the summed profile. Objects at other depths are out of focus and therefore blurred.

2.4 Principles of Synchrotron-based XFI

As discussed in chapter 2.1.3, the emitted x-ray fluorescence spectrum is unique for each element, and thus can be used for destruction-free elemental analysis of substances, named x-ray fluorescence analysis (XRF). It is therefore often used in a wide variety of applications, including food quality inspections, history of arts, security, geology, and also in-vitro cell labeling [46, 83–87]. However, it is predominantly used to analyze thin layers of material or surface compositions. In such cases, low-energy photons can be used, as attenuation inside the sample is of no concern. By using K-shell fluorescence for light elements and L-shell fluorescence for high-Z elements, it is possible to distinguish nearly all elements by their fluorescence spectrum between 1 and 15 keV.

In contrast, in x-ray fluorescence imaging - i.e. the usage of XRF for medical imaging - the fluorescence is used to probe deep into tissue, meaning that attenuation of both the incident beam and the emitted fluorescence has to be taken into account. Additionally, radiation dose is of concern and has to be kept low. By moving to higher-energy

fluorescence lines, attenuation effects but also fluorescence production cross sections are be reduced. The selection of the optimal marker is thus complex and strongly target-dependent and generally heavier elements should be used for thicker samples. For mouse-sized objects, elements around $Z = 50$ are optimal [88], while heavier elements such as gold might be used for XFI in humans [37, 47]. Table 2.1 lists elements that have been used previously or are promising candidates for XFI and their respective fluorescence energy. Biological and chemical constraints limit the use of possible fluorescence markers for biomedical applications, most prominently the requirements of being non-toxic to the organism and allowing good handling of the substance [89]. Additionally, experiment-specific limitations have to be considered. As tin ($Z = 50$) is used as solder in electronic components, many detectors might have an intrinsic tin fluorescence signal, prohibiting the use of tin markers albeit being a promising candidate based on attenuation considerations. Furthermore, the fluorescence marker has to be tuned to the incident beam's energy. As shown in figure 2.12, incident photons in the range between 50 and 70 keV deposit the lowest dose per fixed photon fluence for small animal-sized objects, making it reasonable to optimize the marker selection for such incident energies.

While in absorption imaging the focus of the primary source can be used to directly perform 2D imaging of an object, this is not possible for a secondary process such as fluorescence generation. Instead, focusing lenses would be needed to directly obtain 2D fluorescence images. However, in the hard x-ray regime such optics do not exist[‡]. Thus, scanning methods have to be employed to obtain 2D (or 3D) information. This scanning can be performed either on the detector side, meaning the full sample is irradiated but the detector is collimated to only a small region inside the sample [94], or on the source side, i.e. using a pin beam to probe the sample [90, 92, 93]. The latter method strongly

[‡]Optics in the hard x-ray regime are either based on Bragg diffraction or grazing incidence reflection, both requiring small angles and can thus only collect photons from a very small solid angle, making them unsuitable for XFI.

Table 2.1 – Selection of previously used or promising elements for XFI

Element	Fluorescence Energy
Au (L-shell) [90]	$9 - 11\,\mathrm{keV}$
Mo [40, 42]	$17.4\,\mathrm{keV}$
Pd [39]	$21.1\,\mathrm{keV}$
I [91]	$28.6\,\mathrm{keV}$
Ba [92]	$32.2\,\mathrm{keV}$
Gd [91, 92]	$43.0\,\mathrm{keV}$
Au (K-shell) [37, 39, 47, 92–94]	$68.8\,\mathrm{keV}$

reduces the radiation dose and is thus the only feasible method when targeting in-vivo applications. Alternatively, a combination of pixelated detectors and pinhole collimators has been proposed [41, 95], building a camera obscura imaging geometry. This removes the need for x-y-scanning and thus promises shorter imaging durations. However, to obtain a reasonable spatial resolution, the pinhole has to be below 1 mm diameter, resulting in a small covered solid angle and thus low sensitivity. Consequently, such an imaging geometry is not suitable for cell tracking or similar applications with low fluorescence marker concentrations.

Scan-based imaging methods are inherently slow but for in-vivo imaging, the possible duration of anesthesia has to be taken into account, which is typically around one hour [96]. To keep the imaging duration within this time limit, a primary source with a high photon flux is needed to allow for short measurement intervals per scan point.

Furthermore, thick samples translate into a much more dominating Compton scattering contribution, where it is not only likely that Compton scattering occurs but it is even expected that a photon will scatter multiple times inside the sample before being detected,

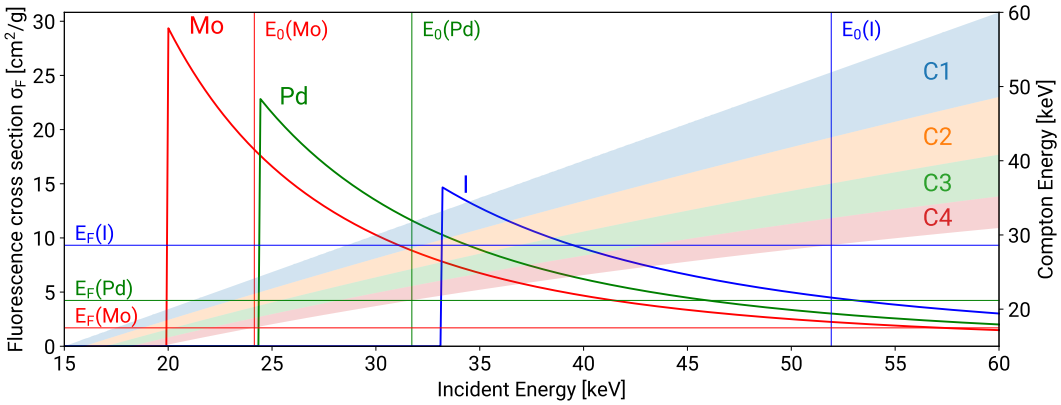

Figure 2.20 – K_α fluorescence cross sections for selected elements compared to energy intervals in which background by (multiple) Compton scattering is expected. Horizontal lines indicate the energy of the corresponding fluorescence line and vertical lines indicate the minimum incident energy for which the fluorescence is below the Compton interval.

losing more energy during each scattering. Thus, a wide region of the spectrum will be dominated by Compton-scattering background and small fluorescence signals in this region cannot be distinguished. When designing an XFI experiment, the goal is therefore not only to maximize the fluorescence signal but also to shape the Compton spectrum such that the fluorescence signal is most significant. When using a polychromatic primary source - such as an x-ray tube - the Compton scattered photons cannot be confined into an energy region but will be spread across the whole spectrum, meaning that the fluorescence signal will always have a strong background. Mono-energetic sources are thus critical for achieving a high sensitivity in XFI. Figure 2.20 indicates the Compton scattering region up to the 4th order for different mono-energetic incident energies as well as the fluorescence cross sections for possible markers around $Z = 50$.

Combining all these aspects, an intense mono-energetic hard x-ray pin beam is required to achieve optimal sensitivity in XFI. Such a source is today only available at synchrotrons. As access to synchrotrons is sparse, this limits the broad usage for XFI and there have

been attempts to adapt conventional x-ray tubes for XFI applications. Most notably, a multi-layer mirror can be used to filter a specific energy and focus the diverging beam of the x-ray tube [40, 42, 97]. While this method can be used to obtain a mono-energetic pin beam, multi-layer mirrors only work at grazing incidence and only a very small fraction of the photons emitted by the source can be collected. Moreover, multi-layer mirrors are limited to approximately 30 keV before the reflectance becomes too low. Using this technique, a flux of 3×10^7 photons/ sec at 24 keV incident energy has been achieved [40], approximately 10000 times less than what is achievable at synchrotrons.

Alternatively, focusing collimators at the detector can be used to filter out most of the multi-scattering background. With this setup, XFI can be performed without a mono-energetic incident spectrum but such a collimator will also block large portions of the fluorescence signal, reducing the overall sensitivity [94].

While such experiments do show that XFI can be performed without synchrotron access, it is needed to achieve the highest sensitivities. As the total fluorescence marker mass in cell tracking or pharmacokinetics is expected to be 3 orders of magnitude lower than when injecting free nanoparticles [38], synchrotrons are the ideal tool for such experiments and cannot be replaced by today's laboratory sources.

2.5 X-Ray Detectors

For the detection and elemental classification of x-ray fluorescence, an energy-resolving detector is needed. Typically, semiconductor detectors based on silicon or cadmium telluride (CdTe) crystals are used for this application. These crystals are usually between a few hundred µm up to some mm thick and a high gradient electric field is applied by external electrodes [98].

When an incoming photon interacts with the detector material, electrons are excited from the valence to the conductor band, generating an electron-hole-pair. Due to the electric field, the electrons are drifting towards the anode and the holes towards the cathode. As described in the Shockley-Ramo theorem [99, 100], these moving charge carriers inside the field induce a current in the electrodes which is proportional to the energy of the incoming photon. This signal can be fed into an amplifier chain to obtain an energy-resolved x-ray spectrum using the pulse height of each event [98, 101, 102].

Depending on the choice of the semiconductor, different effects are dominating the recorded spectra.

2.5.1 Properties of CdTe Detectors

Due to the high atomic numbers of the compounds' constituents, CdTe detectors have a high photoabsorption cross section, meaning that they offer good detection efficiencies at high energies and can typically be used up to 200 keV. However, compound crystals have more defects in their lattice than elemental crystals, which predominantly reduces the lifetime and mobility of holes [98]. When holes become trapped, the signal contributions from the cathode are reduced. This hole tailing is especially likely when the electron-hole pair is created close to the anode, i.e. deep in the chip. For higher-energetic photons, the mean free path in the detector crystal becomes larger, resulting in a higher probability of trapped charges. The overall charge collection efficiency can be modeled using the Hecht equation [103], given as

$$\eta(x) = \frac{\lambda_e}{d}\left(1 - e^{-(d-x)/\lambda_e}\right) + \frac{\lambda_h}{d}\left(1 - e^{-x/\lambda_h}\right) \tag{2.14}$$

with $\lambda_{e/h}$ describing the trapping length for electrons and holes, x the depth inside the detector at which the charge cloud was generated, and d the total thickness of the detector. The effect of hole tailing on the peak shape can be neglected below 30 keV,

while small asymmetries are visible for higher energies. Starting at around 60 keV, a peak is followed by a lower-energetic tail. Detected peak shapes for different energies are shown in figure 2.21.

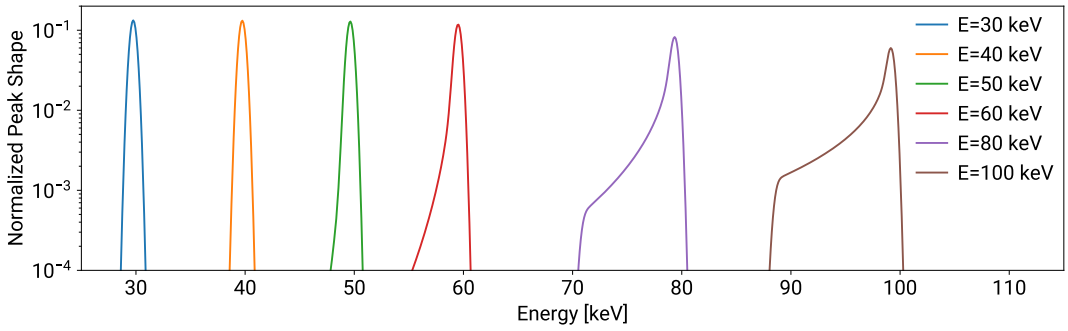

Figure 2.21 – Influence of the hole tailing effect on the detected peak shape for a 2 mm thick CdTe detector with $\lambda_e = 13.2\,\text{cm}$, $\lambda_h = 0.8\,\text{cm}$, and a resolution of 700 eV FWHM, matching the Amptek XR-100CdTe detector.

The relatively low mobility of the charge carriers in CdTe further requires amplifier shaping times of approximately 1 µs. Long shaping times increase the electronic noise contribution to the energy resolution and limit the maximum count rate without significant deadtime [104]. Due to this effect, count rates are limited to 30 000 cps and the energy resolution at 25 keV is typically in the order of 700 eV full width at half maximum (FWHM).

Another effect of the high atomic numbers of the detector's constituents is the increased fluorescence cross section, resulting in the presence of escape peaks. When the incoming photon is absorbed by the detector, a fluorescence photon may be emitted which leaves the detector undetected. In this case, the recorded energy corresponds to the incident photon's energy minus the fluorescence energy E_F of the photon. This process is only possible when the incident photon's energy is larger than the binding energy E_B of the

Table 2.2 – Binding and most prominent fluorescence energies for Cd and Te. Data taken from [54].

Element	E_B [keV]	E_F^{KL3} [keV]	E_F^{KL2} [keV]	E_F^{KM3} [keV]	E_F^{KM2} [keV]
Cd	26.71	23.17	22.98	26.09	26.06
Te	31.81	27.47	27.20	31.00	30.94

electron [104].

Table 2.2 lists the binding as well as the fluorescence energies for cadmium and tellurium. The fluorescence energies have a range of approximately 8 keV, meaning that every real peak will generate a corresponding escape region consisting of various peaks across 8 keV width at lower energies. Thus, high-energetic events will contribute to the background level in a lower energy region.

2.5.2 Properties of Silicon Detectors

In comparison, silicon provides much better electron and hole mobility and high purity, thus hole tailing is of no concern.

Modern silicon detectors are not using a planar structure for anode and cathode (PIN diode), but instead silicon drift detectors (SDD) are used. In a silicon drift detector, the electric field inside the crystal is shaped by drift rings to guide the electron cloud towards a small anode in the center of the chip. This geometry reduces the overall capacitance of the anode, allowing for shorter peaking times and thus lower electronic noise and higher maximum count rates. With SDDs, count rates of 500 kcps and an energy resolution of 260 eV FWHM at 25 keV are achievable [98, 101, 105]. However, they require a very

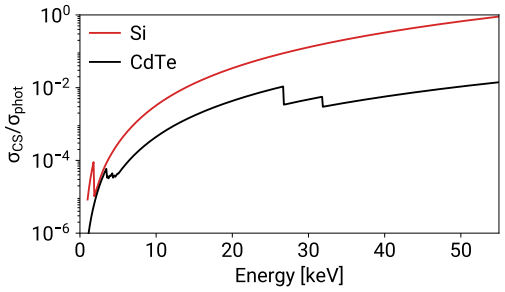

Figure 2.22 – Ratio between Compton and photoabsorption cross section for Si and CdTe. Data taken from [54].

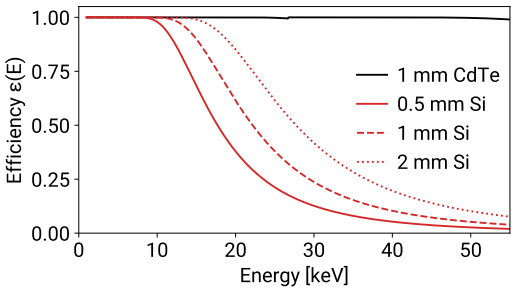

Figure 2.23 – Detection Efficiency for 0.5 and 1 mm Si and 1 mm CdTe. Calculated using data from [54].

high-quality silicon crystal and are therefore limited to small thicknesses. Typically, 300-500 µm are available, but thicker chips up to 2 mm are currently in development [106]. Combined with the lower photoabsorption cross section of Si compared to CdTe, this results in a low efficiency for higher energies as shown in figure 2.23, typically restricting the use of SDDs to ≤ 30 keV [104].

Due to the low Z of silicon, the photoabsorption cross section is lower, and the ratio $\sigma_{CS}/\sigma_{phot}$ - shown in figure 2.22 - is higher than in CdTe, meaning that it is more likely that an incident photon only deposits parts of its energy in the detector via Compton scattering. This is especially the case for high-energetic incident photons where it is likely that the Compton scattered photon does not get absorbed by the detector. In such events, the recorded energy is only given by the Compton electron. Based on eq. 2.1, the maximum transferred energy onto the electron in such an event is given as

$$E_e = E_\gamma \left(1 - \frac{1}{1 + 2\frac{E_\gamma}{m_e c^2}}\right) . \tag{2.15}$$

For a 50 keV incident photon, this results in a maximum recorded energy of 8.2 keV for such events. This effect will thus generate background contributions at the lowest end of

the spectrum.

2.5.3 Detector Selection for XFI

When selecting the optimal detector, all the properties above have to be taken into account and compared to the requirements. In the case of synchrotron-based pre-clinical XFI introduced in chapter 2.4, the use of incident energies between 50 and 60 keV and markers with fluorescence between 20 and 30 keV are ideal. Furthermore, a high count rate is required for the goal of in-vivo measurements, as the total scan duration has to be within the limits of typical anesthesia times. Additionally, a low efficiency increases the radiation dose that is needed for a detectable signal. It is not possible, to select a detector, which fulfills all these requirements, hence a trade-off has to be made.

Figure 2.24 shows the response of both, an SDD and CdTe detector to the same fluorescence reference target, consisting of a 1 mm thick Si substrate coated with approximately 10 nm Ag. While this target provides much less Compton scattering background than mouse-sized objects, it can already be seen that the escape events of the CdTe detector drastically increase the background in the targeted fluorescence energy range between 20 and 30 keV and small fluorescence signals would not be detectable. Based on this issue, silicon detectors are the best suiting choice for XFI, even though the low efficiency increases the required radiation dose. In contrast, the silicon efficiency curve is beneficial for the count rate, which is dominated by the high-energy Compton counts, where the efficiency is only a few percent (see figure 2.23), allowing to operate the experiment at a high incident flux and keeping the scan durations short.

During the course of this thesis, two different detectors have been available, namely a 1 mm thick CdTe detector with an active area of $5 \times 5\,\mathrm{mm}^2$ (XR-100CdTe, Amptek, Bedford, MA, USA) connected to a PX5 multi-channel analyzer readout (Amptek, Bedford,

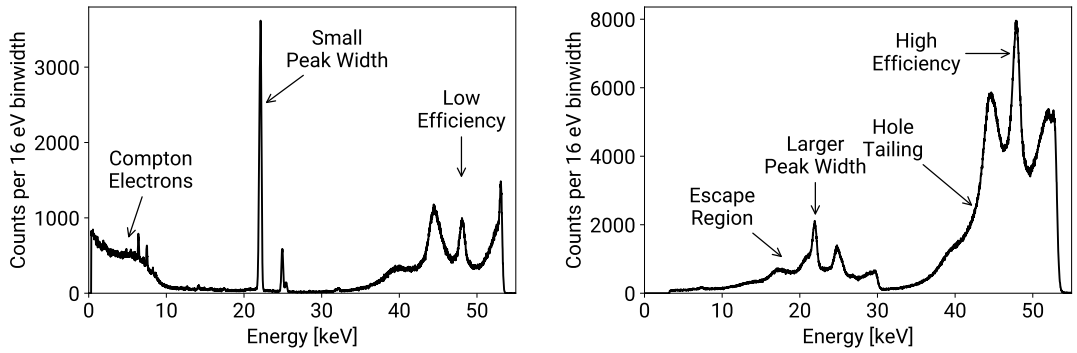

(a) 0.5 mm thick silicon drift detector spectrum.

(b) 1 mm thick CdTe detector spectrum.

Figure 2.24 – Comparison of spectra obtained with a CdTe and silicon drift detector from the same 1 mm thick Si substrate coated with approximately 10 nm Ag, showing characteristic detector effects for the different types of detector.

MA, USA) and a 0.5 mm thick silicon drift detector with an active area of 70 mm^2, collimated to 50 mm^2 with included readout electronics (X-123 FastSDD, Amptek, Bedford, MA, USA). The X-123 contains the same readout electronics as the PX5 unit. For a maximum dead time of 20%, count rates are limited to around 30 kcps and 300 kcps, respectively. Due to the aforementioned detector effects, the CdTe detector is not suitable for fluorescence measurements between 20 and 30 keV but allows to obtain the Compton spectrum with high efficiency which can be used to obtain anatomical information. The detector was typically placed further away than the SDD to account for its lower maximum count rate.

In 2022, six additional detectors have become available. These are prototype units provided by Amptek, which are based on the XR-100 FastSDD but use a 1 mm thick silicon sensor. They contain a 70 mm^2 detector chip, collimated to 50 mm^2. Each detector is connected to a PX5 readout box. They have been used for the measurements described in chapter 5.

3 Methods

3.1 Geant4 Simulations

For the preparation of experiments as well as systematic studies, simulations based on the Geant4 toolkit [107–109] have been performed. Geant4 provides a framework to create Monte Carlo simulations for particle-matter interactions and is used across many domains, from particle- and astrophysics to medical applications. Different so-called physics lists are available, which describe the models for the interactions between different particles and it is important to choose the best matching model, depending on the particles to be simulated as well as the energy range. In the case of synchrotron-based XFI, only interactions of photons and electrons with energies between 1-100 keV are simulated. However, the model has to be able to account for polarization. For these requirements, only the 'polarized Livermore' physics model is appropriate [110].

Inside the simulation, geometries of the detectors in use in our experiments have been defined based on available information [111, 112]. Figure 3.1 shows a side view of the implemented detector structure. The main components are the steel baseplate, a thermoelectric cooler, a ceramic substrate, the detector crystal, and the beryllium window. The SDD detector additionally has a multi-layer collimator in front of the chip. Not all material compositions of the components are known and in part had to be assumed based on typically used materials as well as comparisons between simulation results and data. Due to the low detection efficiency of the SDD, the response of its detector model is more sensitive to the surrounding geometries, as many photons will initially pass through

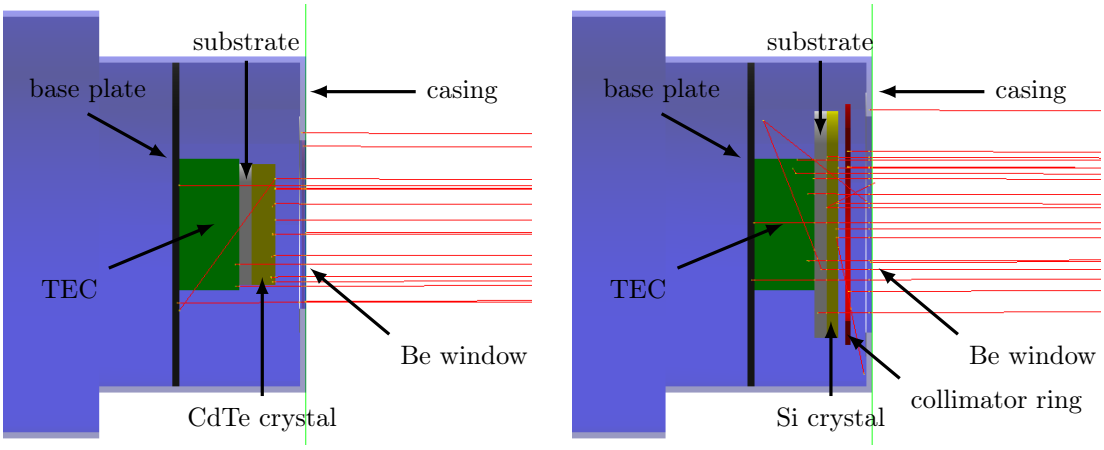

(a) Amptek CdTe detector layout

(b) Amptek 0.5 mm SDD detector layout

Figure 3.1 – Geometries of the different detector heads implemented in Geant4. The main difference between the CdTe and SDD layout is the bigger chip and the multilayer collimator ring in the SDD. Red tracks indicate simulated 30 keV photons demonstrating the difference in detection efficiency of the two detector materials.

the detector chip and can interact with the lower layers, at which they might be back-scattered into the crystal. Such events are also visible in figure 3.1.

The simulation output for each detector consists of two individual datasets, namely the true data and the recorded data. For the true data, information is collected whenever a particle track intersects the detector's sensor geometry. At this point, the state of the particle is queried to obtain information like its energy, its momentum, its particle type, the process that created it, or the number of times it has scattered before. This information is helpful for the design of experiments and provides insights into the governing processes, but one would not be able to directly obtain those in an experiment. The second dataset corresponds to the data, which could be experimentally measured, namely the deposited energy of each simulated event in the chip. For cadmium telluride detectors, the deposited energy is corrected for the hole tailing effect using the depth of

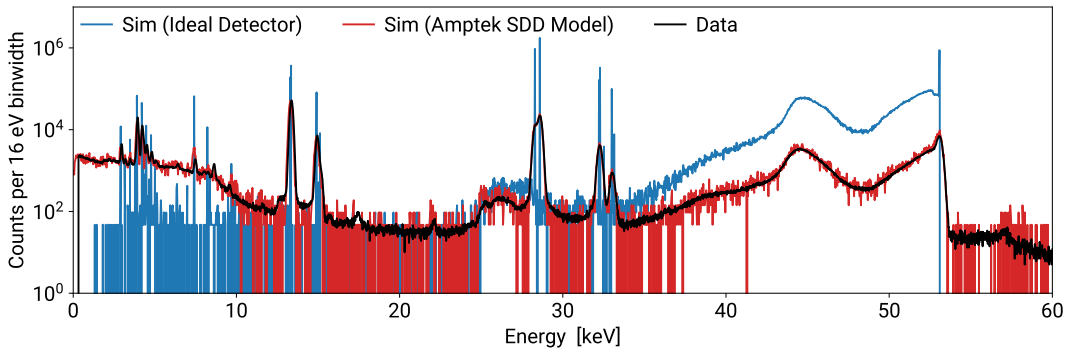

Figure 3.2 – Comparison between measured and simulated spectra of the reference target geometry (see chapter 3.5) using an ideal detector (blue) and the Amptek SDD detector model (red). Simulated spectra are scaled to the same number of incident photons as used for the experiment.

the interaction inside the chip and the Hecht equation as described in chapter 2.5.

Effects like the detector's energy resolution or pileup - which do not need information only available inside the simulation - are not built into the simulation but are applied during a post-processing step when the output is converted into histograms.

The detector models have been tested against experimental data to guarantee good agreement between simulations and measurements, as shown in figure 3.2. The difference between the response of an ideal detector and the detailed detector model demonstrates the importance of a good understanding of the detector's behavior for realistic simulations. This is a critical requirement for the simulations, as they are used for preliminary planning and optimization of experiments.

3.2 Experimental Setup

3.2.1 Beamline Layout

Synchrotron experiments were performed at the P21.1 beamline at the Petra III synchrotron (DESY, Hamburg, Germany). This beamline is a fixed-angle side branch beamline offering 53 or 101 keV incident energy [113, 114]. It is primarily designed for high-energy x-ray diffraction experiments but can also be used for custom experiments - such as XFI - as it offers large free space for special instrumentation. In figure 3.3 the layout of the beamline with its most important components is shown. At its center, a heavy load diffractometer with x-y-z translation, as well as a rotation stage along the vertical axis and a double tilt stage (Huber, Rimsting, Germany) is available. The incident beam can be collimated down to 0.1 x 0.1 mm^2 using an x-y slit system and attenuated via a binary absorber battery with 6 elements, each one having twice the thickness of the previous element. This allows choosing between 63 multiples of 0.1 mm tantalum in the beam path [115]. At 53 keV, each absorber unit corresponds to a transmission factor of approximately 42.6%. The absorber battery is placed about 2 meters in front of the sample position. To minimize beam broadening by scattering in the air, a vacuum beam pipe is placed between the absorber and diffractometer.

The incident flux can be monitored by several 500 µm silicon PIN diodes [115]. The induced current is read out by amperemeters providing an online display in the control hutch and a proportional voltage output, which is fed into voltage-to-frequency converters. These pulses can then be integrated by timer-gated counters. This acquisition chain for the diode current provides a very simple-to-use way to record the integrated flux for data acquisition and filters any short-period noise or oscillations. In total, three diodes are placed in the beam path. The first one is positioned in front of the final monochromator in the optics hutch and therefore can be used to monitor the storage ring and

undulator performance. The two other diodes are present in the experimental hutch. Their position has changed between different experiments. Possible placements are in front of the primary slits, between the slits and absorbers, after the absorbers, or after the sample. The current induced in these diodes is directly proportional to the incident flux on (and transmission of in case of the last diode) the sample and they are therefore the most crucial ones for radiation dose-sensitive experiments.

The final component about 1.5 meters downstream is the so-called x-ray eye. This detector is an in-house development at DESY and consists of a 45° angled scintillator in the beam path and a camera placed at 90° facing the screen, allowing spatially resolved imaging of the transmitted beam. The resolution is in the order of 50 µm, however, the scintillator is much less sensitive than the PIN diodes. This detector is primarily intended to provide navigation during experimental setup and not scientific data-taking. However, it has proven to be a valuable tool to obtain high-resolution transmission images of the samples. A more in-depth description of an earlier version of this detector can be found in [116].

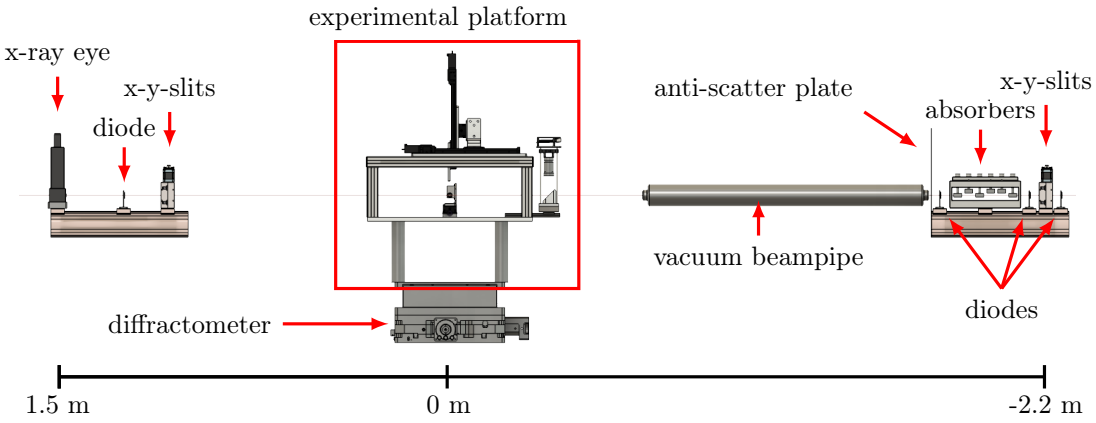

Figure 3.3 – Schematic layout of the experimental hutch at the P21.1 beamline at PETRA III containing the relevant components used in XFI measurements. Note, that not all but only two of the marked diode positions were populated during any beamtime. The incident beam is coming from the right. Marked distances are only an approximation and changed between beamtimes.

3.2.2 XFI Platform

The custom experimental platform for XFI measurements is placed on top of the diffractometer. An earlier version of this stage was presented in [88]. The central element of the platform is a 600 mm × 800 mm wide aluminum plate having circular arranged mounting holes with 5° spacing. This allows for variable placing of the detectors, either on motorized axes or at fixed distances. In the center, the plate has a 100 mm diameter hole which can optionally be closed with an iron inlay. This hole provides space for taller samples as well as a reduction in Compton scattering background. The platform is aligned such that the incident beam passes at a height of 80 mm above the plate. A motorized Cartesian gantry is mounted on top of the plate, allowing for x-y-z translation of the sample. In front of the sample, an on-axis camera is placed, providing a parallax-free view onto the target with respect to the beam. This camera is described in more detail in chapter 3.2.4.

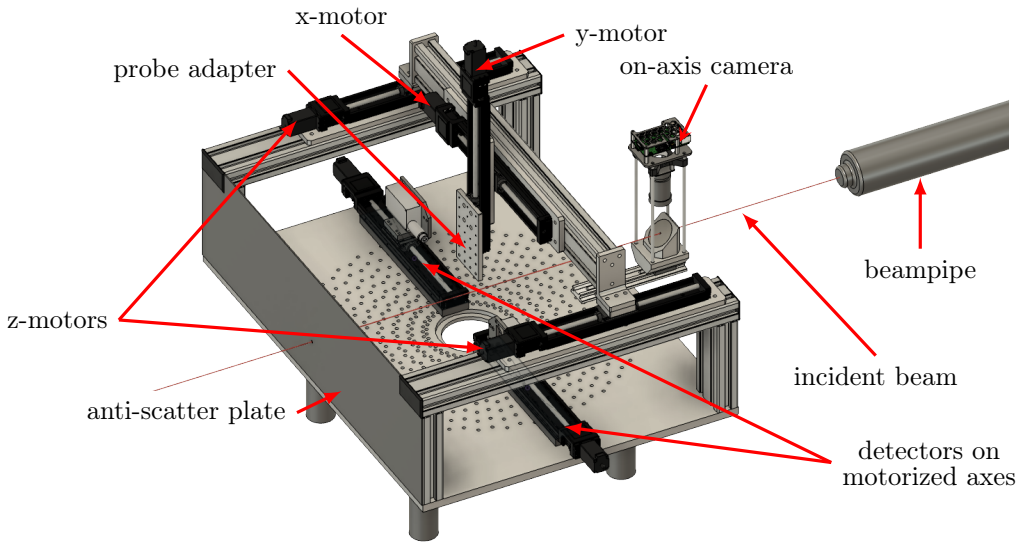

Figure 3.4 – Render of the experimental platform in one example configuration with two detectors placed at ±90°.

Behind the sample, the platform can be closed off using a 2 mm thick steel sheet with a 5 mm diameter hole at beam height, preventing any influence from back-scattering at components of the beamline downstream. This plate is especially important when placing detectors at greater than 90° scattering angle, i.e. facing the chip in the downstream direction. An example configuration of the platform is shown in figure 3.4.

3.2.3 DAQ Software

With XFI being a niche application, synchrotron beamlines do not offer ready-to-use software and scripts that allow automated measurements. Additionally, dedicated detectors and other hardware have to be integrated into the system, requiring the development

of a custom solution for XFI experiments.

Tango Controls

Tango Controls [117] is used at the P21.1 beamline as the Supervisory Control and Data Acquisition (SCADA) system. It provides a homogeneous interface to access nearly every component of the beamline, including motors, detectors, or absorbers. To provide one common interface for both beamline and experiment equipment, Tango was also chosen as the control system for the XFI platform and our data acquisition system, making the distinction between beamline and custom components transparent to the user. Therefore, the overall architecture of the acquisition software was dictated by the concepts of Tango.

In Tango, different entities of the control system are implemented as independently running processes, called Device Server. A device server can be anything from an interface to a hardware component (such as a motor or detector) up to high-level software orchestrating multiple other devices. Tango servers can communicate with each other via a dedicated network protocol over which commands can be invoked and attributes can be queried. A special device server is the `DatabaseDS` server, which interfaces with a MySQL database and manages the configuration of the overall control system. Each new Tango device server has to be registered in this database, and it can be used to restore device states after a restart. Tango is designed to be a distributed control system, therefore both, clients and servers, can be running on the same host as the database server or on different hosts. Additionally, it allows devices registered in one database to communicate with servers registered in a different database. This feature provides the possibility to run an own Tango instance for the experiment while still being able to access beamline components. Figure 3.5 provides an overview of the overall control system layout.

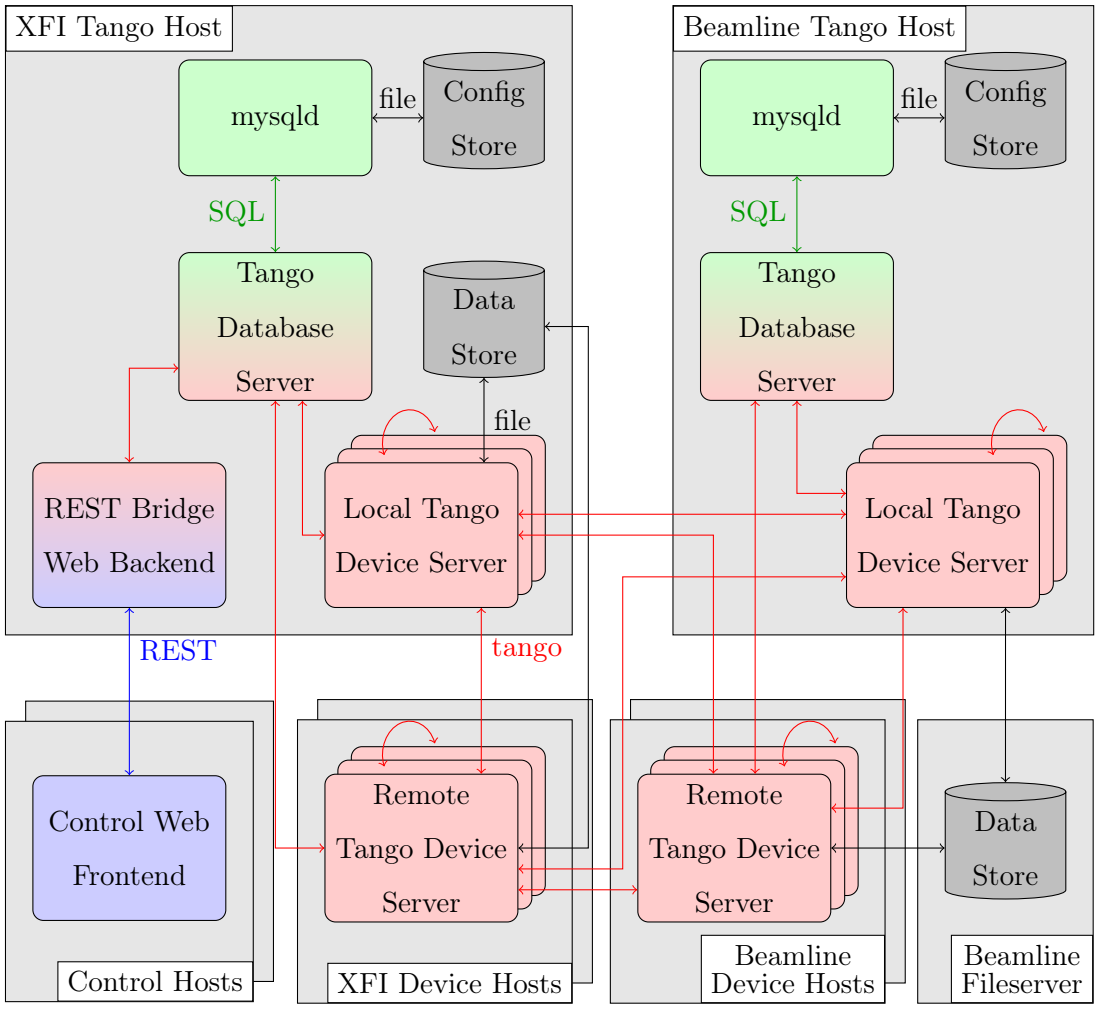

Figure 3.5 – High-level architecture of the Tango-based control system. The different communication paths are indicated by the arrows color-coded based on the used protocol.

On top of this standard Tango design, a custom backend was developed which hosts a web server and acts as a bridge between REST queries and the Tango ecosystem. This bridge allows to run the user interface via a web browser, providing easy access to the control system - most importantly from the beamline control room, where no custom software can be installed as a beamline user.

Device servers have been developed for the Amptek detectors implementing the DP5 communication protocol [118] and for the TMCM6212 stepper motor controller (Trinamic, Hamburg, Germany) following the TMCL protocol [119]. Attributes and commands for the TMCM6212 device server have been adopted from the Tango devices to control the motors at the beamline, and thus there is no difference between controlling a custom or beamline motor on the client side.

Scan Interface

On the highest abstraction level, a scan interface was implemented as a Tango device. This device can be used to coordinate low-level devices such as motors and detectors for measurements, enabling 1D, 2D, and 3D scans. It was designed to be as flexible as possible to allow fast integration of new detectors or motion systems. Additionally, parameters describing the current state of the setup are logged at each scan position. This includes the position of each motor, as well as the output of the counters connected to the PIN diodes. Two different scan modes are implemented: In step-scanning mode, motors are moved to each scan position and the acquisition phase starts when the motors have reached their target position. Only after the acquisition is finished, the motors are moved to the next position. However, for short acquisition periods, motor movements are dominating the total scan duration. Typically, motor accelerations are limited to around $10\,\mathrm{mm/s^2}$ to prevent any vibrations of the target. This results in an overhead of around $0.5\,\mathrm{s}$ to each scan position. In continuous scanning mode, acquisition is performed while

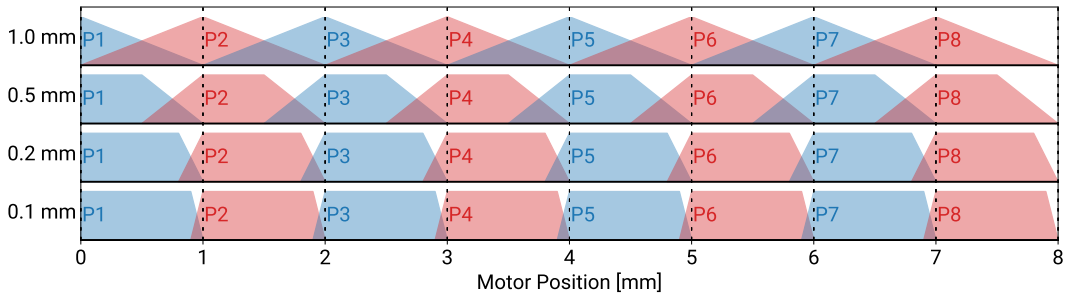

Figure 3.6 – Contribution at each position to a scan pixel in continuous scans for various beam widths. The acquisition is started, when the front of the beam crosses the pixel border (marked as vertical lines).

the motors are moving and their speed is adjusted such that the width of each pixel is passed in the defined acquisition duration. This mode removes the time overhead between scan positions and therefore provides relevant time savings when the acquisition time per pixel is similar to the overhead duration. For a mouse-sized scan (100×30 mm) this overhead sums up to about 25 minutes. However, in continuous mode, parts of the beam will illuminate adjacent pixel positions during the acquisition (see figure 3.6), resulting in smearing along the scan axis. To reduce this effect, the beam width has to be small compared to the pixel width. Therefore, for typical scans with 1 mm pixel size, beam widths between 0.1 and 0.2 mm were used.

3.2.4 On-Axis Camera

To aid alignment of the samples with respect to the beam, a camera assembly, shown in figure 3.7, was developed which provides a parallax-free view onto the sample. This is achieved by using a tilted 50 mm diameter mirror with a 45° tapered central bore (OptoSigma, Les Ulis, France) to let the incident beam pass through. Above the mirror, a Raspberry Pi 4 connected to a Raspberry Pi HQ Camera module with a fixed 16 mm focal

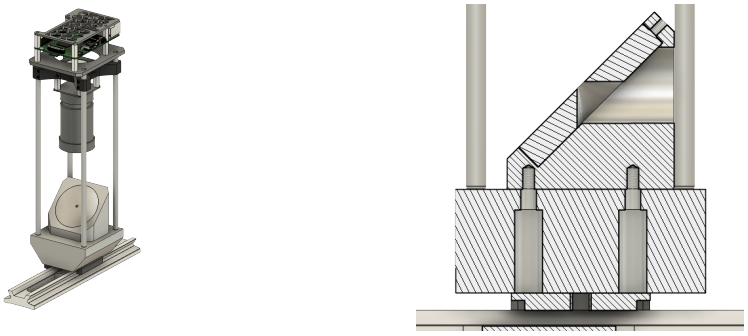

(a) Render of the camera assembly

(b) Cross-section of the mirror and its mount.

Figure 3.7 – Drawings of the on-axis camera

length lens is mounted. While this camera is not suitable for scientific measurements, it is sufficient for its purpose of monitoring the experiment. Depending on the position of the camera assembly on the stage, a field of view of up to 240 mm × 180 mm at the center plane is achievable, providing a good overview of the sample and detector placement. Components are assembled using a 60 mm optical cage system (Thorlabs, NJ, USA) and placed on an optical rail (FLS 40, Qioptic, Göttingen, Germany). By using a Raspberry Pi instead of an industrial/scientific camera, the total cost is kept low and the Tango server can be run directly on the device itself and no additional dedicated server hardware is required for the integration into the acquisition system. Therefore, this setup is well suited for monitoring tasks where no high requirements on image quality and camera features are present.

3.2.5 Standard Phantoms

Two standard phantoms have been used repeatedly for simulations and experiments in the past [59] and during the course of this thesis. In cases that require a well-defined geometry, a 45 mm tall PMMA cylinder with 40 mm diameter is available. The cylinder

has 3 slots in which standard 1.5 ml or 2 ml Eppendorf tubes can be placed. PMMA has similar x-ray attenuation properties as tissue and is therefore often used in standard phantoms with comparable sizes in XFI [91, 93, 94]. The diameter has been chosen to be similar to a mouse but offering enough space for multiple Eppendorf tubes. These tubes can be filled with different marker concentrations for systematic studies. Figure 3.8 shows a drawing of the cylinder phantom.

As a second phantom, a 3D-printed model of a mouse based on real CT and cryosection data [120] (named Digimouse) is available to study more complex geometries. Bone structures as well as several organs have been printed hollow. The bone cavities have been filled with gypsum after printing to obtain a realistic attenuation behavior for tissue and bones. The cavities of the organs can be filled with agarose gel in which possible XFI marker elements are diluted. Thus, this model allows to perform accurate preliminary studies on sensitivity limits for various possible applications of XFI in preclinical studies. The model was provided by Marie Wegner (Department of Radiotherapy and Radio-Oncology, University Medical Center Hamburg - Eppendorf, Germany) [121] and is shown in figure 3.9. Since the segmented organ data are available as a voxel model as well as the 3D-printed representation, this model can be used in both, simulations and experiments.

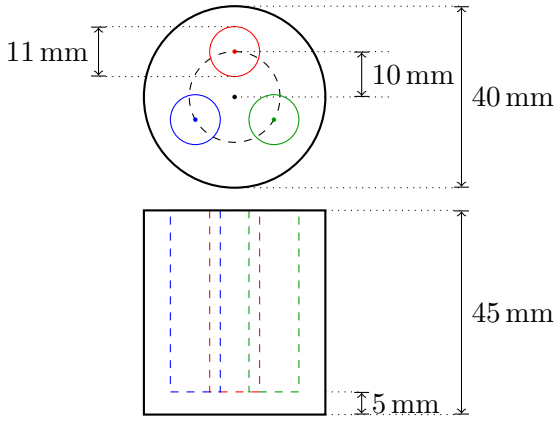

Figure 3.8 – Cylindrical standard phantom dimensions. Adopted from [59].

Figure 3.9 – Photo of the mouse phantom.

3.3 Quantitative X-Ray Fluorescence Imaging

3.3.1 Fluorescence Marker Mass Determination

Being able to quantitatively reconstruct the fluorescence marker mass distribution is an important requirement for the use of XFI for preclinical imaging.

Following the definition of the interaction cross section, the number of expected emitted fluorescence photons N_F in a homogeneous thin target is given as

$$N_F = N_0 \cdot \sigma_F \cdot \rho \cdot l \tag{3.1}$$

where N_0 is the number of incident photons, σ_F is the fluorescence cross section[†], ρ the density of the fluorescence materials and l the length in the target. As fluorescence is emitted isotropically, a detector with area A_D at distance r_D will be hit by $N_F \cdot A_D / 4\pi r_D^2$

[†]Using the XRF convention, see chapter 2.1.7

fluorescence photons. However, one must account for the probability of photoabsorption inside the detector chip to obtain the number of recorded fluorescence events via

$$N_D = N_0 \cdot \sigma_F \cdot \rho \cdot l \cdot \varepsilon_F \cdot \frac{A_D}{4\pi r_D^2} \tag{3.2}$$

where

$$\varepsilon_F = \exp\left(-\left(\frac{\mu}{\rho}\right)_D^{phot}(E = E_F) \cdot \rho_D \cdot d_D\right) \tag{3.3}$$

describes the detection efficiency of the detector with $\left(\frac{\mu}{\rho}\right)_D^{phot}$ the photoabsorption attenuation coefficient of the detector material at the fluorescence energy, ρ_D the density of the detector material and d_D the detector chip thickness.

Rearranging eq. 3.2 and using $m_F/A_B = \rho_F \cdot l$, one can obtain the fluorescence marker mass m_F in the beam volume A_B via

$$\frac{m_F}{A_B} = \frac{N_D}{N_0 \sigma_F \varepsilon_F} \cdot \frac{4\pi r_D^2}{A_D}\,. \tag{3.4}$$

However, this requires precise knowledge about the number of incident photons (which is discussed in chapter 3.5) as well as reliable extraction of the fluorescence counts from the recorded spectrum.

3.3.2 Extraction of the Fluorescence Signal

To extract the fluorescence counts, a fitting routine based on tabulated cross sections is used. For each element i which is included in the fit, the fluorescence signal shape in the fitted energy range is built as a sum of Gaussians centered at the corresponding fluorescence energy of each transition line $E_F^{i,j}$ with a width defined by the detector's energy resolution $\delta(E)$. The Gaussians are weighted by the product of the cross section of the transition and the detector efficiency ε for its energy. Therefore, for each element,

only one single fit parameter for the overall scaling of the element's fluorescence spectrum c_F^i is used. Additionally, a background function $f_B(E, \vec{c_B})$ is added. Typically, either a third-order polynomial or an exponential function is used, depending on the shape of the background. If the low energy tail of the Compton region is part of the fit range, an exponential background often yields better results while a third-order polynomial is used for energy ranges between the Compton-electrons and the Compton region. The model is defined as

$$f(E, \vec{c_E}, \vec{c_B}) = f_B(E, \vec{c_B}) + \sum_{i=1}^{n_E} c_F^i \cdot \sum_{j=1}^{n_L^i} \frac{\sigma_F^{i,j} \cdot \varepsilon_F^{i,j}}{\sqrt{2\pi\delta(E_F^{i,j})^2}} \exp\left(-\frac{\left(E - E_F^{i,j}\right)^2}{2\delta(E_F^{i,j})^2}\right) \tag{3.5}$$

where n_E corresponds to the number of elements and n_L^i the number of transition lines of the i-th element in the fit region and $\{\vec{c_F}, \vec{c_B}\}$ are the free parameters of the fit routine. The number of fluorescence counts per element is given as the integral over the element's signal shape. By using normalized Gaussians in eq. 3.5 and assuming that the energy range of the fit includes several widths of each peak, i.e. an interval of at least $3 \cdot \delta(E_F^{i,j})$ left and right of each peak is included in the fit range, more than 99.7% of the Gaussian is covered by the integral of the element's spectrum in this region and it can be simplified with good approximation to

$$\frac{N_D^i}{\varepsilon_F^i} = c_F^i \cdot \sum_{j=1}^{n_L^i} \sigma_F^{i,j} \tag{3.6}$$

which can be used in eq. 3.4 to calculate the mass of the fluorescence marker in the beam volume. Here, it is assumed that the detection efficiencies $\varepsilon_F^{i,j}$ for the different lines per element are identical and can be expressed as one efficiency per element ε_F^i. As the fluorescence energies of different subshells for the marker materials discussed in this thesis are well within 1 keV, this is a reasonable approximation. When differences in the efficiency become non-negligible, a mean efficiency weighted with the relative cross sections of each fluorescence line has to be calculated instead.

This method relies on the use of tabulated cross section values, which are obtained

using the `CS_FluorLine_Kissel` function of the xraylib [54, 122] library. Detection efficiencies are calculated via the photoabsorption cross section of the detector material using `CS_Photo` of the xraylib. As a fitting routine, `scipy.optimize.curve_fit` of the scipy package is used [123].

3.3.3 Signal Significance

To quantify how significant an extracted signal is, a single-sided hypothesis test can be performed. This test provides the probability that the detected signal has in fact been generated by fluctuations in the background processes and not due to fluorescence. This probability is called the p-value and - when assuming Poisson statistics for the involved processes - can be calculated via

$$p = \sum_{n \geq N_S + N_B}^{\infty} \frac{(N_B)^n}{n!} e^{-N_B} \tag{3.7}$$

with N_S and N_B being the number of extracted signal and background counts in the signal region. A p-value of 0.005 corresponds to a 95.5% confidence that the detected signal has been generated by fluorescence. However, as the p-value becomes very small quickly, an alternative representation of the confidence can be used, namely the significance Z, which is defined as the integral of the normal distribution up to $1 - p$

$$Z(p) = \int_{-\infty}^{1-p} \frac{1}{\sqrt{2\pi}} e^{-\frac{x^2}{2}} \, \mathrm{d}x \, . \tag{3.8}$$

For high values of N_S and N_B, their Poisson distribution can be accurately approximated with a Gaussian distribution [124], and Z can be expressed via

$$Z = \frac{N_S}{\sqrt{N_B}} \tag{3.9}$$

which can be computed easily and corresponds to the signal-to-noise ratio (SNR) of the integrated spectrum [125, 126]. The significance Z can be interpreted as the distance

between the obtained and the expectation value in units of standard deviations in a Gaussian distributed process for the expectation that no fluorescence is present [46, 124]. Typically, a value of $Z \geq 3$ can be used as a lower limit [46, 125], leaving a probability of 0.135% for a false-positive.

3.4 Effects of Attenuation on the Reconstructed Masses

The mass calculation for 2D scans as introduced in section 3.3 assumes that the fluorescence was emitted at the origin of the reference frame, i.e. where the detector is pointing at, and that neither the incident beam nor the fluorescence radiation was attenuated. However, due to the extended size of the mouse, both assumptions are invalid and a correction factor is needed. This correction depends on the depth at which the fluorescence was emitted as well as the distribution of attenuating material in the line of sight to the detector.

3.4.1 Attenuation Correction for a Single Detector

Depending on where within the target volume the fluorescence was emitted, the distance to the detector r might deviate from the nominal distance r_0 used in the mass determination. As the mass scales with r^{-2}, this requires a contribution to the correction factor of

$$c_R(z) = \frac{r(z)^2}{r_0^2}\,. \tag{3.10}$$

The incident attenuation correction follows the Lambert-Beer-Law and can be calculated via

$$c_I(x,y,z) = \exp\left(\int_{z_0}^{z} -\mu_0(x,y,z')\,\mathrm{d}z'\right) \tag{3.11}$$

and the fluorescence attenuation using

$$c_F(x,y,z) = \exp\left(\int_{(x,y,z)}^{\vec{x}_D} -\mu_F(\vec{x}')\,\mathrm{d}\vec{x}'\right) \tag{3.12}$$

where $\mu_0(x,y,z)$ is the position-dependent attenuation coefficient at the incident energy and μ_F at fluorescence energy, and $\vec{x}_D$ is the detector position. Therefore, the total correction factor is given as

$$c = c_R \cdot c_I \cdot c_F \tag{3.13}$$

$$= \frac{r(z)^2}{r_0^2} \cdot \exp\left(\int_{z_0}^{z} -\mu_0(x,y,z')\,\mathrm{d}z'\right) \cdot \exp\left(\int_{(x,y,z)}^{\vec{x}_D} -\mu_F(\vec{x}')\,\mathrm{d}\vec{x}'\right). \tag{3.14}$$

This correction factor cannot be calculated for 2D measurements, as no information on the depth of fluorescence emission or the 3D distribution of attenuation is available.

However, to obtain an estimate of these effects, a 3D voxel model can be used for those calculations. For this, the Digimouse voxel model [120] is used, which was also the basis for the mouse standard phantom (see chapter 3.2.5). Similar to the experimental setup, the detector is placed at a distance of 70 mm and an angle of 150°. For each voxel (i,j,k) the model is placed such that $x_i = y_j = 0$ while the z position is independent of the voxel such that the center of the model is at $z = 0$. This corresponds to the 2D scanning method where the target is moved through the fixed incident beam along the x and y direction, as it is the case for synchrotron experiments. Using this setup, the lengths in the different voxels for both the incident and detector directions are traced and the total attenuation contributions are calculated. Further, the distance correction is calculated for each voxel depth k. Figure 3.10 shows the correction factors for a single slice in the x-z plane in the center of the mouse. At the detector-facing side, a correction factor < 1 is present as the shorter distance outweighs the attenuation effects. When going deeper into the tissue, the attenuation and distance correction increases, resulting in larger correction

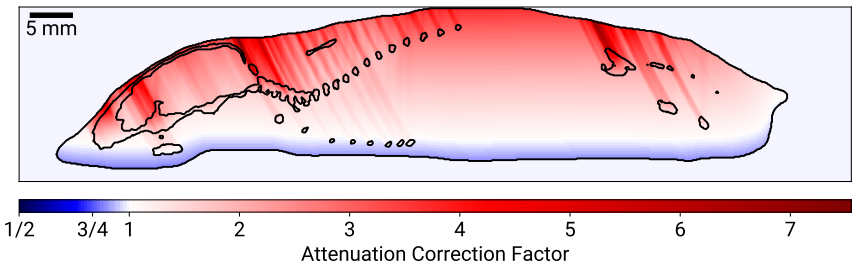

Figure 3.10 – Top view of a y-slice of the attenuation correction of iodine fluorescence. The beam direction is from bottom to top and the detector was placed at 150° scattering angle at 70 mm distance. The contours show the skin and bone locations. Colorbar is chosen such that $1/x$ and x are equidistant to 1.

factors. The diagonal lines show the increased attenuation of the fluorescence signal when bone material is present in the line of sight between the detector and voxel. The largest correction factors are needed in the head region where a thick layer of bones attenuates both incident and signal photons. However, as one cannot infer the depth of origin for measured fluorescence in 2D scans, correction estimates have to be done solely based on the x-y position. Figure 3.11a shows the minimum, average and maximum correction factors along the depth of the mouse for each beam position. As shown in figure 3.10, the maximum attenuation occurs typically in or behind the thickest bone layers, e.g. the head or spine. But in the case of x-ray fluorescence, markers accumulate typically in organs, which are in front of those bones in the simulated geometry. Figure 3.11b limits the projection to only use voxels of organs, giving a much more realistic estimate for the application of XFI. Furthermore, figure 3.12 displays individual correction factors for each organ, with typical values between 1.5 and 2.5 for iodine and a wider distribution for palladium. The biggest spread is present for bones, brain organs, and tissue, which are usually not organs of interest in XFI studies. Palladium is more susceptible to variations than iodine, as its fluorescence energy is only at about 21 keV and thus is attenuated stronger.

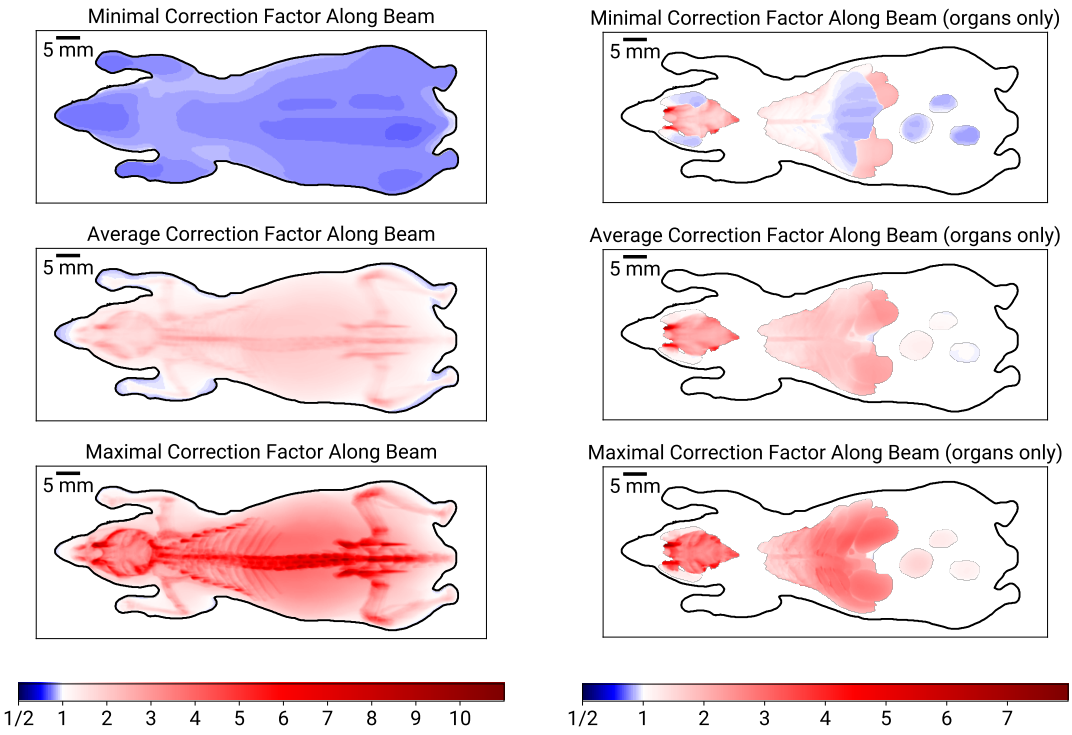

(a) Projections using full mouse

(b) Projections using organs only

Figure 3.11 – Projected minimum, average and maximum correction factor for each beam position for a detector placed at 150° angle and 70 mm distance and iodine fluorescence.

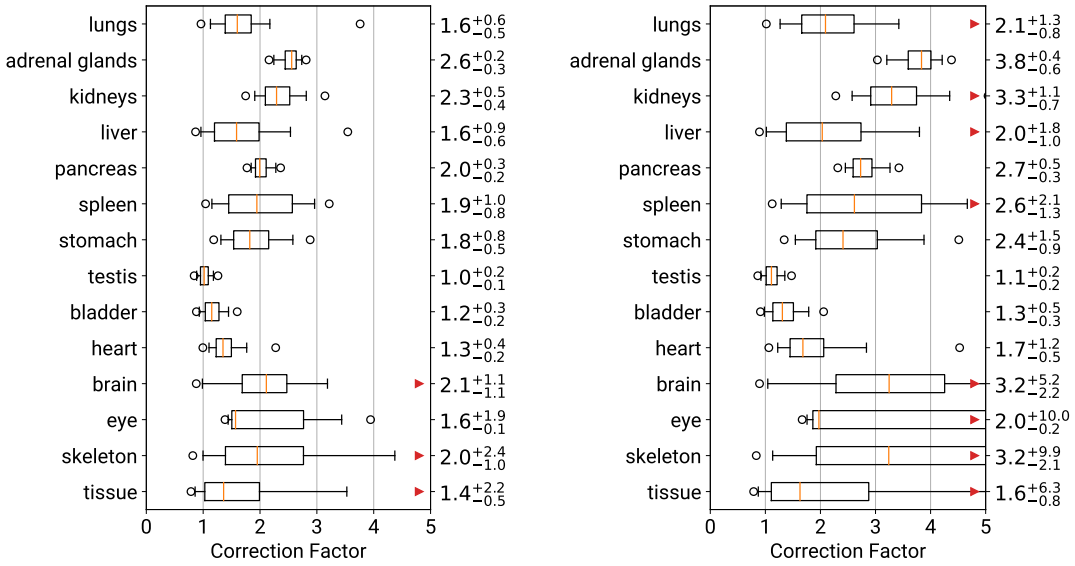

(a) Iodine correction factors

(b) Palladium correction factors

Figure 3.12 – Boxplot for the correction factors separated by the different organs for a detector placed at 150° angle and 70 mm distance for iodine and palladium fluorescence. Orange lines indicate the median value, rectangles the upper to lower quartile, and the whiskers 5 and 95 percentiles. Circles mark to most distant outliers. Red triangles indicate that the outlier is outside the visible range.

Overall, it can be seen that attenuation has to be accounted for to obtain reliable mass reconstructions. Especially the fluorescence photons are attenuated significantly. For 2D imaging, no accurate correction can be performed, however, an estimate for correction factors for individual organs can be calculated.

3.4.2 Attenuation Correction for Multiple Detectors

One of the methods to improve the sensitivity of XFI is the use of multiple detectors and performing the analysis on the combined spectra. In this case, the total covered solid angle of all detectors has to be used in the mass reconstruction (see eq. 3.4).

Since the analysis is performed on the combined data, also a combined correction factor $\tilde{c}$ has to be calculated which can be derived from the individual correction factors c_i for each detector. The expectation value for the number of detected fluorescence photons per detector is given as

$$N_i = \frac{1}{c_i}\sigma_F \varepsilon_F \frac{m_F}{A_B}\frac{\Omega_i}{4\pi} \qquad \forall\, i \in [1, n_D] \tag{3.15}$$

and for the combined data given as

$$\sum N_i = \frac{1}{\tilde{c}}\sigma_F \varepsilon_F \frac{m_F}{A_B}\frac{\sum \Omega_i}{4\pi}\,. \tag{3.16}$$

Summing eq. 3.15 over all detectors and comparing it with eq. 3.16 leads to

$$\sum \frac{\Omega_i}{c_i} = \frac{\sum \Omega_i}{\tilde{c}} \tag{3.17}$$

and therefore

$$\tilde{c} = \frac{\sum \Omega_i}{\sum \frac{\Omega_i}{c_i}} \tag{3.18}$$

for the special case that all detectors cover the same solid angle - e.g. by having multiple detectors of the same type at the same distance but different scattering angles - this can

be simplified to

$$\tilde{c} = \frac{n_d}{\sum \frac{1}{c_i}} \,. \tag{3.19}$$

An important use case for this is to use two detectors, one in forward and one in backward direction to reduce the variance of the correction factors along the beam path. While this does not impact the incident attenuation, it does reduce the variation in fluorescence attenuation, which as seen in figure 3.10 is the dominating factor. An example for iodine fluorescence using detectors at 30° and 150° is shown in figure 3.13. In this case, the median correction factors for all organs are between 1.3 and 1.9. Thus, a uniform correction factor of about 1.6 will lead to a good approximation and can easily be applied to 2D scan data without segmenting different organs.

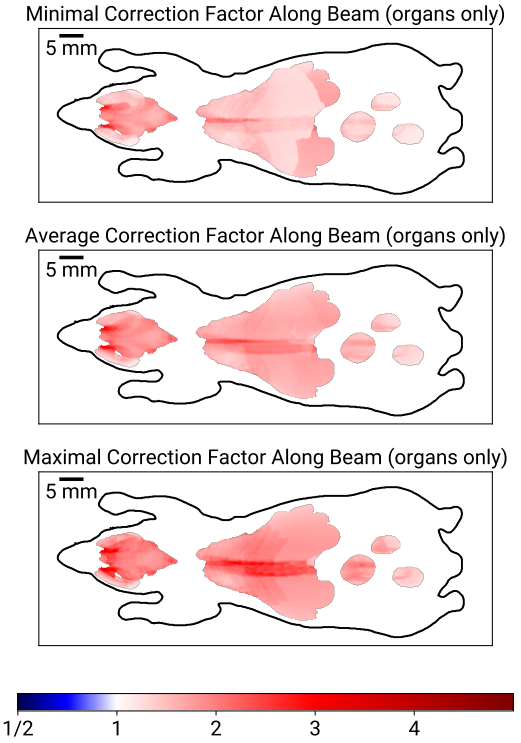

(a) Projection of organ voxels

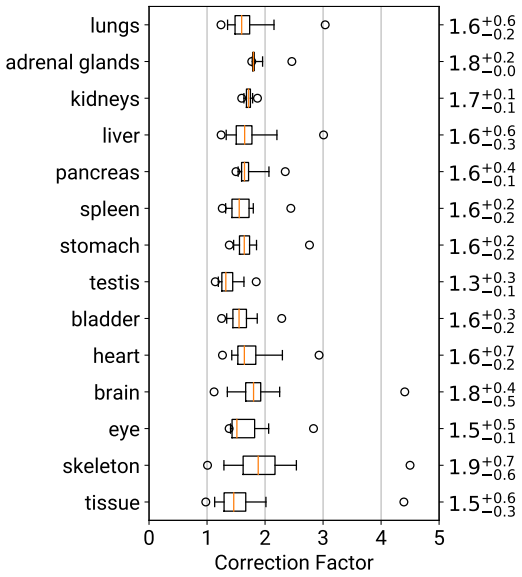

(b) Organ correction factors

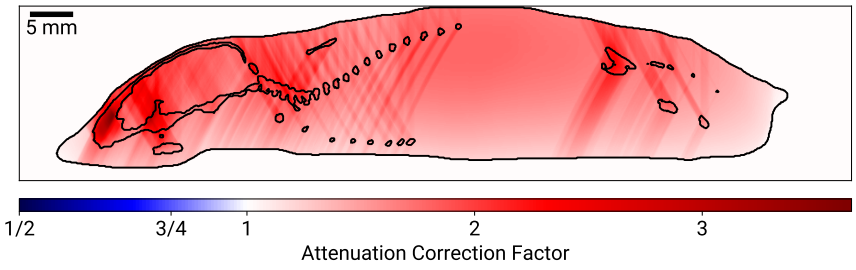

(c) Slice top view

Figure 3.13 – Combined correction factor maps for iodine using two equal detectors at 70 mm distance at scattering angles of 30° and 150°.

3.5 Beamline Incident Flux Measurement

The P21.1 beamline, which was described in detail in chapter 3.2.1, does not provide a way to monitor the absolute photon flux of the incident beam as it is not required for the experiments in the focus of the beamline. However, the PIN diodes do provide a current which is proportional but uncalibrated to the incident flux. For being able to reconstruct masses from fluorescence signals, precise knowledge about the number of photons per measurement is needed. One option to achieve this is to calculate how many photons are needed to induce the measured current based on the average deposited energy and material properties [127]. However, this requires very detailed knowledge about the diode, including the thickness of the intrinsic layer of the diode and parameters such as thickness and material of any cover layers. Further, it has to be verified that the diode does not inhibit high charge carrier recombination, which has been observed in [127] for one individual batch of diodes. Moreover, the diode has to be carefully aligned perpendicular to the beam. Lastly, measuring such low currents can introduce some pitfalls for measurements, such as correcting for the impedance of the diode itself. While all of these issues can be circumvented as shown in [127], it requires extensive calibration measurements of the diodes which is not feasible to do as a beamline user.

Another option often employed is the use of scintillators or other single photon counting detectors to directly measure the count rate of the incident beam [127]. Due to the high flux at synchrotron beamlines, it is not possible to do this with the unattenuated beam as readout electronics typically are limited to $\approx 1 \times 10^6$ counts/s. Thus, the beam has to be attenuated by around 4 orders of magnitude for this method. This requires very accurately machined absorbers and pure materials, as attenuation increases exponentially with absorber thickness. Additionally, contributions such as Rayleigh scattering have to be well understood. In practice, it is not possible to keep the uncertainty within the few percent level at such high attenuation.

Therefore, an alternative way is needed to obtain a calibration from diode current to photon flux which can easily be performed as a user, does not require a complex experimental setup or long measurement times, and can be applied to the unattenuated incident beam. As the experimental setup is already designed to be used for fluorescence measurements, it makes sense to also use fluorescence for the flux calibration. Instead of calculating the mass in the beam as during XFI measurements, a reference target with known mass per area can be used to calculate the number of incident photons.

Several reference targets were purchased from Micromatter (Surrey, BC, Canada). A complete list is shown in table 3.1. The material is vacuum-deposited onto either polycarbonate aerosol membranes or polyester film backings, both having approximately $1\,\mathrm{mg\,cm^{-2}}$ areal mass density. Due to the small thickness of both the backing and the deposited layer, attenuation of the fluorescence signal inside the target can be neglected and Compton scattering is minimal.

For flux measurements, the target is mounted in a 45° orientation and the detector is positioned at 90°. Based on eq. 3.2, the expected number of detected fluorescence photons is then given as

$$N_D = N_0 \sigma_F \rho_F \varepsilon_F \cdot \sqrt{2}\, d \cdot \frac{\Omega_D}{4\pi} \tag{3.20}$$

$$= \sqrt{2} N_0 \sigma_F \varepsilon_F \cdot \frac{m_F}{A_B} \cdot \frac{A_D}{4\pi r_D^2} \tag{3.21}$$

where the factor $\sqrt{2}$ comes from the 45° orientation of the target to the beam, increasing the length of the beam through the fluorescence layer. Rearranging this equation leads to

$$N_0 = \frac{N_D A_B}{\sqrt{2}\varepsilon_F \sigma_F m_F} \frac{4\pi r_D^2}{A_D}\,. \tag{3.22}$$

As can be seen in eq. 3.22, it is important to have good knowledge about the distance of the detector as the reconstructed flux scales quadratically with the distance. However,

Table 3.1 – Overview of available XRF reference targets. Samples XRF51715 and XRF51716 were deposited with RbI ($\rho = 3.11\,\mathrm{g/cm^3}$) and therefore contain two usable fluorescence elements. Thicknesses are certified for ±5% by the manufacturer.

Target ID	Fluorescence Element	Element Density ρ_F [$\mathrm{g\,cm^{-3}}$]	Thickness d [nm]	Mass/Area m_F/A [$\mathrm{\mu g\,cm^{-2}}$]
XRF51715	Rb	1.25	65.2	8.2
	I	1.85	65.2	12.0
XRF51716	Rb	1.25	158	19.8
	I	1.85	158	29.2
XRF51717	Ag	10.5	17.1	17.9
XRF51718			50.3	52.6
XRF51719	Au	19.3	11.1	21.5
XRF51720			27.4	21.5
XRF53949	Pd	12.0	13.8	16.6
XRF53950			38.5	46.3

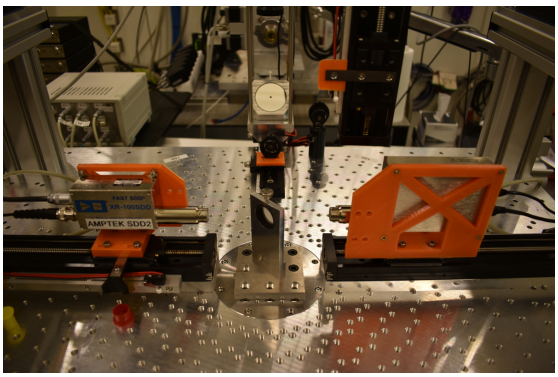

(a) Photograph of the stage setup during reference target measurements.

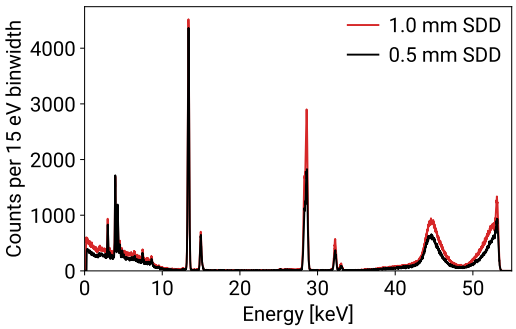

(b) Example spectrum for target XRF51715 (RbI) for a 0.5 mm and 1 mm thick SDD.

Figure 3.14 – Setup of a typical flux reconstruction measurement

in the experimental setup shown in figure 3.14), the detector is often mounted onto a motorized axis with movable limit switches, meaning that its distance is not accurately constrained. Further, direct measurement of the distance is problematic, as the beryllium cover of the detector has to be handled with care. As a result, the offset δr of the measured position $\tilde{r}_D$ compared to its true offset r_D can be in the order of a few millimeters. To obtain this offset, a distance scan can be performed, obtaining spectra at multiple detector offsets from which δr can be reconstructed by fitting

$$f(\tilde{r}_D) = \frac{a}{(\tilde{r}_D + \delta r)^2} \tag{3.23}$$

to the number of fluorescence counts.

Measuring this offset is not only needed for the flux reconstruction, but also for later XFI measurements. Therefore, those distance scans were performed at the beginning of each beamtime.

An example for the different steps in the incident flux calculation is shown in figure 3.15. Recorded spectra are normalized to a fixed diode current and fluorescence counts

are extracted via fitting (figure 3.15a). The detector position offset from the nominal position (i.e. the assumed motor position) is determined using eq. 3.23 (figure 3.15c). For each measurement, the incident flux is then calculated via eq. 3.22 (figure 3.15b). In the case of a correctly determined offset value, a constant result is expected. At last, the individual results are combined to obtain the final measurement result for the incident flux and a conversion factor from induced current to photon flux for the PIN diodes, which can be used to monitor the absolute flux during the beamtime (figure 3.15e). Flux values can typically be determined with $\approx 5\%$ standard deviation, matching the fabrication tolerance of the standard targets.

Between different beamtimes at the P21.1 beamline, large variations of the incident flux have been observed, changing between 3×10^{10} photons/s/mm^2 and 1.7×10^{11} photons/s/mm^2, depending on the tuning of the monochromator and improvements at the beamline during the course of this thesis.

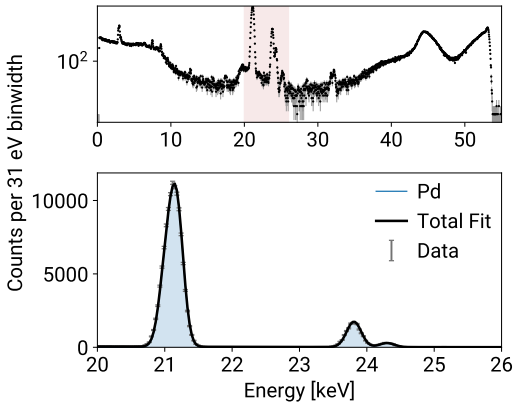

(a) Typical fit of the fluorescence signal.

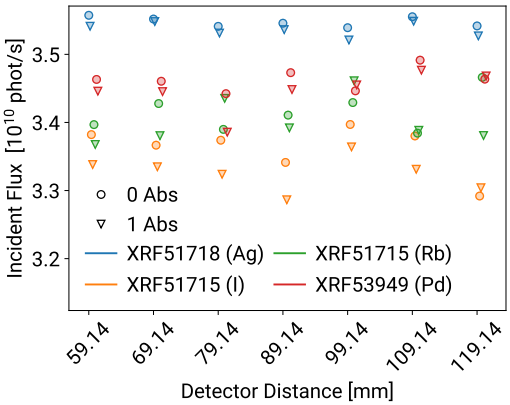

(b) Reconstructed incidence flux for each measurement.

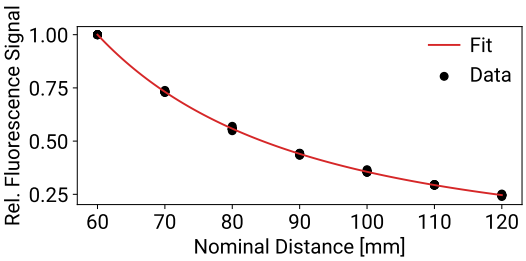

(c) Detector distance offset fit.

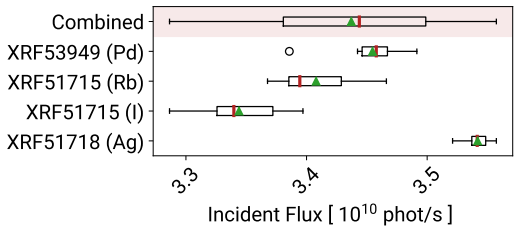

(d) Combined resulting incident flux.

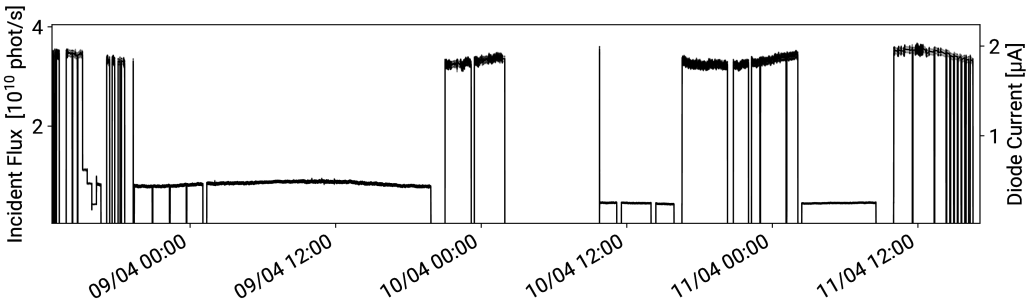

(e) Calibrated beamtime incidence flux timeline.

Figure 3.15 – Example of the flux reconstruction results for one beamtime. Sharp steps in (e) are the results of changes to the number of absorbers or the variation of the beam size.

4 Quantitative Small Animal 2D XFI Measurements

Inflammatory bowel disease (IBD) including Crohn's disease and ulcerative colitis are chronic inflammatory diseases and associated with an increased risk for colon cancer [128]. The exact mechanisms leading to the inflammation are unclear yet but are assumed to be connected to a combination of environmental factors and genetic susceptibilities, resulting in an uncontrolled immune response. Single-cell analysis indicates a broad range of involved immune cells, including various T-cells and macrophages [129]. Thus, simultaneous in-vivo tracking of these cells would bring great benefit to understanding the mechanisms triggering this uncontrolled immune response but is currently not possible [19].

XFI might be a suitable imaging modality, but requires advances in both, detection sensitivity and labeling efficiency of immune cells with possible markers. Two promising candidates for such markers are iodine in the form of iohexol - a contrast agent often used in clinical CT or angiography - or palladium-nanoparticles (PdNPs). Both are already in use in different medical applications [130–133] and emit K-shell fluorescence in the range between 20 and 30 keV (I: 28.6 keV, Pd: 21.1 keV), therefore having high enough transmission through soft tissue and being below the Compton scattering region for 53 keV incident energy.

In this chapter, different pilot studies for the application of XFI to preclinical applications such as IBD are discussed, with the long-term goal of tracking multiple kinds of immune

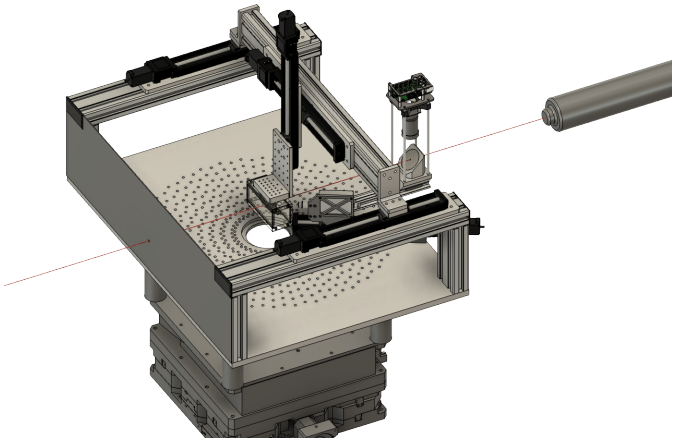

Figure 4.1 – Setup of the experimental stage for the in-situ mouse experiments. A single SDD is placed at 150° scattering angle.

cells simultaneously in-vivo in mice using XFI.

Figure 4.1 shows the platform setup used for the experiments in this chapter. A single SDD with 50 mm^2 collimated detection area and 0.5 mm thickness was placed at 150° scattering angle at 70 mm distance to the center of the platform. The mice are positioned in a sealed PMMA container with 1 mm thick walls, such that the beam enters from the bottom and the spleen is at the top. This results in the shortest possible path of the incident beam and fluorescence photons through tissue for most organs and avoids any large bones which would heavily attenuate the fluorescence signal.

The selected detector placement is a compromise between different parameters to be optimized. While the total count rate, which is dominated by Compton scattering, is minimal at 90°, the minimal distance at this angle is limited by the mouse container. Moving to larger scattering angles allows for a closer distance and therefore larger covered solid angle. Furthermore, attenuation correction as discussed in chapter 3.4 becomes

more asymmetric when the detector is placed at one side of the sample. Additionally, when a second detector becomes available in the future, a two detector system at 30° and 150° allows to obtain a nearly constant attenuation correction factor, as shown in figure 3.13.

9-13 weeks old C57BL/6 Rag1$^{-/-}$ mice were used for the pilot studies. All mice were cared for in accordance with German animal ethics regulations and experimental protocols were approved by the institutional review board 'Behörde Justiz und Verbraucherschutz', Hamburg, Germany (number ORG 998 and N 024 20).

4.1 Thyroid Scans

The thyroid plays an important role in regulating metabolism and energy consumption. For the creation of the thyroid hormone (Levothyroxine), iodine-carrying molecules are needed. Thus, for the correct functioning of the thyroid, it extracts and stores iodine from the circulation [134]. Typically, studies involving the thyroid are therefore based on the use of the radioactive iodine nuclides ^{125}I or ^{131}I to observe the dynamics and accumulation inside the thyroid. Depending on the targeted resolution as well as the detection method (SPECT or scintigraphy), typically between 10 and 800 µCi (0.4 to 30 MBq) are used, leading to a local radiation dose between 1 Gy for low-resolution scintigraphy up to 80 Gy for micro-SPECT [135–139]. An alternative approach to this is the use of XFI, allowing to detect the accumulation of endogenous iodine and enabling long-term studies not limited by the half-live time of the radiotracer. The results presented in this chapter have been published in [38]. XFI measurements of the thyroidal iodine were used to demonstrate the feasibility of synchrotron-based XFI for small quantities of fluorescence markers. These measurements can be seen as an intermediate step towards cell tracking

Table 4.1 – List of scan parameters for the individual thyroid scans. Data taken from [38].

Sample	Resolution [mm]	Duration [s]	Photons per Pixel	Local Dose [mGy]	Scan mode
M1	1	1	2.5×10^9	87	stepwise
M1	0.5	10	6.3×10^9	882	stepwise
M2	1	1	2.3×10^9	80	continuous
M2	0.2	1	3.4×10^9	2975	stepwise
M3	1	2	5.4×10^9	168	continuous
M3	0.5	1	1.2×10^9	168	continuous
M3	0.2	5	5.7×10^9	4987	stepwise

and pharmacokinetics, using XFI to image biological accumulations of iodine with concentrations being similar to the levels expected in such labeling studies, but eliminating variabilities due to the cell labeling efficiency or exocytosis. This allows testing of the needed advances in XFI independently of the ones in cell labeling. Since this study was designed with future in-vivo applications in mind, radiation dose was an important factor of concern. Thus, as motivated in chapter 2.1.8, 300 mGy will be used as an upper limit for in-vivo XFI experiments and shall be already demonstrated in these in-situ studies.

The thyroid region of three different mice was scanned across several beamtimes. For each mouse, multiple different scans were performed to test a large variety of parameters. However, at least one high-resolution scan with a high dose and one scan with in-vivo conform dose was performed, where the high-resolution scan serves as reference data. The parameters of each scan are listed in table 4.1.

Iodine masses were calculated from the fluorescence spectra as described in section 3.3. As the thyroid is close to the skin and the mouse was oriented such that the path to the thyroid in the tissue was minimized, attenuation effects can be neglected.

Typical results are shown in figure 4.2. Two different significance thresholds were compared: $Z \geq 3$ which has typically been used for single-point measurements [37, 46, 88] (figure 4.2 d-e) and a relaxed limit $Z \geq 1.6$ (a-c). The rationale behind this lower limit is that in a scan with many pixels it is more tolerable to have some false positives than for a single data point. For the high dose reference scan, the difference between both scans is negligible (c,f) but for the lower dose scans more pixels surpass the lower significance threshold $Z \geq 1.6$ but not $Z \geq 3$ and comparison to the reference image suggests that most - but not all - of these pixels are true signals, not noise.

To obtain the total thyroidal iodine mass, one can either use the sum of the reconstructed masses per pixel or alternatively extract the fluorescence from the sum of the recorded spectra of each pixel. While this process removes any spatial information, the statistics of the sum spectrum are increased. In first order approximation, summing the spectra of n pixels with similar signal levels will improve the significance by $\sqrt{n}$ (see eq. 3.9). The different resulting total masses are shown in figure 4.4. Obtaining the mass via fitting the summed spectrum generally shows good agreement between low- and high-dose scans and for most scans, the pixelwise sum did also yield consistent masses. However, especially for the M3 scan with 0.5 mm resolution (which has the lowest number of incident photons per pixel), strong deviations are visible, indicating that large portions of the thyroid were below the sensitivity limit of the scan.

Using these results, it is possible to define a sensitivity limit for the minimal detectable iodine mass inside the beam volume based on eq. 3.4 and eq. 3.9. Using

$$N_B = R_B N_0 \frac{A_D}{4\pi r_D^2} \tag{4.1}$$

with R_B being the ratio of generated background photons and the total number of incident photons, normalized to the solid angle of the detector, the minimal detectable mass

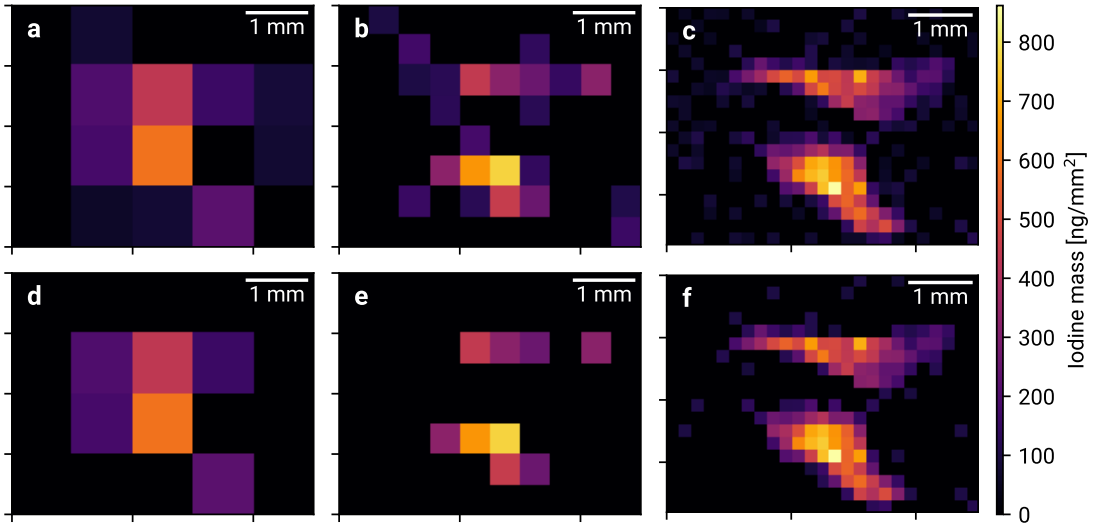

Figure 4.2 – Reconstructed iodine distributions for the different scans of M3 using a significance limit of $Z \geq 1.6$ (a-c) and $Z \geq 3$ (d-f). Taken from [38].

per beam area is given as:

$$\frac{m_{min}}{A_B} = \frac{Z_{min}}{\sigma_F \sqrt{\varepsilon_F}} \sqrt{\frac{R_B}{N_0} 4\pi r_D^2 A_D}\,. \tag{4.2}$$

R_B was determined experimentally to be 6×10^{-4} for this experimental setup and at the maximum in-vivo conform dose of 300 mGy, approximately 8.6×10^9 photons/mm^2 [43] can be used. With $Z_{min} = 3$, this results in a sensitivity limit of 120 ng/mm^2 or 64 ng/mm^2 for $Z_{min} = 1.6$. By using these sensitivity limits, it is possible to estimate the required labeling efficiency and total marker masses for future biodistribution experiments.

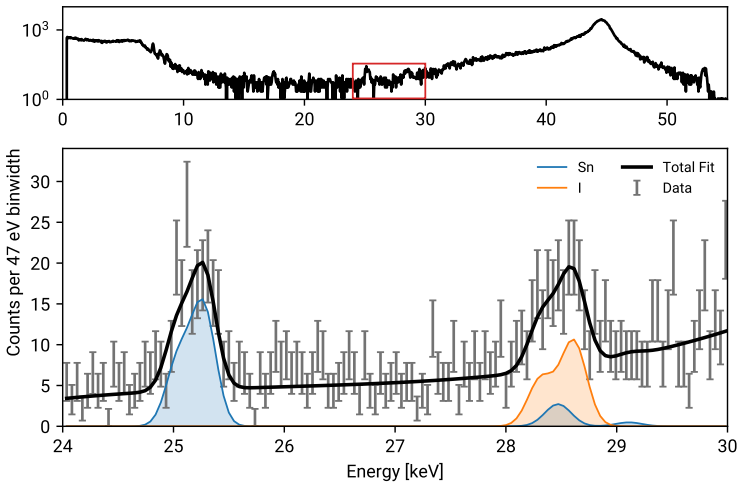

Figure 4.3 – Example spectrum and fit for one high-dose reference spectrum. Taken from [38].

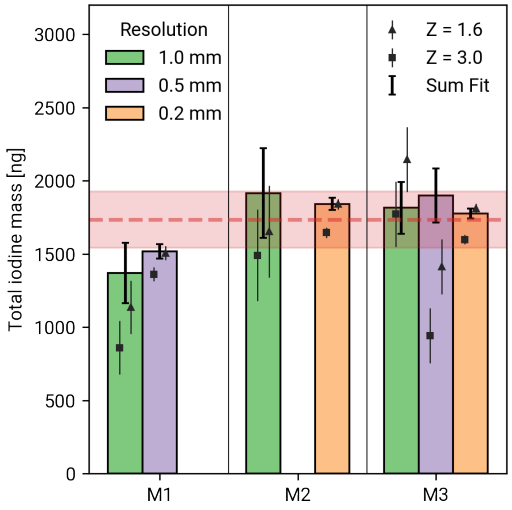

Figure 4.4 – Comparison of reconstructed total thyroidal iodine masses for each scan and different reconstruction methods. Red bar indicates the mean and standard deviation. Taken from [38].

4.2 Biodistributions of Injected Iohexol and PdNPs

Before performing cell tracking studies, biodistributions of the free markers 24 hours after injection were measured to obtain a reference distribution.

As iodine marker, 10 mg iohexol (corresponding to 4.6 mg iodine) diluted in 100 µL PBS was injected intraperitoneally (i.p.) and the mouse was sacrificed and scanned 24 hours after injection. For the palladium measurement, 100 µg PdNPs (5 nm diameter) coated with PMA were injected. Details on the synthesis can be found in [89].

The experimental setup was identical to the thyroid measurements in section 4.1 and spectra were obtained using 5×10^9 photons/mm^2, corresponding to 170 mGy. Transmission images were obtained using the x-ray eye. For fluorescence reconstruction, a minimum significance of $Z \geq 3$ was used.

Full-body composite fluorescence/transmission images are shown in figure 4.5. Iodine is predominantly accumulated in the bladder and intestine while palladium is accumulated in the liver. However, the spleen is indistinguishable from the liver in the chosen scan orientation. Furthermore, the endogenous iodine in the thyroid is visible. In total, 249 µg iodine, corresponding to 2.49% of the injected dose (%ID), and 54 µg palladium (54% ID) were reconstructed. As discussed in chapter 3.4, reconstructed fluorescence masses are influenced by attenuation of the incident and more importantly fluorescence photons. Without 3D distribution information, only estimates about this correction can be made. Based on figure 3.12, the correction factor for iodine in the bladder is about 1.2, but no correction factor for the intestine is available, as it is not segmented in the Digimouse voxel model. For palladium in the liver, the correction factor is about 2 but due to the large extent of the liver has a large variation. Therefore, the attenuation-corrected reconstructed percentage of the injected dose can be estimated to be 3-5% for iohexol and >80% for PdNPs including a large tolerance on the liver correction factor.

Combining both the location of the accumulation and the %ID suggests that the free iodine is rapidly cleared from the circulation system, while the PdNPs are not filtered as strongly. This behavior has also been found previously and is one of the reasons for using free iodine-based molecules as contrast agents in CT imaging [140]. In contrast, nanoparticles have been detected even weeks after injection [40].

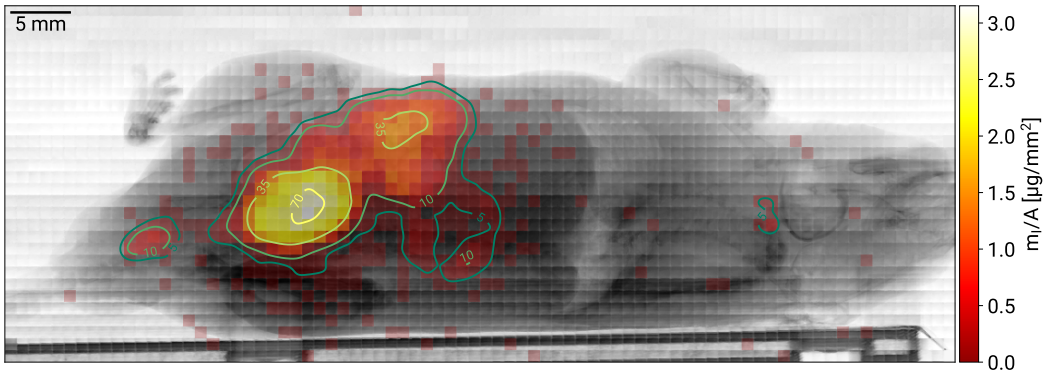

(a) Iodine distribution 24h after injection of 10 mg iohexol.

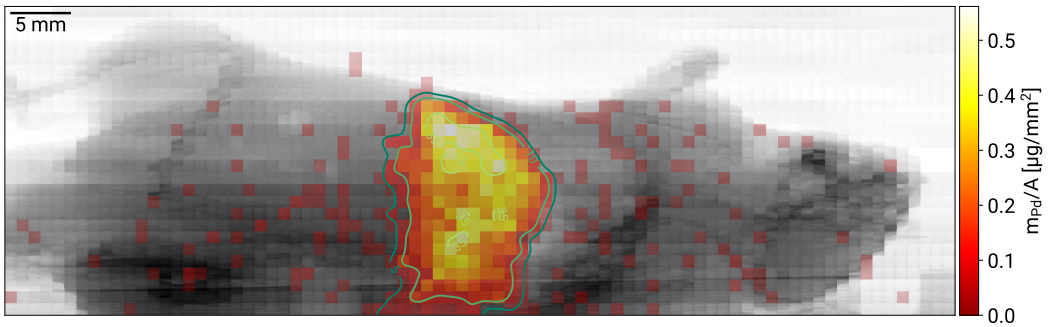

(b) Palladium distribution 24h after injection of 100 µg PdNPs.

Figure 4.5 – Composite fluorescence/transmission images of the marker biodistributions 24 hours after injection. Contours show the significance values for Z =5, 10, 35, and 70. Only pixels with $Z \geq 3$ are marked in the fluorescence image.

4.3 In-situ Biodistributions of Labeled Macrophages

Extensive in-vitro cell labeling studies [89] were performed to optimize the loading of macrophages (MHS) and CTTL-2 cells (ATCC, Manassas, VA, USA) with both iohexol and PdNPs. For MHS, uptakes of about 15 pg/cell for iohexol and 1.2 pg/cell PdNPs were achieved without significantly compromising cell viability and proliferation. For CTTL-2 cells, uptake rates are 5-10 times less than for MHS. While iohexol demonstrated much higher uptake rates, exocytosis is also more prominent, meaning that after 24h less than 10% of the initial iodine mass is still present in the MHS. PdNPs demonstrated a much better long-term stability, with approximately 90% of the palladium still present in the cells after 24 hours.

By demonstrating the ability to detect marker concentrations above 120 ng/mm^2 and the achieved cell uptake, tracking of labeled macrophages was shown to be feasible and shall be demonstrated as the final step before in-vivo experiments can be performed.

For this, a time series of the biodistribution of MHS cells using four mice was recorded. In each mouse 6×10^6 iodine-labeled and 6×10^6 palladium-labeled MHS cells (corresponding to a total of $\approx$ 90 µg iodine and $\approx$ 7.2 µg palladium) were injected intraperitoneally and the mice were sacrificed and scanned 2, 6, 18, and 32 hours after injection using 1.2×10^{10} photons/mm^2, slightly more than the in-vivo conform dose limit. Data are shown in figure 4.6 and 4.7 and total reconstructed masses are listed in table 4.2.

The first time point was chosen such that most cells are still directly at the injection site. Reconstructed masses agree well with the expected masses based on the number of injected cells and cell loading values and are within the batch-to-batch variations of the labeling efficiency [89]. For the 18h and 32h time points, the markers are mostly distributed in the peritoneal cavity. Due to the distribution in a large volume and the low palladium concentration per cell, the palladium fluorescence signal is close to the

Table 4.2 – Reconstructed total marker masses for the labeled MHS.

Timepoint	Iodine [µg]	Palladium [µg]
2h	70.0	8.1
6h	74.4	3.7
18h	30.2	3.4
32h	7.2	3.7

sensitivity limit and masses cannot be reconstructed reliably, thus the total mass is most likely underestimated. As expected from the exocytosis studies, iodine masses are dropping significantly after 6 hours, while palladium is more stable. After 32 hours, both markers are only detectable in the bladder suggesting that both markers were cleared by the cells.

As with the freely injected markers in section 4.2, the reconstructed masses listed above do not account for attenuation corrections and in this case they are hard to quantify. The peritoneal cavity extends between the organs and has therefore a wide variety in depth along the beam, but the injection site is closely behind the skin where almost no attenuation is expected.

In comparison to the marker distributions from section 4.2, a clear difference can be observed. The freely injected markers did accumulate in specific organs (liver for PdNPs, intestine for iohexol), while the markers of the labeled macrophages did mostly stay in the peritoneal cavity. This suggests that in the latter experiment, the biodistribution of these cells was successfully obtained and the marker material was not cleared out of the cell via exocytosis.

In conclusion, with this study it was shown that the experimental setup can be used to

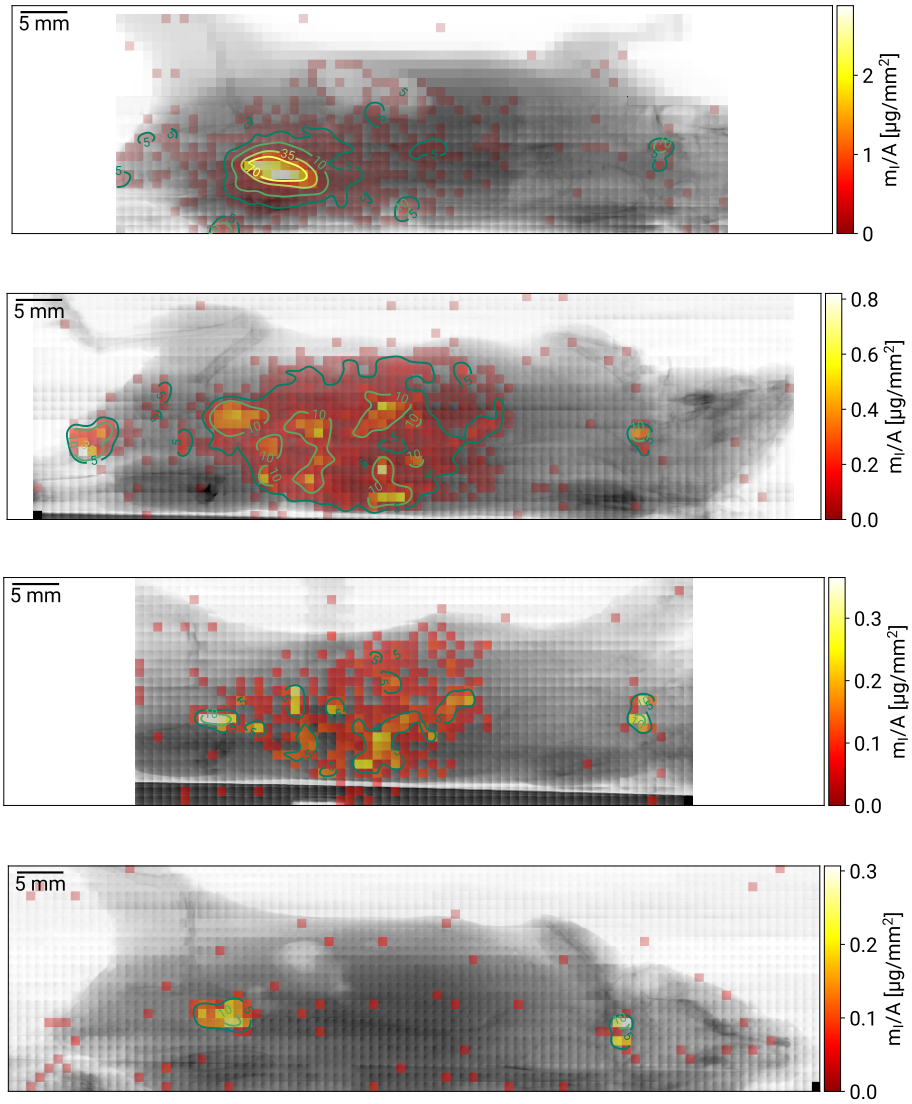

Figure 4.6 – Composite fluorescence/transmission images of the iodine biodistributions 2, 6, 18, and 32 hours (top to bottom) after i.p. injection of labeled macrophages.

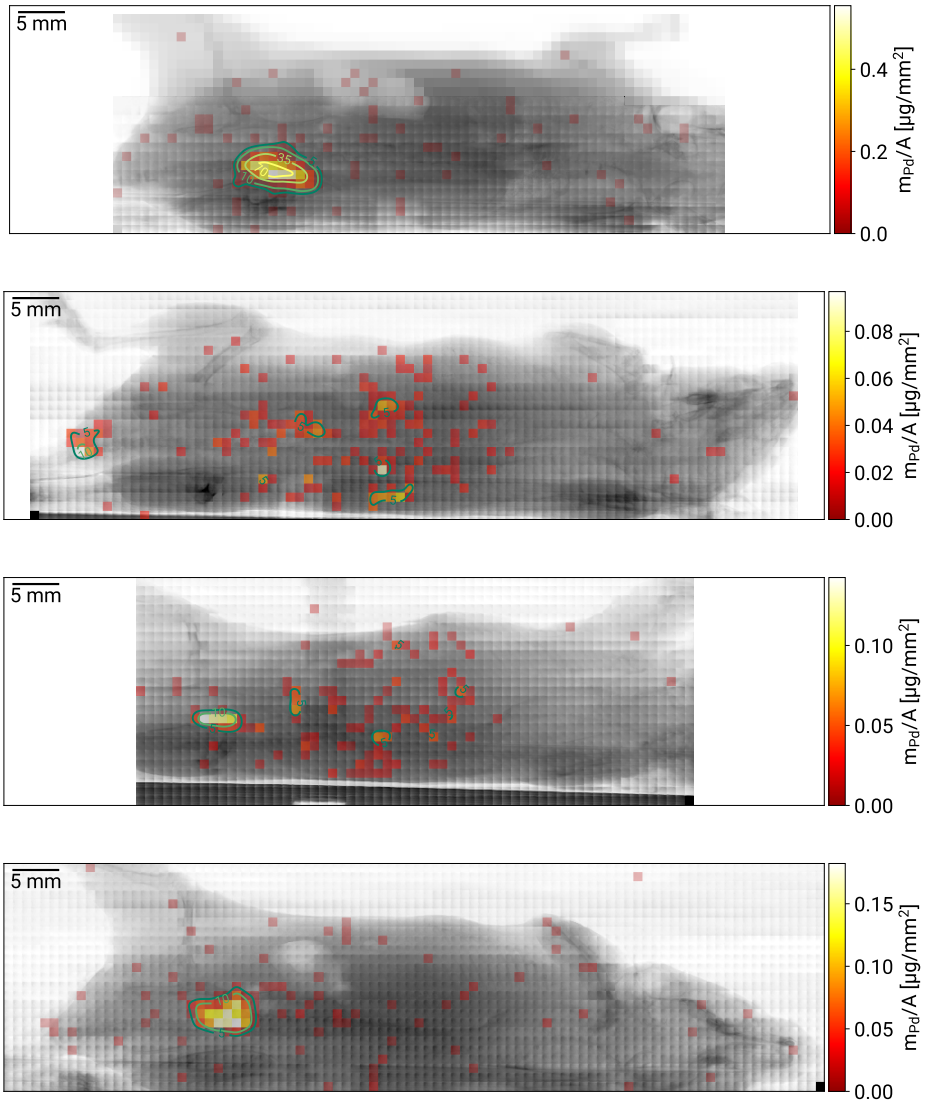

Figure 4.7 – Composite fluorescence/transmission images of the palladium biodistributions 2, 6, 18, and 32 hours (top to bottom) after i.p. injection of labeled macrophages.

track 6×10^6 iodine-labeled macrophages over 32 hours after injection. In contrast, PdNPs could not reliably be tracked at most time points, since only approximately one-tenth of the marker uptake was achieved. With the current experimental setup, these marker concentrations are close to the sensitivity limit. However, the concept of multiplexed cell tracking was demonstrated.

4.4 In-vivo Biodistributions of Macrophages and Free Iohexol

With the results of the in-situ pilot studies, nearly all individual aspects needed for in-vivo cell tracking have been tested and demonstrated. However, animal handling can only be tested up to some extent in in-situ experiments, and measurements at a synchrotron facility do present special challenges for in-vivo handling. Therefore, an important pilot study is the reproduction of the experiments from sections 4.2 and 4.3 in-vivo to demonstrate handling procedures and investigate, whether movements due to breathing and heartbeat introduce visible artifacts. The mice were anesthetized using isoflurane and transferred into a 35 mm diameter imaging cell, supplying a continuous flow of isoflurane and a heated bed to maintain a stable body temperature. Temperature, ECG, and respiration sensors can be used to monitor vital signs. The equipment used for animal handling is a commercially available system manufactured by Minerve (Équipement Vétérinaire MINERVE, Esternay, France) and is placed on a mobile trolley.

As uptake of PdNPs was at the detection limit during the in-situ experiments, only iohexol-labeled macrophages were used and 10^7 cells were injected into two mice. Scanning was performed 6 hours after injection to study the variability of macrophage distributions.

Additionally, 20 mg of free iohexol (corresponding to 9.2 mg iodine) was injected into a third mouse which was scanned at two time points, 6 and 18 hours after injection, demonstrating longitudinal measurement of biodistributions from the same organism. Table 4.3 lists the most important parameters of the scans and the total reconstructed masses (without any attenuation correction) and the composite fluorescence/transmission images are shown in figure 4.8. The free iohexol scan six hours after injection in figure 4.8a suffers from too strong signals, resulting in over-exposure of the fluorescence image. Even at positions outside the mouse, significant amounts of fluorescence signal can be recovered, which are generated by incident photons that scattered at air molecules and thus intersected the mouse. Typically, this effect is small enough to be neglected. While the iodine is widely distributed in the peritoneum, i.e. where it was injected, after two hours, it mostly accumulated in the intestine and bladder after 18 hours and the total reconstructed mass dropped by $\approx 85\%$, showing the fast clearing process of free iohexol molecules by the circulation system.

Assuming that nearly all iodine is still present in the organism after 6 hours and reconstructing approximately 6.6 mg yields an attenuation correction factor of about 1.4 which is in good agreement with the previously calculated ones shown in figure 3.12. Macrophage distributions in figure 4.8c and 4.8d are distinct from the free iohexol distributions and consistent with in-situ data. The macrophages are mostly located in the peritoneum and a small fraction in the colon. No significant variation between the two mice (or the in-situ measurement shown in figure 4.6) is visible and the difference in total reconstructed iodine mass is within 15%.

Small artifacts imposed by the breathing of the mice are visible around the lung in the transmission image, but their size is below the resolution of the fluorescence image and is thus no issue for functional imaging. With these measurements, all required steps for longitudinal multiplexed in-vivo 2D cell tracking using XFI were successfully

Table 4.3 – Parameters of the in-vivo XFI scans. Radiation dose estimate is based on [43]

Scan IDs	Injected Labels	Time after Injection	Photons [photons/mm^2]	Dose [mGy]	Rec. Mass [µg]
A	9.2 mg iohexol	6h	4×10^9	130	6657
B	9.2 mg iohexol	18h	4×10^9	130	893
C	10^7 MHS	6h	6×10^9	190	146
D	10^7 MHS	6h	6×10^9	190	162

demonstrated, although some challenges remain: Quantitative analysis is limited by the uncertainty of precalculated organ correction factors. In the future, their variance might be reduced by using opposing detectors. Furthermore, 2D imaging limits segmentation of the fluorescence signal into different organs, as it is only possible when they do not overlap in the selected projection. Thus, the orientation in which the mouse is imaged has to be optimized for the organs of interest.

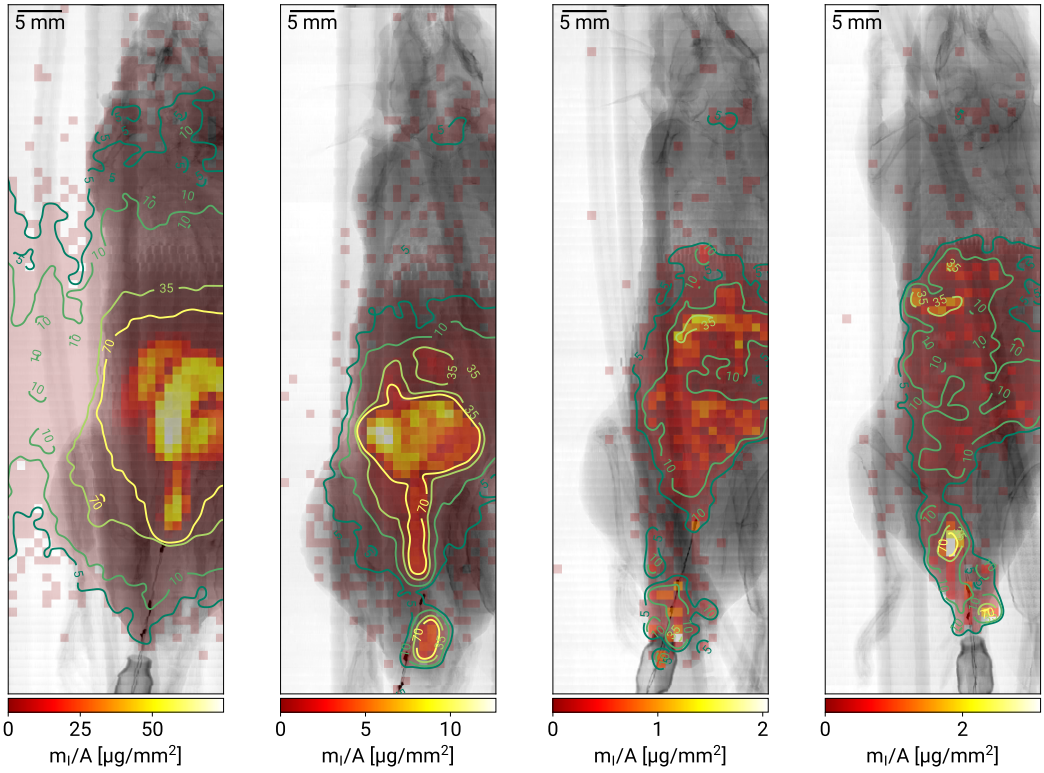

(a) Iohexol after 6h

(b) Iohexol after 18h

(c) Macrophages after 6h

(d) Macrophages after 6h

Figure 4.8 – Composite fluorescence/transmission images of the iodine biodistributions during in-vivo experiments. Subfigure letters correspond to the scan ID in table 4.3

5 X-Ray Fluorescence Tomosynthesis

So far, only 2D fluorescence images have been discussed in this thesis. However, in the context of medical imaging, 3D information is often needed - or at least beneficial - for correct interpretation of the biological processes and limitations of 2D XFI can been seen in the results in chapter 4.

In absorption imaging, Computed Tomography (CT) has proven itself as a reliable method for 3D imaging but an alternative method, Tomosynthesis (TS), has emerged as a viable alternative when low dose is crucial, as discussed in chapter 2.3.

In XFI, the concept of tomography has already been applied to reconstruct the three-dimensional fluorescence marker distribution, which is called x-ray fluorescence computed tomography (XFCT) [40, 42, 91–94]. For XFCT, the object is scanned in the x-y-θ domain and for each measurement, the number of fluorescence photons is extracted from the spectrum, creating fluorescence sinograms. The traditional CT reconstruction algorithms can then be applied to obtain the x-y-z fluorescence distribution. Typically, an iterative reconstruction is needed instead of the filtered back-projection, as it allows including correction terms for fluorescence attenuation. Additionally, the resolution in XFCT is usually much lower than in regular CT and in the order of mm, meaning that it is difficult to include frequency filtering.

However, the requirement to reliably extract the fluorescence signal for each measurement requires a large dose increase for XFCT compared to 2D XFI scans as the number of projections increases but the number of incident photons per measurement has to

stay approximately constant[†]. Instead, a reconstruction method is needed, for which the product of incident photons per beam and number of projections can be kept constant without significantly reducing the overall sensitivity. To solve this problem, a reconstruction method was developed which is not working directly on the recorded spectra but on linear combinations of the individual measurements. Since this is a similar approach to the shift-and-add method of tomosynthesis presented in chapter 2.3.2, this method will be called x-ray fluorescence tomosynthesis (XFTS) in the following.

5.0.1 XFTS Algorithm

Just as for an XFCT scan, the sample is scanned along one translational axis for many different projection angles n_p to obtain the sinogram of individual spectra. The imaging process can be described as a linear transformation

$$b = T \cdot x \tag{5.1}$$

which maps the pixelated marker distribution $x \in \mathbb{R}^N$ to the dataset $b \in \mathbb{R}^M$ via the transformation matrix $T \in \mathbb{R}^{MxN}$, where N is the number of pixels in the reconstruction space and M the number of values of the dataset used for reconstructing the slice. The coefficients of T are defined by the experimental setup, e.g. detector position, detection efficiency, interaction cross section as well as the attenuation due to the target geometry. In the traditional XFCT, M is equal to the number of L independent measurements obtained and the term dataset refers to the extracted fluorescence counts per measurement. In XFTS, for each pixel in the reconstruction space, a linear combination of the L obtained individual measurements is used to generate a unique spectrum from which the fluorescence signal for the reconstruction is extracted, resulting in $M = N$ values in the

[†] Z_{min} might be reduced a bit compared to 2D scans, similar to what was done for the thyroid scans in chapter 4.1, meaning that the number of photons needed per projection might be a bit smaller than in 2D imaging.

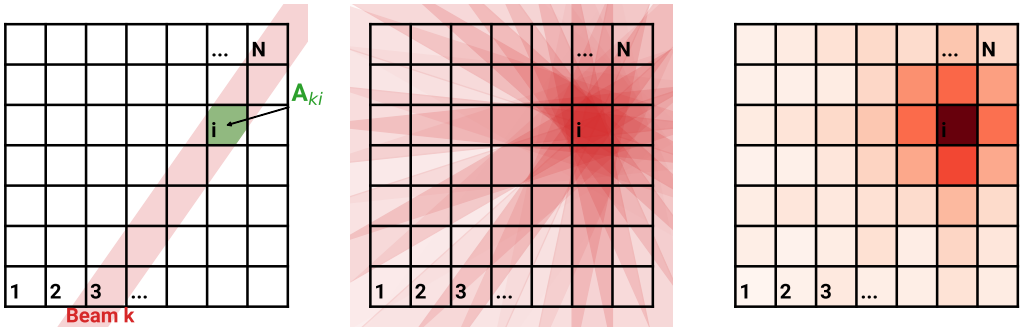

Figure 5.1 – Schematic working principle of the synthesis step in the XFTS algorithm. Left: Definition of important quantities for a single pixel i and beam k. Center: All beams for which the weighting matrix $Q_{ik} = Q_{jk}$ is non-zero. Spectra of these measurements will be summed based on the weights A_{ki} to obtain the synthesized dataset b_j. The transparency of each beam corresponds to the weighting Q_{jk} due to the covered area. Right: Relative strength of each pixel contributing to the dataset b_j representing the entries in the j-th row of the imaging transfer matrix T. It corresponds to a blurred image of the original pixel i.

dataset. In the following, whenever possible the index i is used for indexing the pixelated reconstruction and real space R^N and j is used to index data in the vector space R^M. k is used to index the measurements R^L.

Based on the true distribution of the fluorescence marker x, the expected number of fluorescence counts in each individual measurement $s \in \mathbb{R}^L$ is given as

$$s_k = \sum_{i=1}^{N} W_{ki} x_i \qquad 1 \leq k \leq L \tag{5.2}$$

where $W \in \mathbb{R}^{LxN}$ describes the probability, for the measurement k to stimulate a recordable fluorescence photon from the pixel i. The vector s contains the expectation value for the number of fluorescence photons in each spectrum, which might be too small to be statistically significant and reliably extractable. Therefore, a synthesis step is needed to generate a unique linear combination b_j from multiple measurements to reduce statistical

variance, given as

$$b_j = \sum_{k=1}^{L} Q_{jk} s_k \qquad 1 \leq j \leq M \tag{5.3}$$

with $Q \in \mathbb{R}^{MxL}$ and $M = N$ containing weighting factors for the combination of the different spectra which are the ratio of the covered pixel area of pixel j for measurement k[‡]. By using this weighting, the dataset vector space has the same dimension as the pixel vector space, i.e. $M = N$. Furthermore, this specific weighting is similar to the naive projection without filtering in classic CT reconstruction (see chapter 2.3) and thus b is already a blurred reconstruction image which can be used as a good initial guess for the iterative reconstruction. The sum of the weighting factors used for each linear combination is equal to the number of projections n_p from which the measurements have been obtained via

$$\sum_{k=1}^{L} Q_{jk} = n_p \,. \tag{5.4}$$

Therefore, the full transfer matrix of the imaging system in XFTS is $T = QW$ and the fluorescence distribution can be obtained from the combined spectra by solving

$$b = QWx \tag{5.5}$$

for x. Figure 5.1 schematically shows the synthesis process. As these combined data are based on n_p spectra, statistical variance is reduced compared to individual spectra and extraction of the fluorescence signal can be performed more accurately.

Since the mathematical formulation of this imaging transformation is the same as for e.g. CT reconstruction, the same iterative algorithms can be used. Due to its wide usage and ease of use the Expectation Maximization algorithm is used for iterative reconstruction

[‡]Note, that here, pixels in the reconstruction space are indexed using j instead of i, as in this step the synthesis is performed to map b, resulting in $M = N$.

[141–143]. It is performed via

$$x_i^{n+1} = \frac{\sum_{j=1}^{M} T_{ji} \frac{b_j}{(Tx^n)_j}}{\sum_{j=1}^{M} T_{ji}} \cdot x_i^n \tag{5.6}$$

with the initial guess $x^0 = b$.

However, it should be noted that many alternative iterative reconstruction methods, such as conjugate gradient (CGLS) [144] or nonconvex regularization [145, 146] or extensions of the Expectation Maximization such as the introduction of a total variation step (EM-TV) [143] exist and could be used instead, but the focus of this chapter is to introduce the general principle of XFTS.

5.0.2 Quantitative XFTS Reconstruction

To obtain a quantitative marker density reconstruction, the W matrix coefficients have to be calculated based on geometric and physical properties. For each measurement k,

$$N_F^{ki} = N_0 \alpha_{ki} \sigma_F \langle l \rangle_{ki} \rho_i \tag{5.7}$$

fluorescence photons are expected to be generated by pixel i, where N_0 is the number of incident photons, α_{ki} the transmission of the incident beam k to the pixel i, σ_F the cross section for the fluorescence process, ρ_i the marker concentration in the pixel and $\langle l \rangle_{ki}$ the average length of the beam in the pixel. This length can be calculated by

$$\langle l \rangle_{ki} = \frac{w_p A_{ki}}{A_p} = \frac{A_{ki}}{w_p} \tag{5.8}$$

with w_p the pixel width (equal to the beam width), A_{ki} the covered area of the pixel by the beam, and $A_p = w_p^2$ the pixel area.

The number of detected fluorescence photons is given as

$$N_D^k = \sum_{i=1}^{N} N_F^{ki} \beta_{ki} \varepsilon_F \frac{A_D}{4\pi r_{D,ki}^2} \tag{5.9}$$

with β_{ki} the transmission of the fluorescence signal from the pixel to the detector, ε_F the detection efficiency, A_D the detector area, and $r_{D,ki}$ the detector distance. Note, that β and r_D are not only dependent on the pixel index but also on the measurement k as the target is moved and rotated between different measurements. However, the difference in the detector distance for each pixel is often small and negligible and a constant r_D can be used. Combining those equations leads to

$$W_{ki} = N_0 \alpha_{ki} \beta_{ki} \varepsilon_F \sigma_F \frac{A_{ki}}{w_p} \frac{A_D}{4\pi r_{D,ki}^2} \,. \tag{5.10}$$

Thus, the W matrix contains only a priory known parameters describing the experimental setup except for the incident and fluorescence transmission factors α and β.

Instead, α and β have to be determined based on an absorption CT scan which can be recorded in parallel using a transmission detector. While α is directly obtained from the CT result as it is the transmission at the incident beam's energy, β has to be inferred based on segmenting the resulting CT into 3 different compounds: soft tissue, bone, and air. The transmission for those compounds at the fluorescence energy can then be obtained from tabulated values, e.g. using the xraylib [54].

5.0.3 XFTS Using Multiple Detectors

To improve sensitivity, multiple detectors can be used during the measurement, increasing the covered solid angle. However, as they are positioned at different angles, the fluorescence correction matrix β is different for each detector. Assuming all detectors

are equal and positioned at the same distance, they can simply be incorporated into the reconstruction by using the sum spectrum of all n_D detectors and

$$\beta_{ki} = \sum_{m}^{n_D} \beta_{ki}^{m} \tag{5.11}$$

i.e. each matrix element is the sum of all individual detectors' fluorescence transmission factors β^m. A_D is then still the detector area of one individual detector but elements of the β matrix might become larger than one. For more complicated geometries where different detectors or different distances are used, i.e. A_D, ε, or r_D are different as well, this summing has to be performed in eq. 5.10 instead, changing to

$$W_{ki} = N_0 \alpha_{ki} \sigma_F \frac{A_{ki}}{w_p} \sum_{m=1}^{n_D} \beta_{ki}^{m} \varepsilon_F^m \frac{A_D^m}{4\pi (r_{D,ki}^m)^2} \tag{5.12}$$

5.1 XFTS Demonstration Experiment

To test the XFTS reconstruction scheme, demonstration measurements were performed at the P21.1 beamline. The cylindrical PMMA standard phantom was used for systematic studies of the performance of the XFTS algorithm for different fluorescence elements and concentrations, numbers of projections, detector positions, and numbers of incident photons. Additionally, the mouse phantom filled with different palladium concentrations was used to demonstrate the reconstruction of complex, realistic objects. A total of six detectors (Amptek XR100 FastSDD, 50 mm^2 collimated area and 1 mm thickness) were placed at scattering angles of ±30°, ±90° and ±150°. Due to geometric constraints, the detectors at ±90° had to be positioned at a distance of 60 mm, while a distance of 50 mm was used for the other four detectors. For all measurements, the continuous scanning mode (see chapter 3.2.3) with a beam size of 0.2×1 mm^2 and a pixel size of 1×1 mm^2 was used. In this configuration, an unattenuated photon flux of 8.2×10^9 photons/s was provided at the beamline and each absorber unit had a transmission ratio of around

42.6%. The overall setup as well as the notation for the different detectors is shown in figure 5.2.

5.1.1 Cylindrical Phantom Measurements

A full list of the varied parameters is given in tables 5.1 and 5.2. The number of projections n_P and the measurement duration per position were kept such that the total number of photons is independent of n_P. Due to time constraints, it was not feasible to perform absorber variations for all values of n_P. Therefore, n_{Abs} was only varied for the minimum and maximum number of projections. In total, 32 different scans were performed and each of the six detectors can be used for XFTS and XFCT reconstructions, resulting in a total of 192 individual image reconstructions.

The phantom was scanned over a range of 45 mm for each projection. The projection angles were selected to cover a total of 180°, which is sufficient for both XFTS and XFCT reconstructions but might reduce the quality of the attenuation correction. This was chosen to reduce the number of needed projections and therefore total scanning time. As multiple detectors were arranged symmetrically, the quality of the fluorescence attenuation - which is the dominating attenuation effect as discussed in chapter 3.4 - can be enhanced in combined reconstruction since systematic errors in the attenuation model will be mostly canceled out by opposing detectors.

Three different absorber configurations were used, defining the total number of photons/mm^2 N_0^{tot} summed over all projections as well as the overall radiation dose, listed in table 5.3.

Ideally, measurements should be performed at the maximum possible incident flux, limited by the detectors' count rates or beamline capabilities and for lower total radiation doses, the measurement times should be reduced. This approach would minimize the

Table 5.1 – Overview of the different scan parameters used for the cylindrical phantom measurements with palladium markers. $\rho_{1,2,3}$ designate the concentration of the fluorescence element in the three different Eppendorf tubes placed in the phantom. n_P designates the number of projections and n_{Abs} the number of absorbers used to attenuate the incident beam.

Scan ID	Element	ρ_1 [mg/ml]	ρ_2 [mg/ml]	ρ_3 [mg/ml]	n_P	Duration [s]	n_{Abs}
1	Pd	0.5	0.25	0.1	12	1	3
2					12	1	4
3					12	1	5
4					15	0.8	4
5					20	0.6	4
6					30	0.4	3
7					30	0.4	4
8					30	0.4	5
9		0.05	0.025	0.01	12	1	3
10					12	1	4
11					12	1	5
12					15	0.8	4
13					20	0.6	4
14					30	0.4	3
15					30	0.4	4
16					30	0.4	5

Table 5.2 – Overview of the different scan parameters used for the cylindrical phantom measurements with iodine markers. $\rho_{1,2,3}$ designate the concentration of the fluorescence element in the three different Eppendorf tubes placed in the phantom. n_P designates the number of projections and n_{Abs} the number of absorbers used to attenuate the incident beam.

Scan ID	Element	ρ_1 [mg/ml]	ρ_2 [mg/ml]	ρ_3 [mg/ml]	n_P	Duration [s]	n_{Abs}
17	I	0.5	0.25	0.1	12	1	3
18					12	1	4
19					12	1	5
20					15	0.8	4
21					20	0.6	4
22					30	0.4	3
23					30	0.4	4
24					30	0.4	5
25		0.05	0.025	0.01	12	1	3
26					12	1	4
27					12	1	5
28					15	0.8	4
29					20	0.6	4
30					30	0.4	3
31					30	0.4	4
32					30	0.4	5

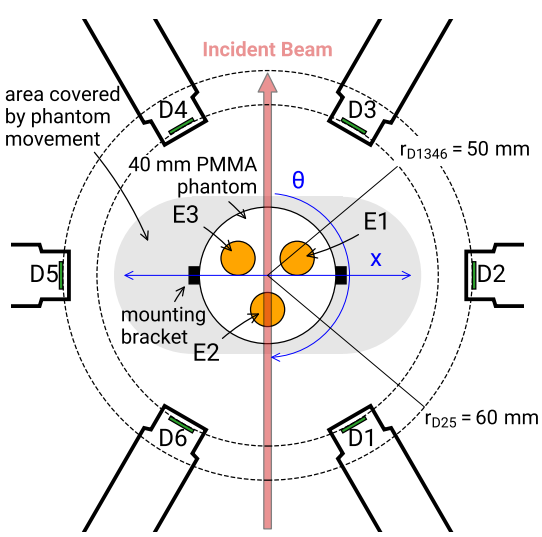

(a) Schematic drawing of the placement of the most important components.

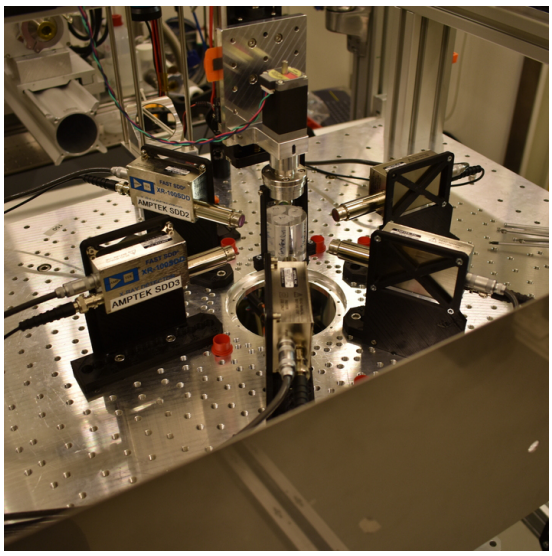

(b) Photograph of the experimental setup.

Figure 5.2 – Experimental setup of the XFTS cylinder phantom experiment.

Table 5.3 – Total number of photons and dose estimates for the different absorber configurations used for the cylindrical phantom measurements. Dose estimates are based on tabulated values [43] for a 40 mm diameter tissue-equivalent cylinder at the isocenter at 55 keV incident energy.

n_{Abs}	N_0^{tot} [photons/mm^2]	Dose Estimate [mGy]
3	7.6×10^9	248
4	3.2×10^9	105
5	1.3×10^9	43

total scan duration and is important for in-vivo experiments. However, tests have shown that the current control software only reliably works for targeted acquisition durations per pixel $\geq 0.2\,\mathrm{s}$ with substantial jitter in the resulting acquisition times and $\geq 0.4\,\mathrm{s}$ for a high-quality scan. This timing constraint is mainly given by the need to acquire 5 beam profile measurements per pixel for the transmission image, which has to be trans-

ferred as raw data from the beamline's control system instance. Furthermore, acquisition triggering is completely software-controlled, based on the state of multiple Tango device servers, some of which internally communicating over a serial interface to the hardware. This architecture was chosen, as it offers the greatest flexibility for which optimal timing was sacrificed. However, in dose-relevant 3D scanning applications, this means that the incident flux has to be attenuated to meet the software requirements, increasing the overall scan time. It was thus decided to adjust the scan parameters such that the minimal acquisition time per pixel was 0.4 s and different radiation doses were achieved by varying the absorber count. As a result, each scan took around 10 minutes. As a reference, the detectors would have been able to sustain count rates using only one absorber, resulting in scan times between around 30 seconds for the low dose scans and 2 minutes for the high dose scans without the timing limitations of the scanning software. This would correspond to only 13 ms for the shortest acquisition time per pixel for the lowest dose scans with 30 projections (equivalent to scan IDs 8, 16, 24 and 32 in tables 5.1 and 5.2).

Figure 5.3 shows an example spectrum (scan ID 12) with the beam intersecting the Eppendorf tube containing 0.01 mg/ml palladium at the center, as well as the combined spectrum used as input for the fit in the XFTS reconstruction. In figure 5.3a, the influence of the detector angle on the overall spectrum is visible, with the Compton scattered photons changing the high energy region as well as the total counts of the spectrum, while the fluorescence signal is nearly constant. Figure 5.3b demonstrates the improvement in the statistical fluctuations when applying the spectrum combination in XFTS compared to an individual spectrum as used in XFCT, which reveals the Pd fluorescence line at 21 keV. These spectra are the input to the signal fitting in the respective reconstruction algorithms.

For each measurement, both XFTS and XFCT reconstructions were performed as de-

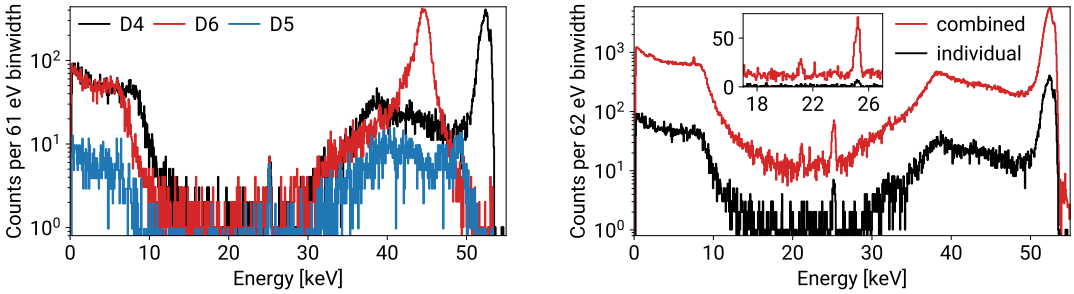

(a) Recorded spectra at different scattering angles showing the angle-dependent Compton scattering

(b) Comparison between an individual spectrum and the combined spectrum used in XFTS (D4)

Figure 5.3 – Example spectra from a cylindrical phantom scan with the beam intersecting an Eppendorf tube containing 0.01 mg/ml palladium. Detector-intrinsic Sn fluorescence is present at 25 keV and Pd fluorescence at 21 keV.

scribed in section 5.0.1 for each of the six detectors. Similar to 2D scans for the cell-tracking pilot studies in chapter 4, a significance threshold was applied during peak fitting, to reduce noise in the input to the iterative reconstruction. If the significance is lower than this limit, the fluorescence count of the spectrum is set to zero independent of the fit result. Compared to one single measurement of a sample or a 2D scan, this limit can be relaxed to a lower significance, as some noise in a single projection will be filtered by the iterative reconstruction. A minimum significance limit of 1.6 (corresponding to a 90% confidence limit) has proven to yield the best results. Furthermore, reconstruction of the combined data of all detectors as given in section 5.0.3 was performed.

Since the true marker distribution is known, the cylinder phantom measurements can be used to find the optimal parameters for the reconstruction and quantify the quality of the XFTS reconstruction algorithm, allowing to compare it to the XFCT method. The attenuation contributions for the incident and fluorescence photons can be calculated using the a priory known shape of the phantom. Attenuation is calculated using the xraylib database and its predefined materials for air and PMMA. The difference in

the attenuation coefficient between PMMA and water in the Eppendorf tubes can be neglected.

An important parameter to be decided is the number of iterations of the ML-EM reconstruction. It has been shown that noise can be amplified [147] when using too many iterations, therefore it is important to stop the iteration at the optimal point. However, this point can only be found when using a known distribution for reconstruction, as it is the case for the cylinder phantom measurements. To quantify the reconstruction quality, three metrics often used in image processing are employed:

- Normalized root mean squared error (NRMSE)

  The NRMSE provides a simple way to estimate the accuracy of the reconstructed data r of the ground truth t. Using Euclidean normalization it is calculated via [148]

  $$NRMSE = \frac{\sqrt{\langle (r-t)^2 \rangle}}{\sqrt{\langle t^2 \rangle}} \tag{5.13}$$

  where $\langle x \rangle$ is the mean value of the distribution x.

- Peak signal-to-noise ratio (PSNR)

  PSNR is most often used for quality assessment of compressed data but has also been applied to image reconstruction. It is commonly expressed in dB and calculated via

  $$PSNR = 10 \log_{10} \left(\frac{\max(t)^2}{\langle (t-r)^2 \rangle} \right) \tag{5.14}$$

- Structural similarity (SSIM)

  The SSIM was established in an effort to develop a metric that is more in line with human perception of similarity than metrics like NRMSE and PSNR [149]. It compares sliding windows of the true and reconstructed image to take the local structure in both datasets into account. SSIM provides an output value between 0

and 1, where larger values indicate greater similarity. Its calculation is detailed in [149].

Figure 5.4 shows these metrics for different iterations. It can be seen that XFCT reaches its optimal point much earlier than XFTS. This is expected, as the reconstruction space for XFCT is smaller than for XFTS which used linear combinations of the raw measurements and is therefore overdetermined. For XFCT, a total of 5-10 iterations is optimal and image quality quickly drops off for both fewer and more iterations. For XFTS, a much wider range between 60 and 120 iterations is ideal, demonstrating greater stability. In both algorithms, different metrics have a different optimal number of reconstruction iterations and a balance has to be found between them. As SSIM has been shown to have the best agreement of those three metrics to human classification of image quality [150] it was selected as the primary metric and reconstruction iterations were chosen to predominantly favor a good SSIM value. Therefore, 6 iterations for XFCT and 100 for XFTS were selected for further analysis. Figure 5.6 shows a representative selection of the reconstruction results.

Figure 5.4 already suggests that both algorithms perform similarly when a strong fluorescence signal is present but XFTS provides better image quality - and higher sensitivity - than XFCT in cases of weak signals. To further investigate this, a signal strength quantity S is used, given by $S = \sqrt{D} \cdot \rho_F$ where D is the radiation dose and ρ_F the fluorescence marker concentration. This definition is based on the definition of and proportional to the significance in section 3.3.3 and allows comparing measurements where both, marker concentration and the number of incident photons, are varied. Using this quantity, figure 5.5 shows the reconstructed to true mass ratios as well as the image quality metrics for different S-values for each individual detector as well as the combination of all detectors.

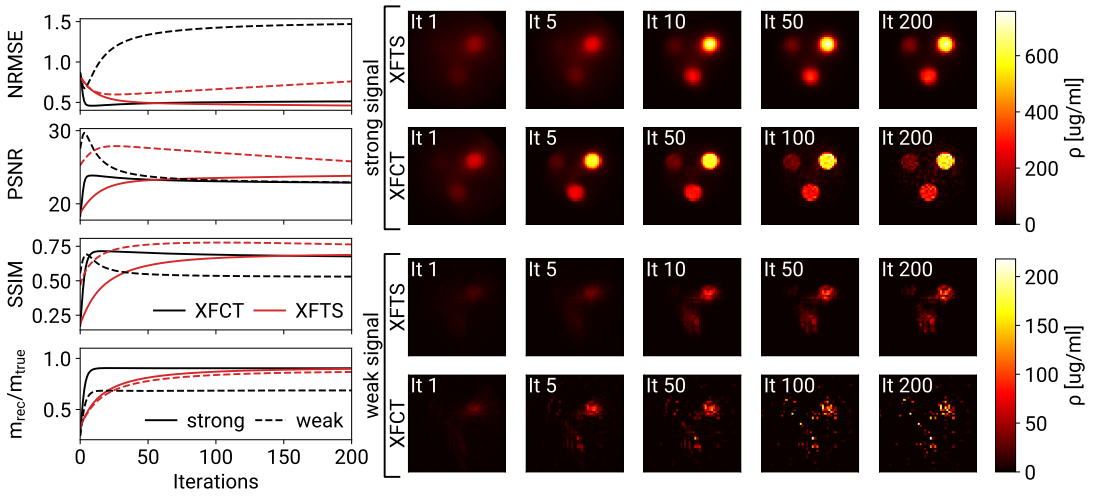

Figure 5.4 – Reconstruction results for different iterations for two measurements with palladium markers. Strong signal corresponds to scan ID 6 using all detectors for reconstruction, weak signal to scan ID 16 using only one detector (D1)

XFTS consistently provides a more accurate mass reconstruction for lower signal strengths and XFCT approaches the XFTS results for higher signal strengths. The same is true for PSNR and SSIM metrics, while NRMSE is comparable for both methods. Between palladium and iodine, the most notable difference is that reconstructed masses for palladium are systematically too low (between 5 and 10 %) even for high signal strength, independent of the reconstruction method. This might suggest limitations of the material-segmentation approach where attenuation coefficients at the fluorescence energy are inferred from a material database instead of being measured.

An important difference between the reconstruction results of XFCT and XFTS - which is not directly represented in the image metrics - is that XFCT has shown to result in sharper reconstructions for strong signals, as visible in figure 5.4. This might stem from the fact that XFTS uses an initial guess with $1/|r|$ point spread function, which cannot completely be recovered during the iterations. Overall, it can be stated that XFTS does

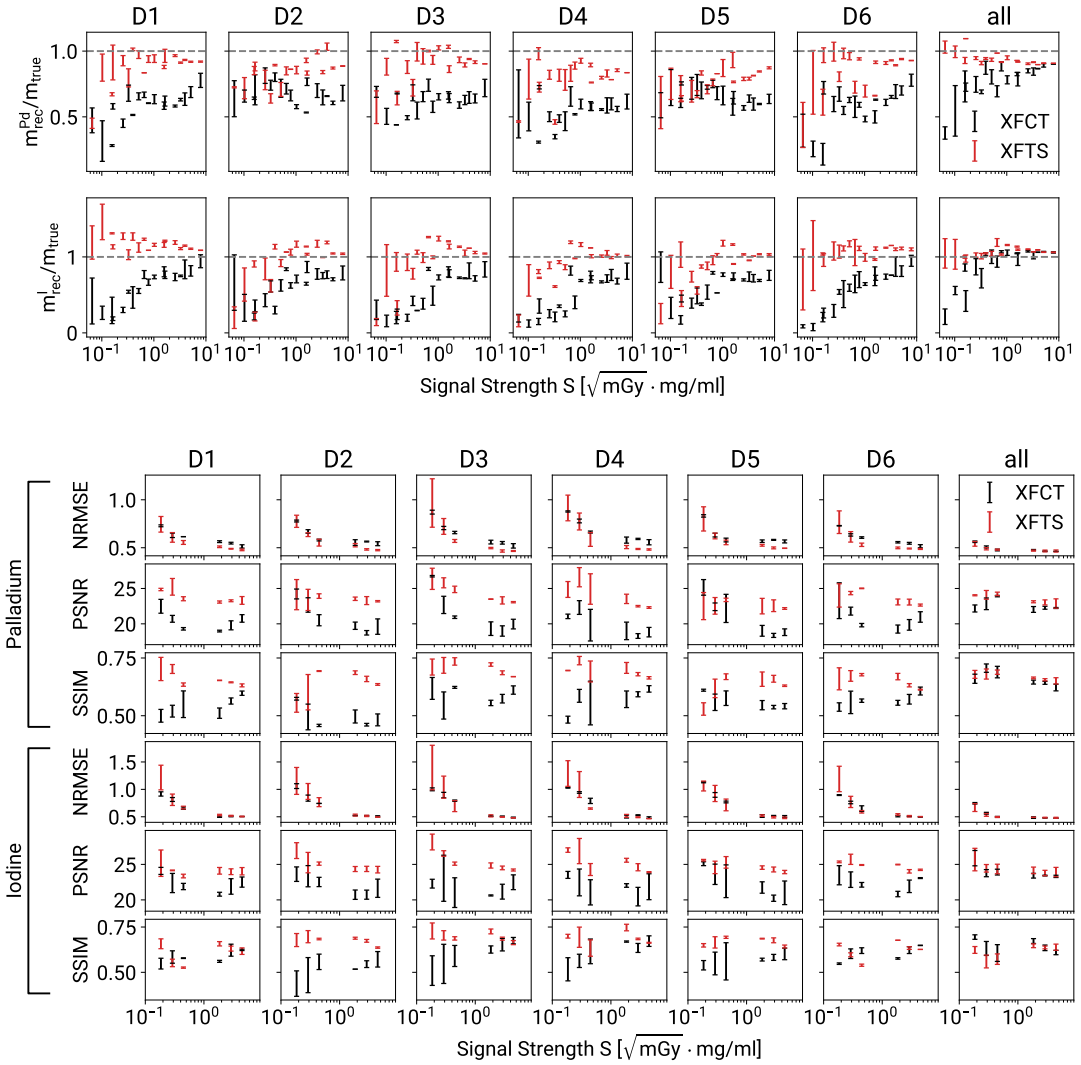

Figure 5.5 – Reconstructed mass ratio (top) and image quality metrics (bottom) for different signal strengths. The mass ratio can be calculated for each individual Eppendorf tube while image metrics combine all three tubes per image, resulting in fewer data points. For the calculation of the signal strength, the average concentration was used for the latter. Data points are mean values and standard deviations for all matching measurements (i.e. with different numbers of projections).

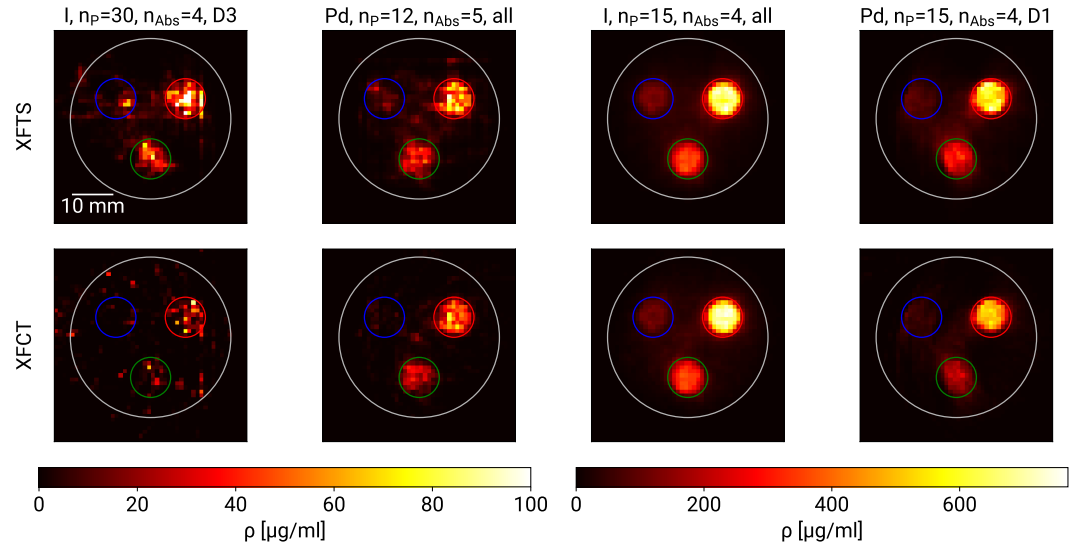

Figure 5.6 – Representative selection of reconstructions for different scans. The top row shows the XFTS and the bottom row the XFCT reconstruction. From left to right, the corresponding scan IDs from tables 5.1 and 5.2 are 31 (D3), 11 (all detectors), 20 (all detectors) and 4 (D1).

provide a significantly better image reconstruction for weak signals and has a higher sensitivity than the conventional XFCT reconstruction. However, for stronger signals, XFTS does not offer a benefit regarding image metrics with XFCT providing sharper images. As both reconstructions work on the same input data, both algorithms may be employed and the better result can be used depending on the signal strength.

For this phantom, only small quality differences can be seen for different numbers of projections, as shown in figure 5.6 since the marker distribution has a relatively simple shape and no small details are present.

5.1.2 Mouse Phantom Measurements

To demonstrate XFTS for a more realistic application, the mouse phantom (see section 3.2.5) was scanned in the same experimental setup. To simulate different fluorescence marker organ uptakes, palladium was diluted in agarose gel and filled into the corresponding cavities. Concentrations of 0.02 mg/ml in the lungs, 0.01 mg/ml in the liver and 0.03 mg/ml in the kidneys were used. The mouse was placed vertically into a 38 mm diameter PMMA tube with 1.5 mm wall thickness. This tube is equivalent to the one in the commercial in-vivo imaging cells used during the experiments in chapter 4.4.

The phantom was scanned in a 45 mm × 76 mm region using 15 projections from 0° to 180°, pixel size of $1 \times 1\,\mathrm{mm}^2$, beam size of $0.2 \times 1\,\mathrm{mm}^2$ and acquisition times per pixel of 0.2 s. As discussed in section 5.1.1, such short acquisition times do introduce some jitter in the real measurement times, but had to be accepted to keep the overall measurement duration within the available time. Three scans were performed with different absorber settings, as listed in table 5.4. Including motor movements, each scan took around 3 hours to complete. Again, the duration was heavily limited by the scanning software, while the hardware would have supported much faster measurements of around 30 minutes. Additionally, the same parameter variation as performed for each set of Eppendorf tubes in the cylindrical phantom was applied to a single slice in the kidney region, allowing for validating the previous results for a more complex geometry.

Due to the complex geometry of the mouse phantom and the different attenuation properties of its materials, segmentation of the reconstruction space to different materials has to be performed via a transmission CT. Transmission data are available via the x-ray eye detector and reconstruction is performed using filtered back-projection (FBP). For segmentation into materials, the reconstructed image was filtered and smoothed using a combination of median and Gaussian filters for removing 'salt-and-pepper' noise [151].

Table 5.4 – Total number of photons and dose estimates for the different absorber configurations used for the mouse phantom measurements. Dose estimates are based on tabulated values [43] for a 25 mm diameter tissue-equivalent cylinder at the isocenter at 55 keV incident energy.

n_{Abs}	N_0^{tot} [photons/mm^2]	Dose Estimate [mGy]
1	10.5×10^9	345
2	4.5×10^9	148
3	1.9×10^9	62

Afterwards, two thresholds were used to separate air-like, tissue-like, and bone-like materials. The threshold values were selected by hand to visually match the non-segmented image. Figure 5.7a shows the FBP reconstruction, the filtered image as well as the segmented image for different numbers of projections. By applying the Gaussian and median filter, the contrast in the image is strongly increased, yielding a good separation between the different materials. For fewer numbers of projections, some artifacts are present in the segmented image, mostly at the thin-walled imaging cell. However, the effect of these artifacts on the attenuation calculation is small. Overall it can be seen that already a low number of projections can be used for a sufficient anatomic reconstruction in the context of attenuation correction.

Figure 5.7b shows a comparison of the measured transmission at one projection angle compared to the transmission calculated using the tabulated attenuation coefficients from the segmented materials. A good agreement between these two images is present, validating that the segmentation process can be used to obtain accurate transmission information and that the chosen materials from the NIST database are matching the phantom's ones.

Fluorescence reconstruction was performed analogously to the cylinder phantom using 6 iterations for XFCT and 100 iterations for XFTS and reconstruction was performed for

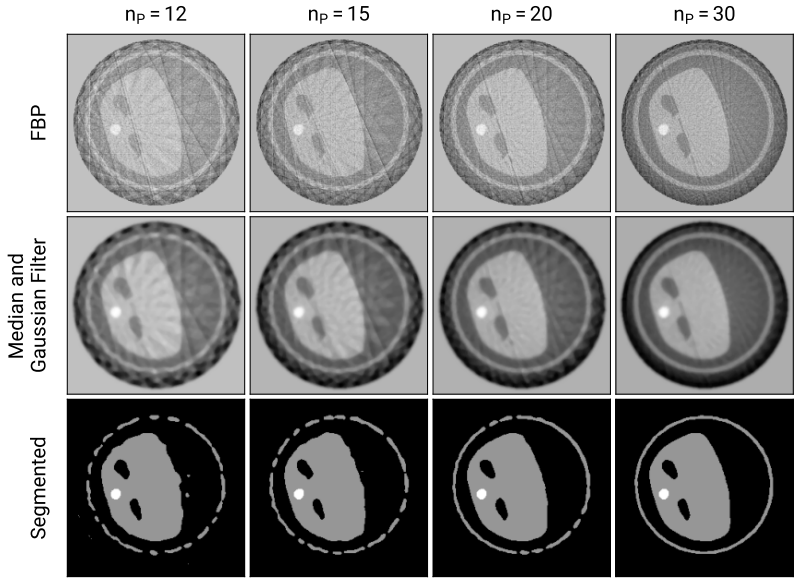

(a) Segmentation quality for different numbers of projection angles.

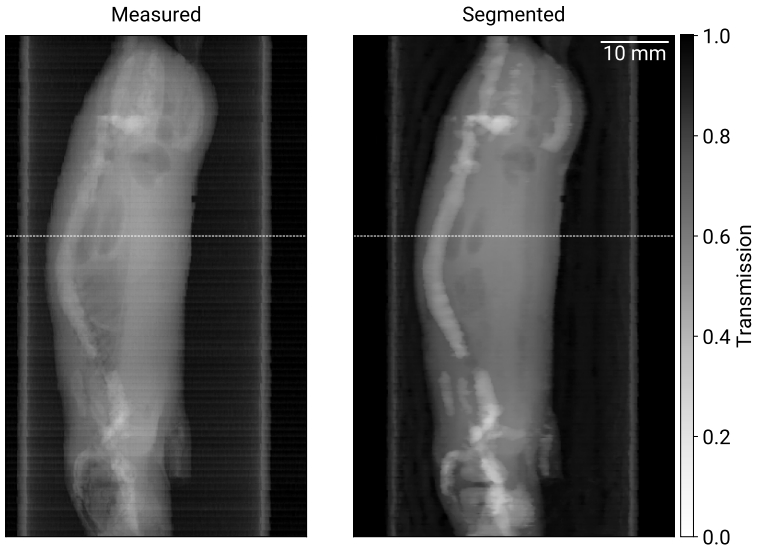

(b) Comparison of measured transmission and transmission calculated from segmented materials.

Figure 5.7 – Segmentation of CT data for obtaining attenuation coefficients. The dashed line in (b) indicates the height of the slice shown in (a).

each individual detector as well as for the combined data of all detectors. A comparison between the two reconstruction results using XFTS and XFCT for the 146 mGy scan as well as the expected distribution is shown in figure 5.8. The expected distribution was calculated using the Digimouse voxel model, on which the phantom is based. However, some differences are expected: In the physical model, the smallest features could not be manufactured, resulting in some missing bones, especially the rips. Furthermore, both, the transmission CT data and the fluorescence reconstruction suggest that the kidney cavity had not been filled completely with the agarose gel, but a small gap was present between the two halves, visible in figure 5.7a. Additionally, a strong Pd fluorescence signal is present along the spine near the head in the upper half of the model with larger concentrations than in the organs. This Pd signal is present as palladium solution had flowed into the gypsum cavity during preparation of an earlier experiment. Since this signal is much stronger than the concentrations used in this experiment, the fluorescence colormaps were limited to the signal range of the organ signals. Besides these expected differences, an overall good agreement between both reconstruction methods as well as the modeled result is present. The maximum density projection also reveals a clear distinction between the marker concentrations in the different organs, matching the concentration differences in the used solutions.

The reconstructed masses for the different scans are compared in figure 5.9. For both methods, the different organs are separable using only 15 projections. Consistent with the results of the cylinder phantom measurement, XFTS and XFCT results are in good agreement at the highest doses, yielding around 55 µg palladium distributed in the full body. The reconstructed mass in the XFCT reconstruction becomes lower when using lower doses or only one detector. This is a result of the limited statistics in each individual spectrum, where the signal cannot reach the significance threshold. For the lowest statistics, the reconstructed mass starts to increase again. In these measurements, only a few (often less than ten) total counts are present in the signal region and the approx-

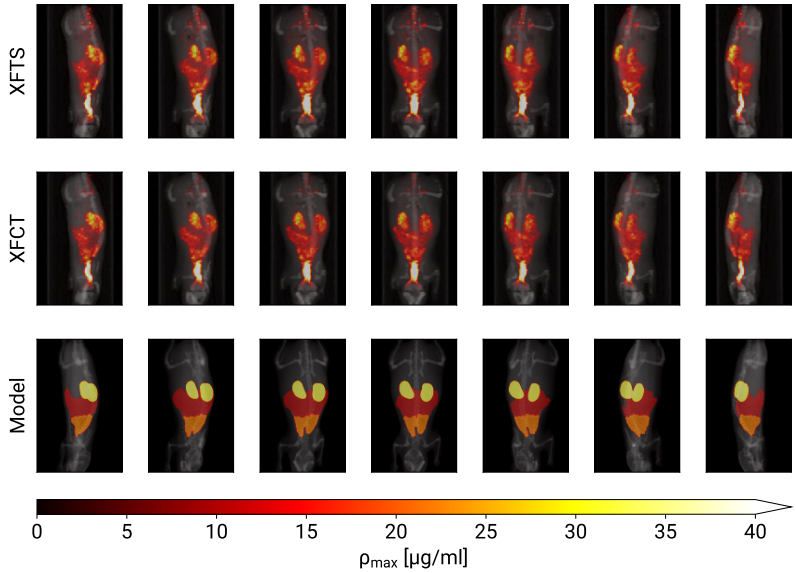

(a) Maximum value projection.

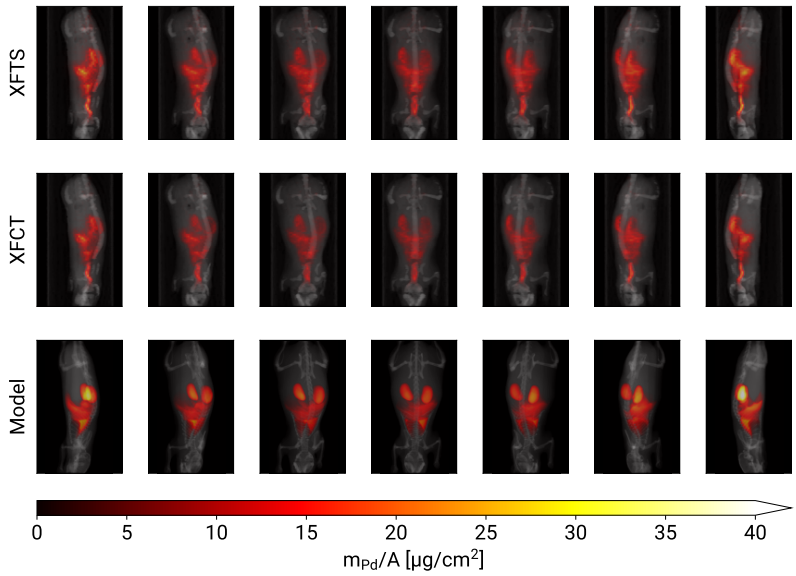

(b) Summed mass per area along the projection axis.

Figure 5.8 – Reconstruction result of the 146 mGy mouse phantom scan using all detectors.

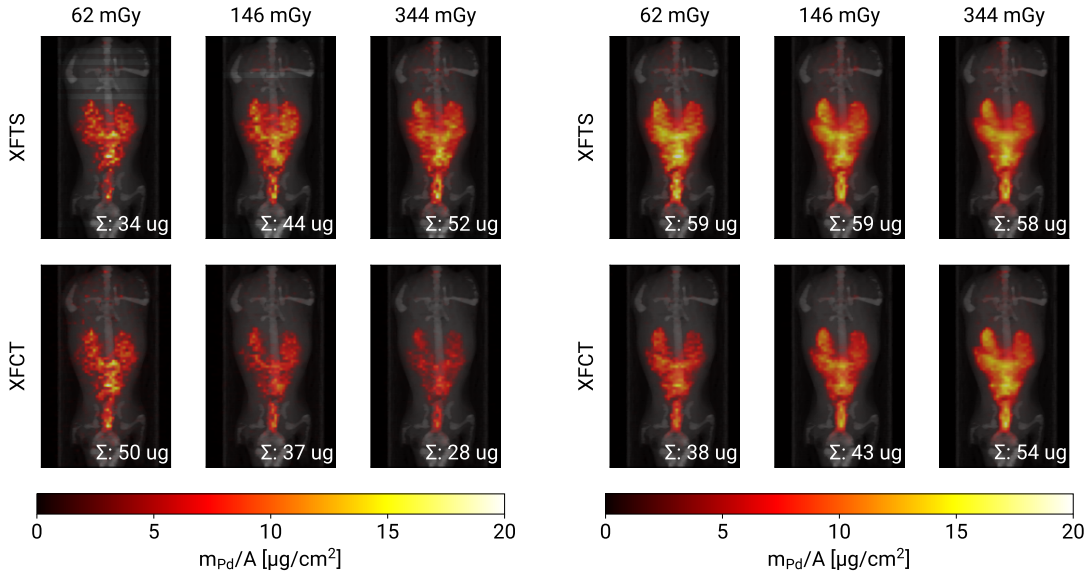

(a) Mass projection for detector D1.

(b) Mass projection for all detectors.

Figure 5.9 – Mass projections for the different dose scans using only one detector (left) and all detectors (right). The total reconstructed mass in each scan is denoted in the lower right corner of each image.

imation for the significance $Z = N_S/\sqrt{N_B}$ is not strictly valid anymore. The increase in reconstructed mass is therefore most likely attributable to statistical noise and can even increase to much higher values for a lower (or no) minimal significance limit. For XFTS, mass reconstructions and image quality are stable also for lower doses. Using all detectors, hardly any difference is visible between 62 mGy and 344 mGy. For a single detector, some artifacts can be seen at 146 mGy and only a deteriorated reconstruction is achieved at 62 mGy. However, for neither method, the absolute limit of detection was reached as all reconstructions show fluorescence in each organ.

5.1.3 Detection Limits and Comparison to Simulations

As the detection limit could not be determined sufficiently during the experiment, simulations are used to obtain an estimate. To validate the simulation results, the cylinder phantom experiment was recreated in a Geant4 simulation. Only one scan configuration was used, namely the scan with low palladium concentrations, 15 projection angles, and 4 absorbers (scan ID 12). This scan was chosen, as it closely resembles the parameters that were also used in the mouse phantom scans. Nevertheless, by comparing fluorescence signal strength, Compton scattering background shape, and the absolute number of detected photons of the simulated and recorded spectra high confidence in the general validity of the simulation output even for different fluorescence concentrations or marker elements can be obtained. Figure 5.10 shows a comparison between simulated and measured spectra. For increased statistics, the sum spectrum of all individual measurements of a single projection is compared. As the setup is symmetric and spectra are nearly identical for the mirrored detector positions, only three of the six detectors are shown. 3.2×10^9 photons/mm^2 were simulated, matching the measured flux of the experiment and no scaling between simulation and data was applied. Good agreement between both spectra is achieved for the overall spectral shape, the background level in the fluorescence region, and the palladium fluorescence strength at 21 keV. In contrast, the simulated detector intrinsic tin fluorescence at 25 keV does not agree well with the data, especially at 90° scattering angle. This is most likely because no details about the exact location of tin inside the detector are available and the currently used model seems to not be entirely correct. However, since palladium and tin fluorescence do not spectrally overlap, this is not an issue for determining the palladium fluorescence sensitivity limit.

After showing that the experimental results can be recreated with good agreement in Geant4, two slices of the Digimouse voxel model were simulated to obtain detection limits for palladium accumulations in the kidneys and liver. Simulation output was analyzed

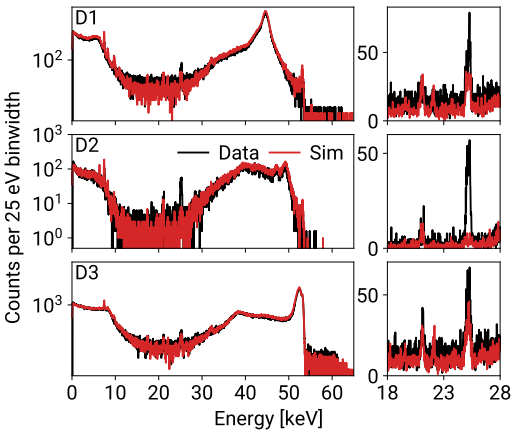

Figure 5.10 – Comparison between the simulated and measured sum spectrum of one projection angle of the cylinder phantom with palladium for detectors D1, D2, and D3.

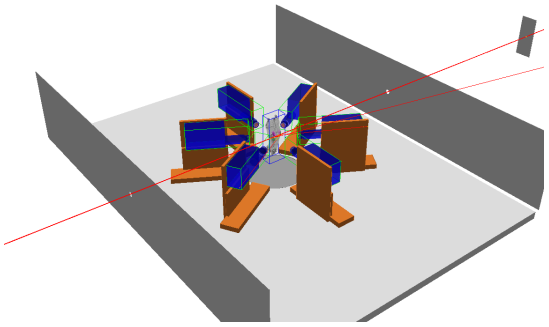

Figure 5.11 – Screenshot of the mouse phantom simulation.

the same as the experimental data, i.e. segmentation of the materials was performed using transmission CT and fluorescence counts were extracted by fitting the simulated spectra. No additional knowledge taken from the simulation was used. For each organ, marker concentrations were varied using 30, 20, 10, 7.5, 5, 2.5, 1.5, 1, 0.5 and 0.1 µg/mL and were simulated at different dose levels of 50, 150 and 300 mGy. A screenshot of the simulation geometry is shown in figure 5.11. In figure 5.12c, examples of the reconstructed distributions in the liver for different signal strengths are shown. For determining the sensitivity limit, evaluation of the mean signal significance $\langle Z \rangle$ has been shown to be a useful quantity. This value corresponds to the mean significance of the spectrum fit of all spectra at which a true signal is present. For XFTS, the 2D fluorescence distribution can directly be used, as a synthesized spectrum is available for each spatial pixel while for XFCT reconstruction, the sinogram of the true fluorescence distribution is used to determine the included spectra. In figure 5.12a it can be seen that both the SSIM value of the reconstructed image and the accuracy of the reconstructed Pd mass in the organ

Table 5.5 – Sensitivity limits for the XFTS and XFCT reconstructions for Pd in the liver and kidneys. Values are given in terms of signal strengths as well as concentrations for the typical maximal radiation dose for in-vivo measurements.

	XFCT		XFTS	
	S [$\sqrt{\text{mGy}}$ mg/ml]	ρ_{min}@300 mGy [µg/ml]	S [$\sqrt{\text{mGy}}$ mg/ml]	ρ_{min}@300 mGy mGy [µg/ml]
kidneys	0.123	7.12	0.019	1.08
liver	0.066	3.79	0.011	0.65

are constant for higher signal strengths and have a clear cutoff at which they become worse. For both organs, this cutoff value is at lower signal strengths for XFTS than for XFCT, demonstrating again the improved sensitivity of XFTS. Empirically, a good agreement between this cutoff strength and a drop of the mean significance $\langle Z \rangle$ below 3 was found. Since $\langle Z \rangle$ inhibits a clear linear correlation to the signal strength, a linear fit of $\langle Z \rangle$, shown in figure 5.12b, can therefore be used to find a simple approximation of the sensitivity limit for both methods. The obtained limits are listed in table 5.5. For both organs, the sensitivity was improved by a factor of approximately six compared to XFCT and - as expected due to its larger volume - lower concentrations can be seen in the liver than in the kidneys. At maximum in-vivo dose, kidney concentrations down to 1.08 µg/ml and liver concentrations down to 0.65 µg/ml are detectable. This corresponds to a total mass in this slice of 72 ng and 110 ng respectively, and the maximum mass in the beam volume is around 20 ng/mm^2 for both organs. This is in good agreement with the 120 ng/mm^2 detection limit obtained for the thyroid scans in chapter 4.1 when taking the effects of the improved detector setup and the difference between iodine and palladium fluorescence cross section and detection efficiency into account. Thus, it can be shown that no sensitivity penalty is present when using XFTS-based 3D imaging compared to 2D XFI scans.

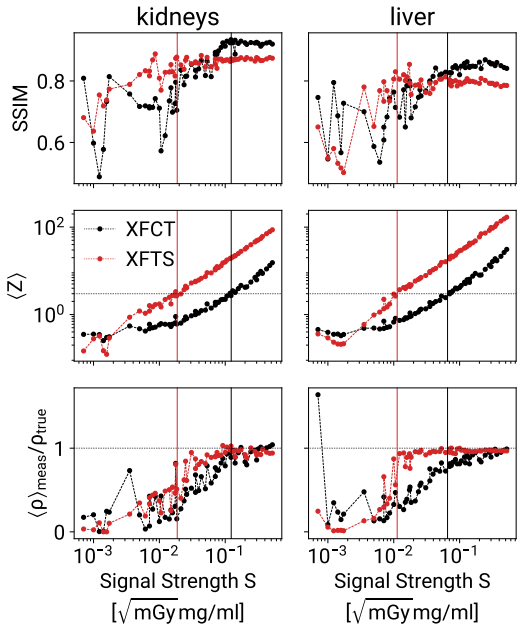

(a) Reconstruction metrics for XFTS and XFCT algorithms.

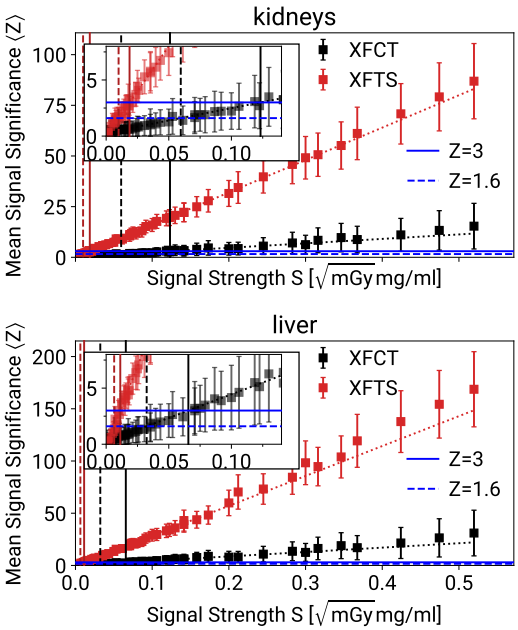

(b) Mean significance for simulation fits at signal positions.

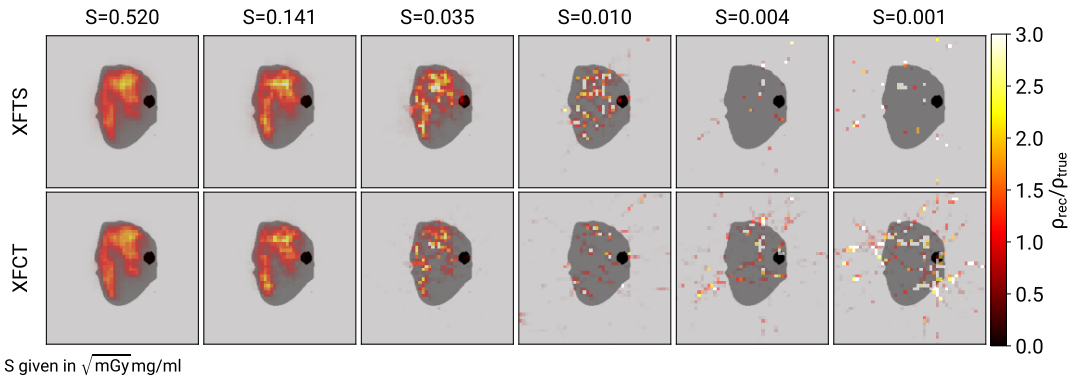

(c) Reconstruction results at different signal strengths.

Figure 5.12 – XFTS and XFCT reconstruction and corresponding metrics of simulations of the kidneys and liver with different signal strengths.

6 Conclusion and Outlook

The pilot studies performed in this thesis demonstrate a clear path towards the usage of synchrotron-based XFI as an alternative imaging modality for preclinical cell tracking and pharmacokinetics. The experiments provide valuable information about the required infrastructure for such studies, achievable sensitivity, but also limitations at the current stage. The main limitation for quantitative imaging was shown to be the variable attenuation of both incident and fluorescence photons in 2D imaging. Furthermore, advances in cell loading using palladium nanoparticles or the use of other marker materials are needed to achieve multiplexed in-vivo XFI.

So far, only macrophages were tracked, but they are only one part of the immune system. To obtain greater insights, also other important cell types have to be observed, most importantly different types of T-cells. As they are much smaller than macrophages, labeling has shown to be more difficult, and only a much smaller uptake was achieved so far [89].

The biggest hurdle for quantitative analysis in the presented cell tracking XFI studies is the complex attenuation correction. One promising approach to mitigate this issue is the use of multiple detectors, which should reduce the variance between different regions in the target as indicated in chapter 3.4. However, more detailed studies are needed to verify that this holds true for different detector distances or sample geometries.

Alternatively, this issue can be circumvented by performing a full 3D reconstruction, where attenuation models can be included much more accurately and segmentation of the obtained marker distribution to organs is easier. Specifically, the XFTS algorithm

proposed in chapter 5 can be used to obtain a 3D fluorescence reconstruction with sufficient spatial resolution and high quantitative accuracy without the radiation dose penalty of XFCT imaging. With the current experimental setup, XFCT and XFTS imaging is limited to in-situ measurements, as the scan times are too long for in-vivo applications. However, this is only limited by the software currently in use and not due to hardware or physical limitations such as detector count rate or incident flux. An important future improvement is thus to implement a hardware-based triggering for the scans to reduce the acquisition time, enabling in-vivo XFTS scans. The main limitation of the XFTS reconstruction compared to the traditional XFCT method is the loss of spatial resolution, leading to a blurred reconstructed image. This is an inherent drawback of the synthesis approach, similar to tomosynthesis used in absorption imaging. However, modification of the iterative algorithm such as the introduction of a total variation step, might improve the resolution to some extent [152] and should be compared to the current results.

The XFTS experiments also used a modified experimental setup compared to the cell tracking studies in chapter 4, as more detectors with thicker detector chips have become available. Additionally, the mouse phantom was placed vertically, allowing to position the detectors closer to the sample. Using the sensitivity scaling law $Z \propto \sqrt{\varepsilon\Omega}$ this upgraded setup promises to improve the sensitivity by a factor of four. Organ uptake down to concentrations of 650 ng/ml for palladium are detectable and similar values are expected for iodine. This improvement is also expected for 2D imaging, thus with this setup, detection of palladium-labeled MHS cells in chapter 4.3 would have been better visible and the sensitivity can further be improved in the future by using even more detectors.

Demonstrating the successful tracking of iodine-labeled macrophages in-vivo, synchrotron-based XFI has shown to be a useful imaging modality and can in the future be applied to not only pilot studies but also in preclinical medical research. While the focus of this

thesis was the application to cell tracking and immunology, XFI is a versatile modality for many kinds of functional imaging, such as pharmacokinetics or oncology and might in the future be able to fill the existing gap in functional imaging between PET, MRI, and BLI.

Bibliography

[1] W. C. Röntgen. "On a New Kind of Rays". In: *Science* 3.59 (Feb. 1896), pp. 227–231. DOI: 10.1126/science.3.59.227.

[2] Joel D. Howell. "EARLY CLINICAL USE OF THE X-RAY". In: *Trans. Am. Clin. Climatol. Assoc.* 127 (2016), p. 341. URL: https://www.ncbi.nlm.nih.gov/pmc/articles/PMC5216491.

[3] Seynaeve P. C. and Broos J. I. "The history of tomography". In: *J. Belge Radiol.* 78.5 (Oct. 1995), pp. 284–288. URL: https://europepmc.org/article/med/8550391.

[4] G. N. Hounsfield. "Computerized transverse axial scanning (tomography): Part 1. Description of system". In: *The British Journal of Radiology* 46.552 (1973). PMID: 4757352, pp. 1016–1022. DOI: 10.1259/0007-1285-46-552-1016. eprint: https://doi.org/10.1259/0007-1285-46-552-1016. URL: https://doi.org/10.1259/0007-1285-46-552-1016.

[5] P. C. Lauterbur. "Image Formation by Induced Local Interactions: Examples Employing Nuclear Magnetic Resonance". In: *Nature* 242 (Mar. 1973), pp. 190–191. DOI: 10.1038/242190a0.

[6] Vijay P. B. Grover et al. "Magnetic Resonance Imaging: Principles and Techniques: Lessons for Clinicians". In: *Journal of Clinical and Experimental Hepatology* 5.3 (Sept. 2015), p. 246. DOI: 10.1016/j.jceh.2015.08.001.

[7] Mark A. Haidekker. "Magnetic Resonance Imaging". In: *Medical Imaging Technology*. New York, NY: Springer New York, 2013, pp. 67–96. DOI: 10.1007/978-1-4614-7073-1_5. URL: https://doi.org/10.1007/978-1-4614-7073-1_5.

[8] Lauren Scarfe et al. "Preclinical imaging methods for assessing the safety and efficacy of regenerative medicine therapies". In: *npj Regener. Med.* 2.28 (Oct. 2017), pp. 1–13. DOI: 10.1038/s41536-017-0029-9.

[9] Shan Tong, Adam M. Alessio, and Paul E. Kinahan. "Image reconstruction for PET/CT scanners: past achievements and future challenges". In: *Imaging Med.* 2.5 (Oct. 2010), p. 529. DOI: 10.2217/iim.10.49.

[10] Mark A. Haidekker. "Nuclear Imaging". In: *Medical Imaging Technology*. New York, NY, USA: Springer, New York, NY, Apr. 2013, pp. 55–66. DOI: 10.1007/978-1-4614-7073-1_4.

[11] Ali Douraghy and Arion F. Chatziioannou. "Preclinical Imaging". In: *Basic Sciences of Nuclear Medicine*. Berlin, Germany: Springer, Oct. 2010, pp. 379–413. DOI: 10.1007/978-3-540-85962-8_18.

[12] V. Koo, P. W. Hamilton, and K. Williamson. "Non-invasive in vivo imaging in small animal research". In: *Cell. Oncol.* 28.4 (2006), pp. 127–139. DOI: 10.1155/2006/245619. eprint: 16988468.

[13] Simon R. Cherry and Sanjiv S. Gambhir. "Use of Positron Emission Tomography in Animal Research". In: *ILAR J.* 42.3 (Jan. 2001), pp. 219–232. DOI: 10.1093/ilar.42.3.219.

[14] Douglas Hanahan. "Transgenic Mice as Probes into Complex Systems". In: *Science* 246.4935 (Dec. 1989), pp. 1265–1275. DOI: 10.1126/science.2686032.

[15] Ravi P. Misra and Stephen A. Duncan. "Gene targeting in the mouse". In: *Endocrine* 19.3 (Dec. 2002), pp. 229–238. DOI: 10.1385/ENDO:19:3:229.

[16] Ming Xu et al. "How Entanglement of Different Physicochemical Properties Complicates the Prediction of in Vitro and in Vivo Interactions of Gold Nanoparticles". In: *ACS Nano* 12.10 (Oct. 2018), pp. 10104–10113. DOI: 10.1021/acsnano.8b04906.

[17] Fatemeh Ahmadpoor, Atif Masood, Neus Feliu, Wolfgang J. Parak, and Seyed Abbas Shojaosadati. "The Effect of Surface Coating of Iron Oxide Nanoparticles on Magnetic Resonance Imaging Relaxivity". In: *Front. Nanotechnol.* 0 (2021). DOI: 10.3389/fnano.2021.644734.

[18] Weijun Wei et al. "ImmunoPET: Concept, Design, and Applications". In: *Chem. Rev.* 120.8 (Apr. 2020), pp. 3787–3851. DOI: 10.1021/acs.chemrev.9b00738.

[19] Carlos Sanchez-Cano et al. "X-ray-Based Techniques to Study the Nano–Bio Interface". In: *ACS Nano* 15.3 (Mar. 2021), pp. 3754–3807. DOI: 10.1021/acsnano.0c09563.

[20] Amelie Heuer-Jungemann et al. "The Role of Ligands in the Chemical Synthesis and Applications of Inorganic Nanoparticles". In: *Chem. Rev.* 119.8 (Apr. 2019), pp. 4819–4880. DOI: 10.1021/acs.chemrev.8b00733.

[21] Michael M. Boyiadzis et al. "Chimeric antigen receptor (CAR) T therapies for the treatment of hematologic malignancies: clinical perspective and significance". In: *J. ImmunoTher. Cancer* 6.1 (Dec. 2018), p. 137. DOI: 10.1186/s40425-018-0460-5.

[22] Laura M. Lechermann et al. "Detection limit of 89Zr-labeled T cells for cellular tracking: an in vitro imaging approach using clinical PET/CT and PET/MRI". In: *EJNMMI Res.* 10.1 (Dec. 2020), pp. 1–12. DOI: 10.1186/s13550-020-00667-5.

[23] Naoko Nose et al. "[18F]FDG-labelled stem cell PET imaging in different route of administrations and multiple animal species". In: *Sci. Rep.* 11.10896 (May 2021), pp. 1–8. DOI: 10.1038/s41598-021-90383-4.

[24] Aditya Bansal et al. "Novel 89Zr cell labeling approach for PET-based cell trafficking studies". In: *EJNMMI Res.* 5.1 (Dec. 2015), pp. 1–11. DOI: 10.1186/s13550-015-0098-y.

[25] Yanlu Lv et al. "In vivo simultaneous multispectral fluorescence imaging with spectral multiplexed volume holographic imaging system". In: *J. of Biomedical Optics, 21(6).* Vol. 21. 6. SPIE, June 2016, p. 060502. DOI: 10.1117/1.JBO.21.6.060502.

[26] Erik A. Rodriguez et al. "The Growing and Glowing Toolbox of Fluorescent and Photoactive Proteins". In: *Trends Biochem. Sci.* 42.2 (Feb. 2017), pp. 111–129. DOI: 10.1016/j.tibs.2016.09.010.

[27] Zi Yao et al. "Multiplexed bioluminescence microscopy via phasor analysis". In: *Nat. Methods* 19 (July 2022), pp. 893–898. DOI: 10.1038/s41592-022-01529-9.

[28] Lingfei Lu et al. "NIR-II bioluminescence for in vivo high contrast imaging and in situ ATP-mediated metastases tracing". In: *Nat. Commun.* 11.4192 (Aug. 2020), pp. 1–11. DOI: 10.1038/s41467-020-18051-1.

[29] David Tibor Lauber et al. "State of the art in vivo imaging techniques for laboratory animals". In: *Lab. Anim.* 51.5 (Feb. 2017), pp. 465–478. DOI: 10.1177/0023677217695852.

[30] Ali Gholamrezanezhad et al. "Cytotoxicity of 111In-oxine on mesenchymal stem cells: a time-dependent adverse effect". In: *Nucl. Med. Commun.* 30.3 (Mar. 2009), pp. 210–216. DOI: 10.1097/MNM.0b013e328318b328.

[31] Masato Kobayashi et al. "Simultaneous acquisition of 99mTc- and 123I-labeled radiotracers using a preclinical SPECT scanner with CZT detectors". In: *Ann. Nucl. Med.* 30.4 (May 2016), pp. 263–271. DOI: 10.1007/s12149-015-1055-6.

[32] Li Li et al. "Superparamagnetic Iron Oxide Nanoparticles as MRI contrast agents for Non-invasive Stem Cell Labeling and Tracking". In: *Theranostics* 3.8 (2013), p. 595. DOI: 10.7150/thno.5366.

[33] Wei Liu and Joseph A. Frank. "Detection and Quantification of Magnetically Labeled Cells by Cellular MRI". In: *Eur. J. Radiol.* 70.2 (May 2009), p. 258. DOI: 10.1016/j.ejrad.2008.09.021.

[34] Sofia M. Pereira et al. "Evaluating the effectiveness of transferrin receptor-1 (TfR1) as a magnetic resonance reporter gene". In: *Contrast Media Mol. Imaging* 11.3 (May 2016), pp. 236–244. DOI: 10.1002/cmmi.1686. eprint: 26929139.

[35] Olga Koshkina et al. "Nanoparticles for "two color" 19F magnetic resonance imaging: Towards combined imaging of biodistribution and degradation". In: *J. Colloid Interface Sci.* 565 (Apr. 2020), pp. 278–287. DOI: 10.1016/j.jcis.2019.12.083.

[36] Kazuki Akazawa et al. "Perfluorocarbon-Based 19F MRI Nanoprobes for In Vivo Multicolor Imaging". In: *Angew. Chem. Int. Ed.* 57.51 (Dec. 2018), pp. 16742–16747. DOI: 10.1002/anie.201810363.

[37] Florian Grüner et al. "Localising functionalised gold-nanoparticles in murine spinal cords by X-ray fluorescence imaging and background-reduction through spatial filtering for human-sized objects". In: *Sci. Rep.* 8.16561 (Nov. 2018), pp. 1–12. DOI: 10.1038/s41598-018-34925-3.

[38] Christian Körnig et al. "In-situ x-ray fluorescence imaging of the endogenous iodine distribution in murine thyroids". In: *Sci. Rep.* 12.2903 (Feb. 2022), pp. 1–9. DOI: 10.1038/s41598-022-06786-4.

[39] Henrik Kahl et al. "Feasibility of Monitoring Tumor Response by Tracking Nanoparticle-Labelled T Cells Using X-ray Fluorescence Imaging—A Numerical Study". In: *Int. J. Mol. Sci.* 22.16 (Aug. 2021), p. 8736. DOI: 10.3390/ijms22168736.

[40] Jakob C. Larsson et al. "High-spatial-resolution x-ray fluorescence tomography with spectrally matched nanoparticles". In: *Phys. Med. Biol.* 63.16 (Aug. 2018), p. 164001. DOI: 10.1088/1361-6560/aad51e.

[41] Seongmoon Jung et al. "Dynamic In Vivo X-ray Fluorescence Imaging of Gold in Living Mice Exposed to Gold Nanoparticles". In: *IEEE Trans. Med. Imaging* 39.2 (July 2019), pp. 526–533. DOI: 10.1109/TMI.2019.2932014.

[42] Kian Shaker et al. "Longitudinal In-Vivo X-Ray Fluorescence Computed Tomography With Molybdenum Nanoparticles". In: *IEEE Trans. Med. Imaging* 39.12 (July 2020), pp. 3910–3919. DOI: 10.1109/TMI.2020.3007165.

[43] John M. Boone, Orlando Velazquez, and Simon R. Cherry. "Small-Animal X-ray Dose from Micro-CT". In: *Mol. Imag.* 3.3 (July 2004). DOI: 10.1162/15353500200404118.

[44] Inneke Willekens et al. "Evaluation of the radiation dose in micro-CT with optimization of the scan protocol". In: *Contrast Media Mol. Imaging* 5.4 (July 2010), pp. 201–207. DOI: 10.1002/cmmi.394.

[45] Theresa Staufer et al. "Assessing Cellular Uptake of Exogenous Coenzyme Q10 into Human Skin Cells by X-ray Fluorescence Imaging". In: *Antioxidants* 11.8 (Aug. 2022), p. 1532. DOI: 10.3390/antiox11081532.

[46] Oliver Schmutzler et al. "X-ray Fluorescence Uptake Measurement of Functionalized Gold Nanoparticles in Tumor Cell Microsamples". In: *Int. J. Mol. Sci.* 22.7 (Apr. 2021), p. 3691. DOI: 10.3390/ijms22073691. eprint: 33916283.

[47] Arthur Ungerer et al. "X-ray-Fluorescence Imaging for In Vivo Detection of Gold-Nanoparticle-Labeled Immune Cells: A GEANT4 Based Feasibility Study". In: *Cancers* 13.22 (Nov. 2021), p. 5759. DOI: 10.3390/cancers13225759.

[48] Gerhard Materlik, Trevor Rayment, and David I. Stuart. "Diamond Light Source: status and perspectives". In: *Philos. Trans. Royal Soc. A* 373.2036 (Mar. 2015), p. 20130161. DOI: 10.1098/rsta.2013.0161.

[49] Norbert Schell et al. *The High Energy Materials Science Beamline (HEMS) at PETRA III*. Vol. 772. Trans Tech Publications Ltd, 2014. DOI: 10.4028/www.scientific.net/MSF.772.57.

[50] J. Susini, M. Salomé, B. Fayard, R. Ortega, and B. Kaulich. "THE SCANNING X-RAY MICROPROBE AT THE ESRF "X-RAY MICROSCOPY" BEAMLINE". In: *Surf. Rev. Lett.* 09.01 (Feb. 2002), pp. 203–211. DOI: 10.1142/S0218625X02001793.

[51] Arthur H. Compton. "A Quantum Theory of the Scattering of X-rays by Light Elements". In: *Phys. Rev.* 21.5 (May 1923), pp. 483–502. DOI: 10.1103/PhysRev.21.483.

[52] O. Klein and Y. Nishina. "Über die Streuung von Strahlung durch freie Elektronen nach der neuen relativistischen Quantendynamik von Dirac". In: *Z. Phys.* 52.11 (Nov. 1929), pp. 853–868. DOI: 10.1007/BF01366453.

[53] Chen-Kai Qiao, Jian-Wei Wei, and Lin Chen. "An Overview of the Compton Scattering Calculation". In: *Crystals* 11.5 (May 2021), p. 525. DOI: 10.3390/cryst11050525.

[54] Tom Schoonjans et al. "The xraylib library for X-ray–matter interactions. Recent developments". In: *Spectrochim. Acta, Part B* 66.11 (Nov. 2011), pp. 776–784. DOI: 10.1016/j.sab.2011.09.011.

[55] Ilya Obodovskiy. "Chapter 6 - Interaction of Gamma Quanta With Matter". In: *Radiation*. Walthm, MA, USA: Elsevier, Jan. 2019, pp. 137–150. DOI: 10.1016/B978-0-444-63979-0.00006-9.

[56] Ervin B. Podgoršak. "Production of X Rays". In: *Radiation Physics for Medical Physicists*. Berlin, Germany: Springer, July 2009, pp. 177–205. DOI: 10.1007/978-3-642-00875-7_4.

[57] Manne Siegbahn. "Relations between the K and L Series of the High-Frequency Spectra". In: *Nature* 96 (Feb. 1916), p. 676. DOI: 10.1038/096676b0.

[58] R. Jenkins, R. Manne, R. Robin, and C. Senemaud. "Nomenclature system for X-ray spectroscopy, part VIII". In: *Pure Appl. Chem* 63 (Jan. 1991). URL: https://www.researchgate.net/publication/288262008_Nomenclature_system_for_X-ray_spectroscopy_part_VIII.

[59] Christian Körnig. "Spatial Reconstruction of small Objects for medical x-ray Fluorescence Imaging using multiple Detectors". MA thesis. Universität Hamburg, 2019.

[60] M.J. Berger, Coursey J.S., M.A. Zucker, and J. Chang. *Stopping-Power & Range Tables for Electrons, Protons, and Helium Ions*. Nov. 2017. DOI: 10.18434/T4NC7P. URL: https://www.nist.gov/pml/stopping-power-range-tables-electrons-protons-and-helium-ions.

[61] Ervin B. Podgoršak. "Energy Transfer and Energy Absorption in Photon Interactions with Matter". In: *Radiation Physics for Medical Physicists*. Berlin, Germany: Springer, July 2009, pp. 377–427. DOI: 10.1007/978-3-642-00875-7_8.

[62] "Biological Effects of Radiation". In: *Radiation Protection and Dosimetry*. Ed. by M. Stabin. New York, NY, USA: Springer, New York, NY, 2003, pp. 75–104. DOI: 10.1007/978-0-387-49983-3_6.

[63] Stephen M. Seltzer. "Calculation of Photon Mass Energy-Transfer and Mass Energy-Absorption Coefficients". In: *Radiat. Res.* 136.2 (Nov. 1993), pp. 147–170. DOI: 10.2307/3578607.

[64] C. S. Parkins, J. F. Fowler, R. L. Maughan, and M. J. Roper. "Repair in mouse lung for up to 20 fractions of X rays or neutrons". In: *Br. J. Radiol.* 58.687 (Mar. 1985), pp. 225–241. DOI: 10.1259/0007-1285-58-687-225. eprint: 4063664.

[65] W. D. Coolidge. “A Powerful R\"ontgen Ray Tube with a Pure Electron Discharge”. In: *Phys. Rev.* 2.6 (Dec. 1913), pp. 409–430. DOI: 10.1103/PhysRev.2.409.

[66] Ervin B. Podgoršak. “Particle Accelerators in Medicine”. In: *Radiation Physics for Medical Physicists*. Berlin, Germany: Springer, July 2009, pp. 609–643. DOI: 10.1007/978-3-642-00875-7_14.

[67] Gavin Poludniowski, Artur Omar, Robert Bujila, and Pedro Andreo. “Technical Note: SpekPy v2.0—a software toolkit for modeling x-ray tube spectra”. In: *Med. Phys.* 48.7 (July 2021), pp. 3630–3637. DOI: 10.1002/mp.14945.

[68] Robert Bujila, Artur Omar, and Gavin Poludniowski. “A validation of SpekPy: A software toolkit for modelling X-ray tube spectra”. In: *Physica Medica: European Journal of Medical Physics* 75 (July 2020), pp. 44–54. DOI: 10.1016/j.ejmp.2020.04.026.

[69] J. Xu, D. D. Reh, J. P. Carey, M. Mahesh, and J. H. Siewerdsen. “Technical assessment of a cone-beam CT scanner for otolaryngology imaging: Image quality, dose, and technique protocols”. In: *Med. Phys.* 39.8 (Aug. 2012), pp. 4932–4942. DOI: 10.1118/1.4736805.

[70] Xiaobing Li et al. “Fast microfocus x-ray tube based on carbon nanotube array”. In: *Journal of Vacuum Science & Technology B, Nanotechnology and Microelectronics: Materials, Processing, Measurement, and Phenomena* 37.5 (Aug. 2019), p. 051203. DOI: 10.1116/1.5099697.

[71] Helmut Wiedemann. “Overview of Synchrotron Radiation”. In: *Synchrotron Radiation*. Berlin, Germany: Springer, 2003, pp. 31–53. DOI: 10.1007/978-3-662-05312-6_3.

[72] Helmut Wiedemann. “Radiation Sources”. In: *Synchrotron Radiation*. Berlin, Germany: Springer, 2003, pp. 55–72. DOI: 10.1007/978-3-662-05312-6_4.

[73] Philip R. Willmott. "X-Ray Sources at Large-Scale Facilities". In: *Magnetism and Accelerator-Based Light Sources*. Cham, Switzerland: Springer, Mar. 2021, pp. 1–37. DOI: 10.1007/978-3-030-64623-3_1.

[74] Yuri Shvyd'ko. "High-Resolution X-Ray Monochromators". In: *X-Ray Optics*. Berlin, Germany: Springer, 2004, pp. 215–286. DOI: 10.1007/978-3-540-40890-1_5.

[75] Qi Xie et al. "Robust Low-dose CT Sinogram Preprocessing via Exploiting Noise-generating Mechanism". In: *IEEE Trans. Med. Imaging* 36.12 (Dec. 2017), p. 2487. DOI: 10.1109/TMI.2017.2767290.

[76] J. Radon. "über die Bestimmung von Funktionen durch ihre Integralwerte längs gewisser Mannigfaltigkeiten". In: *Berichte über die Verhandlungen der Sächsische Akademie der Wissenschaften* 69 (1917). 00000, pp. 262–277.

[77] R. N. Bracewell. "Strip Integration in Radio Astronomy". In: *Aust. J. Phys.* 9.2 (1956), pp. 198–217. DOI: 10.1071/ph560198.

[78] "Two-Dimensional Fourier-Based Reconstruction Methods". In: *Computed Tomography: From Photon Statistics to Modern Cone-Beam CT*. Berlin, Heidelberg: Springer Berlin Heidelberg, 2008, pp. 151–200. DOI: 10.1007/978-3-540-39408-2_5. URL: https://doi.org/10.1007/978-3-540-39408-2_5.

[79] "Algebraic and Statistical Reconstruction Methods". In: *Computed Tomography: From Photon Statistics to Modern Cone-Beam CT*. Berlin, Heidelberg: Springer Berlin Heidelberg, 2008, pp. 201–240. DOI: 10.1007/978-3-540-39408-2_6. URL: https://doi.org/10.1007/978-3-540-39408-2_6.

[80] Yulia Levakhina. "Where we are today: Tomosynthesis research and development". In: *Three-Dimensional Digital Tomosynthesis*. Wiesbaden, Germany: Springer Vieweg, Apr. 2014, pp. 11–41. DOI: 10.1007/978-3-658-05697-1_2.

[81] Yulia Levakhina. "Forward and backprojection model (FP/BP)". In: *Three-Dimensional Digital Tomosynthesis*. Wiesbaden, Germany: Springer Vieweg, Apr. 2014, pp. 43–74. DOI: 10.1007/978-3-658-05697-1_3.

[82] Arianna Ferrari, Luca Bertolaccini, Piergiorgio Solli, Paola Oriana Di Salvia, and David Scaradozzi. "Digital chest tomosynthesis: the 2017 updated review of an emerging application". In: *Ann. Transl. Med.* 6.5 (Mar. 2018), p. 91. DOI: 10.21037/atm.2017.08.18. eprint: 29666814.

[83] Rainer Schramm. "Use of X-ray Fluorescence Analysis for the Determination of Rare Earth Elements". In: *Physical Sciences Reviews* 1.9 (Sept. 2016). DOI: 10.1515/psr-2016-0061.

[84] Xin Feng, Huihua Zhang, and Peiqiang Yu. "X-ray fluorescence application in food, feed, and agricultural science: a critical review". In: *Crit. Rev. Food Sci. Nutr.* 61.14 (Aug. 2021), pp. 2340–2350. DOI: 10.1080/10408398.2020.1776677.

[85] Douglas J. Klapec, Greg Czarnopys, and Julie Pannuto. "Interpol review of detection and characterization of explosives and explosives residues 2016-2019". In: *Forensic Sci. Int.: Synergy* 2 (Jan. 2020), pp. 670–700. DOI: 10.1016/j.fsisyn.2020.01.020.

[86] Erica R Valdes and Kenneth T Hoang. *X-Ray Fluorescence Spectroscopy for Analysis of Explosive-Related Materials and Unknowns*. Tech. rep. ARMY EDGEWOOD CHEMICAL BIOLOGICAL CENTER APG MD ABERDEEN PROVING GROUND ..., 2017.

[87] B. Hochleitner, V. Desnica, M. Mantler, and M. Schreiner. "Historical pigments: a collection analyzed with X-ray diffraction analysis and X-ray fluorescence analysis in order to create a database". In: *Spectrochim. Acta, Part B* 58.4 (Apr. 2003), pp. 641–649. DOI: 10.1016/S0584-8547(02)00280-X.

[88] Oliver Schmutzler. "Foundations of Experimental Synchrotron Based X-ray Fluorescence Imaging in Medium Sized Objects". PhD thesis. Universität Hamburg, 2020.

[89] Yang Liu. "Synthesis and characterization of inorganic nanoparticles, and analysis of their uptake by cells and plants for in vitro and in vivo imaging". PhD thesis. Universität Hamburg, 2022.

[90] Nivedh Manohar, Francisco J. Reynoso, and Sang Hyun Cho. "Experimental demonstration of direct L-shell x-ray fluorescence imaging of gold nanoparticles using a benchtop x-ray source". In: *Med. Phys.* 40.8 (Aug. 2013), p. 080702. DOI: 10.1118/1.4816297.

[91] Yu Kuang et al. "Development of XFCT imaging strategy for monitoring the spatial distribution of platinum-based chemodrugs: Instrumentation and phantom validation". In: *Med. Phys.* 40.3 (Mar. 2013). DOI: 10.1118/1.4789917.

[92] Yu Kuang et al. "First Demonstration of Multiplexed X-Ray Fluorescence Computed Tomography (XFCT) Imaging". In: *IEEE Trans. Med. Imaging* 32.2 (Oct. 2012), pp. 262–267. DOI: 10.1109/TMI.2012.2223709.

[93] Seong-Kyun Cheong et al. "X-ray fluorescence computed tomography (XFCT) imaging of gold nanoparticle-loaded objects using 110 kVp x-rays". In: *Phys. Med. Biol.* 55.3 (Jan. 2010), pp. 647–662. DOI: 10.1088/0031-9155/55/3/007.

[94] Bernard L. Jones, Nivedh Manohar, Francisco Reynoso, Andrew Karellas, and Sang Hyun Cho. "Experimental demonstration of benchtop x-ray fluorescence computed tomography (XFCT) of gold nanoparticle-loaded objects using lead- and tin-filtered polychromatic cone-beams". In: *Phys. Med. Biol.* 57.23 (Nov. 2012), N457–N467. DOI: 10.1088/0031-9155/57/23/n457.

[95] Siyuan Zhang et al. "Quantitative Imaging of Gd Nanoparticles in Mice Using Benchtop Cone-Beam X-ray Fluorescence Computed Tomography System". In: *Int. J. Mol. Sci.* 20.9 (May 2019). DOI: 10.3390/ijms20092315.

[96] Samuel Huber. private communication.

[97] Kian Shaker, Jakob C. Larsson, and Hans M. Hertz. "Quantitative predictions in small-animal X-ray fluorescence tomography". In: *Biomed. Opt. Express* 10.8 (Aug. 2019), pp. 3773–3788. DOI: 10.1364/BOE.10.003773.

[98] R. A. Sareen B. G. Lowe. *Semiconductor X-Ray Detectors*. Andover, England, UK: Taylor & Francis, Nov. 2013. DOI: 10.1201/b16093.

[99] W. Shockley. "Currents to Conductors Induced by a Moving Point Charge". In: *J. Appl. Phys.* 9.10 (Oct. 1938), pp. 635–636. DOI: 10.1063/1.1710367.

[100] S. Ramo. "Currents Induced by Electron Motion". In: *Proc. IRE* 27.9 (Sept. 1939), pp. 584–585. DOI: 10.1109/JRPROC.1939.228757.

[101] Hermann Kolanoski and Norbert Wermes. "Semiconductor detectors". In: *Particle Detectors*. Oxford, England, UK: Oxford University Press, pp. 255–372. DOI: 10.1093/oso/9780198858362.003.0008.

[102] R. Redus. *Application Note AN-DPP-001: Digital Pulse Processors Theory of Operation*. Tech. rep. Amptek Inc. URL: https://www.amptek.com/-/media/ametekamptek/documents/resources/dpp_theory.pdf?la=en&revision=0b5bb590-e4b6-4038-ab67-3516060fa5e7.

[103] Karl Hecht. "Zum Mechanismus des lichtelektrischen Primärstromes in isolierenden Kristallen". In: *Z. Phys.* 77.3 (Mar. 1932), pp. 235–245. DOI: 10.1007/BF01338917.

[104] Robert H. Redus, John A. Pantazis, Thanos J. Pantazis, Alan C. Huber, and Brian J. Cross. "Characterization of CdTe Detectors for Quantitative X-ray Spectroscopy". In: *IEEE Trans. Nucl. Sci.* 56.4 (Aug. 2009), pp. 2524–2532. DOI: 10.1109/TNS.2009.2024149.

[105] Amptek Inc. *Application Note AN-SDD-003: Amptek Silicon Drift Detectors*. Tech. rep. URL: https://www.amptek.com/-/media/ametekamptek/documents/resources/amptek-silicon-drift-detectors.pdf?la=en&revision=c99a4a99-420c-4334-a06d-98ecb7da87fe.

[106] Gerald Falkenberg et al. "CRL optics and silicon drift detector for P06 Microprobe experiments at 35 keV". In: *Powder Diffr.* 35.S1 (Dec. 2020), S34–S37. DOI: 10.1017/S0885715620000536.

[107] J. Allison et al. "Geant4 developments and applications". In: *IEEE Trans. Nucl. Sci.* 53.1 (Feb. 2006), pp. 270–278. DOI: 10.1109/TNS.2006.869826.

[108] S. Agostinelli et al. "Geant4—a simulation toolkit". In: *Nucl. Instrum. Methods Phys. Res., Sect. A* 506.3 (July 2003), pp. 250–303. DOI: 10.1016/S0168-9002(03)01368-8.

[109] J. Allison et al. "Recent developments in Geant4". In: *Nucl. Instrum. Methods Phys. Res., Sect. A* 835 (Nov. 2016), pp. 186–225. DOI: 10.1016/j.nima.2016.06.125.

[110] Vladimir Ivanchenko, John Apostolakis, Alexander Bagulya, Haifa Ben Abdelouahed, and Christina Zacharatou. "Recent Improvements in Geant4 Electromagnetic Physics Models and Interfaces". In: *Progress in NUCLEAR SCIENCE and TECHNOLOGY* 2 (Oct. 2011), pp. 898–903. DOI: 10.15669/pnst.2.898.

[111] Amptek Inc. *User Operating Manual 70 mm2 XR-100FastSDD X-Ray Detector & Preamplifier*. Tech. rep. 2018.

[112] Amptek Inc. *User Operating Manual XR-100CdTe X-Ray Detector & Preamplifier*. Tech. rep. 2018.

[113] Ulrich Lienert. *Conceptual Design Report of the Swedish Materials Science Beamline at PETRA III*. Tech. rep. Desy, Hamburg, Germany, 2012. URL: https://petra3-extension.desy.de/sites2009/site_petra3-ext/content/e84814/e260936/e260937/ConceptualDesignReport_1.pdf.

[114] *P21.1 Beamline Data Sheet*. https://photon-science.desy.de/facilities/petra_iii/beamlines/p21_swedish_materials_science/p211_high_energy_x_ray_diffraction_for_physics_and_chemistry/unified_data_sheet_p211/index_eng.html.

[115] Oleh Ivashko. private communication.

[116] Willem Rischau. *Characterization of the X-ray eye*. Tech. rep. Friedrich Schiller University Jena, Germany, 2009. URL: https://photon-science.desy.de/research/technical_groups/detectors/presentations/e190266/CharacterizationoftheX-rayeye-ReportofWillemRischau1.pdf.

[117] *TANGO Controls*. http://www.tango-controls.org.

[118] Amptek Inc. *Amptek Digital Products Programmer's Guide*. Tech. rep. 2020.

[119] Trinamic GmbH. *TMCM-6212 TMCL Firmware Manual*. Tech. rep. 2016.

[120] Belma Dogdas, David Stout, Arion F. Chatziioannou, and Richard M. Leahy. "Digimouse: a 3D whole body mouse atlas from CT and cryosection data". In: *Phys. Med. Biol.* 52.3 (Jan. 2007), pp. 577–587. DOI: 10.1088/0031-9155/52/3/003.

[121] Marie Wegner, Elisabetta Gargioni, and Dieter Krause. "Einsatzmöglichkeiten der additiven Fertigung in der Herstellung von Phantomen". In: *Konstruktion für die Additive Fertigung 2020*. Ed. by Roland Lachmayer, Katharina Rettschlag, and Stefan Kaierle. Berlin, Heidelberg: Springer Berlin Heidelberg, 2021, pp. 267–282.

[122] A. Brunetti, M. Sanchez del Rio, B. Golosio, A. Simionovici, and A. Somogyi. "A library for X-ray–matter interaction cross sections for X-ray fluorescence applications". In: *Spectrochim. Acta, Part B* 59.10 (Oct. 2004), pp. 1725–1731. DOI: 10.1016/j.sab.2004.03.014.

[123] Pauli Virtanen et al. "SciPy 1.0: Fundamental Algorithms for Scientific Computing in Python". In: *Nature Methods* 17 (2020), pp. 261–272. DOI: 10.1038/s41592-019-0686-2.

[124] Giovanni Punzi. "Sensitivity of searches for new signals and its optimization". In: *arXiv* (Aug. 2003). DOI: 10.48550/arXiv.physics/0308063. eprint: physics/0308063.

[125] Yue Sun, Sophie-Charlotte Gleber, Chris Jacobsen, Janos Kirz, and Stefan Vogt. "Optimizing detector geometry for trace element mapping by X-ray fluorescence". In: *Ultramicroscopy* 152 (May 2015), p. 44. DOI: 10.1016/j.ultramic.2014.12.014.

[126] Siwen An, Salim Reza, Börje Norlin, Christer Fröjdh, and Göran Thungström. "Signal-to-noise ratio optimization in X-ray fluorescence spectrometry for chromium contamination analysis". In: *Talanta* 230 (Aug. 2021), p. 122236. DOI: 10.1016/j.talanta.2021.122236.

[127] R. L. Owen, J. M. Holton, C. Schulze-Briese, and E. F. Garman. "Determination of X-ray flux using silicon pin diodes". In: *J. Synchrotron Radiat.* 16.2 (Mar. 2009), pp. 143–151. DOI: 10.1107/S0909049508040429.

[128] Penelope Pelczar et al. "A pathogenic role for T cell–derived IL-22BP in inflammatory bowel disease". In: *Science* 354.6310 (Oct. 2016), pp. 358–362. DOI: 10.1126/science.aah5903. URL: https://www.science.org/doi/10.1126/science.aah5903.

[129] Jerome C. Martin et al. "Single-Cell Analysis of Crohn's Disease Lesions Identifies a Pathogenic Cellular Module Associated with Resistance to Anti-TNF Therapy". In: *Cell* 178.6 (Sept. 2019), p. 1493. DOI: 10.1016/j.cell.2019.08.008.

[130] B. Smevik and J. Westvik. "Iohexol for contrast enhancement of bowel in pediatric abdominal CT". In: *Acta Radiol.* 31.6 (Nov. 1990), pp. 601–604. eprint: 2278786. URL: https://pubmed.ncbi.nlm.nih.gov/2278786.

[131] Subramaniyan Bharathiraja et al. "Multimodal tumor-homing chitosan oligosaccharide-coated biocompatible palladium nanoparticles for photo-based imaging and therapy". In: *Sci. Rep.* 8.500 (Jan. 2018), pp. 1–16. DOI: 10.1038/s41598-017-18966-8.

[132] Mei Chen et al. "Safety profile of two-dimensional Pd nanosheets for photothermal therapy and photoacoustic imaging". In: *Nano Res.* 10.4 (Apr. 2017), pp. 1234–1248. DOI: 10.1007/s12274-016-1349-6.

[133] Myriam Laprise-Pelletier, Jean Lagueux, Marie-France Côté, Thomas LaGrange, and Marc-André Fortin. "Low-Dose Prostate Cancer Brachytherapy with Radioactive Palladium–Gold Nanoparticles". In: *Adv. Healthcare Mater.* 6.4 (Feb. 2017), p. 1601120. DOI: 10.1002/adhm.201601120.

[134] Nikolaos Stathatos. "Anatomy and Physiology of the Thyroid Gland". In: *The Thyroid and Its Diseases*. Cham, Switzerland: Springer, Jan. 2019, pp. 3–12. DOI: 10.1007/978-3-319-72102-6_1.

[135] Ji Min Oh et al. "Development of an athyroid mouse model using 131 I ablation after preparation with a low-iodine diet". In: *Sci. Rep.* 7.1 (Oct. 2017), p. 13284. DOI: 10.1038/s41598-017-13772-8. eprint: 29038462.

[136] Yuhao Li et al. "Quantification of radioactivity by planar gamma-camera images, a promoted method of absorbed dose in the thyroid after iodine-131 treatment".

In: *Sci. Rep.* 8.1 (July 2018), p. 10167. DOI: 10.1038/s41598-018-28571-y. eprint: 29977082.

[137] Chien-Chih Ke et al. "Quantitative Measurement of the Thyroid Uptake Function of Mouse by Cerenkov Luminescence Imaging". In: *Sci. Rep.* 7.1 (July 2017), p. 5717. DOI: 10.1038/s41598-017-05516-5. eprint: 28720762.

[138] R. Rocchi, T. Kunavisarut, P. Ladenson, and P. Caturegli. "Thyroid uptake of radioactive iodine and scintigraphy in mice". In: *Thyroid* 16.7 (July 2006), pp. 705–706. DOI: 10.1089/thy.2006.16.705. eprint: 16889498.

[139] Freek J. Beekman et al. "Towards in vivo nuclear microscopy: iodine-125 imaging in mice using micro-pinholes". In: *Eur. J. Nucl. Med. Mol. Imaging* 29.7 (July 2002), pp. 933–938. DOI: 10.1007/s00259-002-0805-6. eprint: 12111135.

[140] Qian Yin et al. "Poly(iohexol) nanoparticles as contrast agents for in vivo X-ray computed tomography imaging". In: *J. Am. Chem. Soc.* 135.37 (Sept. 2013), pp. 13620–13623. DOI: 10.1021/ja405196f. eprint: 23987119.

[141] A. P. Dempster, N. M. Laird, and D. B. Rubin. "Maximum Likelihood from Incomplete Data via the EM Algorithm on JSTOR". In: *Journal of the Royal Statistical Society. Series B (Methodological)* 39.1 (1977), pp. 1–38. URL: https://www.jstor.org/stable/2984875.

[142] L. A. Shepp and Y. Vardi. "Maximum Likelihood Reconstruction for Emission Tomography". In: *IEEE Trans. Med. Imaging* 1.2 (Oct. 1982), pp. 113–122. DOI: 10.1109/TMI.1982.4307558.

[143] Ming Yan and Luminita A. Vese. "Expectation maximization and total variation-based model for computed tomography reconstruction from undersampled data". In: *Proceedings Volume 7961, Medical Imaging 2011: Physics of Medical Imaging*. Vol. 7961. SPIE, Mar. 2011, pp. 833–840. DOI: 10.1117/12.878238.

[144] M. R. Hestenes and E. Stiefel. "Methods of conjugate gradients for solving linear systems". In: *J Res NIST* 49.6 (1952), pp. 409–436. DOI: 10.6028/jres.049.044. URL: http://dx.doi.org/10.6028/jres.049.044.

[145] Dianwen Zhu and Changqing Li. "Nonconvex regularizations in fluorescence molecular tomography for sparsity enhancement". In: *Phys. Med. Biol.* 59.12 (May 2014), pp. 2901–2912. DOI: 10.1088/0031-9155/59/12/2901.

[146] Dianwen Zhu and Changqing Li. "Accelerated image reconstruction in fluorescence molecular tomography using a nonuniform updating scheme with momentum and ordered subsets methods". In: *J. of Biomedical Optics, 21(1)*. Vol. 21. 1. SPIE, Jan. 2016, p. 016004. DOI: 10.1117/1.JBO.21.1.016004.

[147] Anastasios Gaitanis, George Kontaxakis, George Spyrou, George Panayiotakis, and George Tzanakos. "PET image reconstruction: A stopping rule for the MLEM algorithm based on properties of the updating coefficients". In: *Comput. Med. Imaging Graph.* 34.2 (Mar. 2010), pp. 131–141. DOI: 10.1016/j.compmedimag.2009.07.006.

[148] Stéfan van der Walt et al. "scikit-image: image processing in Python". In: *PeerJ* 2 (June 2014), e453. DOI: 10.7717/peerj.453. URL: https://doi.org/10.7717/peerj.453.

[149] Zhou Wang, A. C. Bovik, H. R. Sheikh, and E. P. Simoncelli. "Image quality assessment: from error visibility to structural similarity". In: *IEEE Trans. Image Process.* 13.4 (Apr. 2004), pp. 600–612. DOI: 10.1109/TIP.2003.819861.

[150] Tina Samajdar and Md. Iqbal Quraishi. "Analysis and Evaluation of Image Quality Metrics". In: *Information Systems Design and Intelligent Applications*. Delhi, NY, USA: Springer, Jan. 2015, pp. 369–378. DOI: 10.1007/978-81-322-2247-7_38.

[151] Rafael C. Gonzalez and Richard E. Woods. *Digital image processing*. London, England, UK: Pearson, 2018.

[152] Tenta Sasaya et al. "EM-TV reconstruction algorithm for pinhole-type fluorescent X-ray computed tomography". In: *2015 10th Asian Control Conference (ASCC)*. IEEE, May 2015, pp. 1–6. DOI: 10.1109/ASCC.2015.7244545.

Acknowledgement

First, I would like to thank my supervisor Prof. Dr. Florian Grüner for the continuous support during my thesis and for giving me the freedom to explore new ideas. I cannot remenber a single time you prevented me from working on one of them and always found a way to test them. Thinking back at where we started a few years ago, I am amazed of what you have made possible. I also want to thank Prof. Dr. Wolfgang J. Parak, not only for reviewing my thesis but also for providing an insight into the field of nanoscience and it's sheer possibilities.

I also want to thank the whole medical imaging team. We always had a great atmosphere and albeit no being able to meet in the office we managed to keep it that way.
Especially, I want to thank Theresa Staufer for her commitment and support at all times. Whether during normal workdays or at 2 a.m. during beamtimes, everyone can always rely on you. It was a pleasure to work with you.
I want to thank Oliver Schmutzer, with whom I enjoyed - sometimes lengthy - coffee brakes and great discussions. Many of them have proven to be very fruitful, others were just great distractions to clear the mind. I cannot decide, which ones I liked the most.

Besides my colleagues, I would like to thank my familiy for the endless support over all the years, always providing guidance but never pushing, you were a great help at all times.
Last but not least, there is one person without whom I would not have come to this point. You provided the balance I needed and have always been there for me. Thank you, Tonja.

Eidesstattliche Versicherung

Declaration on oath

Hiermit versichere ich an Eides statt, die vorliegende Dissertationsschrift selbst verfasst und keine anderen als die angegebenen Hilfsmittel und Quellen benutzt zu haben.

Hamburg, den 7.9.2022

Christian Gabriel Körnig